A window to the first stars: An investigation of chemically near-pristine environments.

LOUISE AMBER WELSH

A window to the first stars:

An investigation of chemically near-pristine environments.

Louise Amber Welsh

A Thesis presented for the degree of
Doctor of Philosophy

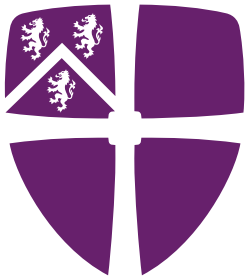

Durham University

Centre for Extragalactic Astronomy
Department of Physics
Durham University
United Kingdom

August 2021

A window to the first stars:

An investigation of chemically near-pristine environments.

Louise Amber Welsh

Submitted for the degree of Doctor of Philosophy

August 2021

Abstract: The first stars in the Universe are an elusive stellar population that we know relatively little about. They are the only stellar population to necessarily form in the absence of metals. Thus, they are in principle easy to identify. However, we are yet to detect a metal-free star in the local Universe. The fusion of metals in the cores of these first stars marks the onset of complex chemical evolution. The eventual collapse of massive (> 10 $M_{\odot}$) metal-free stars released the first instances of metals into the surrounding environment. From simulations of stellar evolution, we know that stars with different properties produce different chemical patterns. Thus, to study these stars, we can search for environments that have retained the chemical fingerprint of the first supernovae. It is the environments that have experienced minimal processing through stars that are likely to showcase the chemistry of the first stellar population. These 'windows to the first stars' can be identified through their lack of metals.

This thesis presents a novel stochastic chemical enrichment model that uses the chemistry of relic environments to investigate the properties of the enriching stellar population. This model, along with nucleosynthetic yield calculations, allows us to investigate the number of massive stars that have chemically contributed to an environment, the mass distribution of the enriching population, the typical explosion energy of their supernovae, and the degree of mixing between the stellar layers. The utility of this model is shown by searching for the chemical fingerprint of the first stars in both the most metal-poor damped Lyman-α systems (DLAs) and the most metal-poor stars in the halo of the Milky Way. We also

present and analyse new observational data of near-pristine DLAs. This includes the first bound on the carbon isotope ratio of a chemically near-pristine DLA. This isotope ratio can be used to investigate enrichment from low mass ($\sim$ 1 $M_{\odot}$) metal-free stars. The full complement of chemistry available for this DLA suggests that it may have experienced a hiatus in star formation following the epoch of reionisation. Finally, we present the precise [O/Fe] abundance determinations of two near-pristine DLAs. This investigation aims to establish whether [O/Fe] is elevated amongst the most metal-poor DLAs. The ultimate goal of this thesis is to investigate the properties of the first stars through their surviving chemistry and establish the most useful metals to utilise to this end. There is a focus on the most metal-poor DLAs and their role in early chemical enrichment and galaxy evolution.

Declaration

The work described in this thesis was undertaken between October 2017 and August 2021 while the author was a research student under the supervision of Dr. Ryan Cooke and Prof. Michele Fumagalli in the Centre for Extragalactic Astronomy at Durham University, England. No part of this thesis has been submitted for any degree or qualification at Durham University or elsewhere. Chapter 2 has been published as:

"Modelling the chemical enrichment of Population III supernovae: the origin of the metals in near-pristine gas clouds" Welsh, L., Cooke, R., & Fumagalli, M. MNRAS, 487, 3363 (2019)

Chapter 3 has been published as:

"The stochastic enrichment of Population II stars" Welsh, L., Cooke, R., & Fumagalli, M. MNRAS, 500, 5214 (2021)

Chapter 4 has been published as:

"A bound on the 12C/13C ratio in near-pristine gas with ESPRESSO" Welsh, L., Cooke, R., Fumagalli, M., & Pettini, M. MNRAS, 494, 1411 (2020)

Chapter 5 is in the final stages of preparation for submission to The Astrophysical Journal.

The author of this thesis was primarily responsible for the work contained in these publications. All figures in this thesis were prepared by the author, or have been properly attributed in the figure caption.

without the author's prior written consent and information derived from it should be acknowledged."

Acknowledgements

I like to think that we are the cumulative product of the people we've met and the experiences we've shared. So, I am lucky to have such wonderful friends and family. I owe a special thanks to my parents and grandparents: Margaret, Archie, Rita, Robert, Sarah, and Maggie. Thank you for your endless support and encouragement. I also send my love to my brothers: Ruairidh, Sean, Michael, and Andrew.

Next, I must thank my supervisors, Ryan and Michele. I could not have asked for a more supportive and informative supervisory team. Ryan, thank you being a great teacher and always finding time whenever I needed help. I appreciate the guidance, patience, and freedom over the past four years. Michele, thank you for always keeping the big picture in mind and knowing how to express what I'm saying in a fraction of the words.

To my office mates: Tom, Ugne, Oliver, Jack, Alex, and Stefan thanks for the laughs... and the occasional office debate! It was a pleasure coming into the office everyday. A honorary mention to gorgeous George — my family cat — who has been a trusted office mate for the past year. You have been less helpful with astronomy but fluffy nonetheless.

To the rest of my friends and colleagues in Durham, most of whom I haven't seen this past year, thanks for making this city a fantastic place live and learn. A non exhaustive list (I'm sure) includes: Anna, Aidan, Andrew, Arnau, Amy, Behzad, Beatriz, Carol, Chris, Calvin, Emma, Harry, Giacomo, Jack, Jake, James, Joaquin, Josh, Lizelke, Raad, Tom, and Vicky. Anastasia and Anouk — you are my rocks! Thank you for being wonderful friends. I wouldn't have made it through the past eight years of education if I hadn't met you both.

Dedicated to

my family.

Contents

List of Figures

List of Tables

CHAPTER 1

Introduction

1.1 Context

Our current cosmological model relies on hierarchical structure formation to grow components of the Universe. Within the framework of ΛCDM, structures form from initial perturbations of the density field in the Universe. These perturbations are first detectable $\sim 380,000$ years after the Big Bang in the temperature fluctuations of the cosmic microwave background radiation (Planck Collaboration et al., 2020). It is these perturbations that will eventually give rise to the inhomogeneous distribution of matter that is observed on small scales today. In this framework, the first baryonic structures to form were the putative first stars (known as Population III/Pop III stars).

Prior to the formation of these stars, the Universe was made up entirely of hydrogen, helium, and trace amounts of lithium. Predominantly, just two elements. These stars are the catalyst to all complex chemical evolution — their cores provide the hot, dense environment necessary to fuse the first metals (i.e. elements heavier than lithium). Since structures form through a 'bottom-up' mechanism, the first stars, and the elements they produced, are the building blocks of the first galaxies.

We have searched for Population III stars in the halo of the Milky Way, and the surrounding

dwarf galaxies, with numerous dedicated surveys over the last forty years (e.g. Bond, 1980). None have been found. Our current understanding of the first stars is therefore driven by two means: (1) cosmological hydrodynamical simulations, and (2) observational searches for their chemical fingerprint. This thesis marks a contribution to the latter field of research, with a particular focus on investigating high redshift gas reservoirs. First, we provide an overview of our current understanding of the first stars and their observational probes, starting with a theoretical framework of their formation.

1.2 The first stars

In the paradigm of ΛCDM, the matter density of the Universe is dominated by cold dark matter (CDM). The baryonic component constitutes just $1/6$ of the matter content of the Universe. Some million years after the Big Bang, the dark matter is thought to have formed into 'minihalos' driven by the initial density perturbations. It is within the gravitational potential wells created by these minihalos that the first stars are thought to form (Bromm et al., 2009). Cosmological hydrodynamical simulations suggest that the first stars form at $z \sim 15 - 30$ when the dark matter minihalos are $\sim 10^{6-7}$ $M_\odot$ (Tegmark et al., 1997; Abel et al., 1998; Yoshida et al., 2003; Bromm et al., 2003; Xu et al., 2013).

As realised by Saslaw & Zipoy (1967), primordial gas clouds rely on molecular hydrogen to cool and radiate energy. Compared to cooling in metal-enriched gas, cooling via H_2 is relatively inefficient (Glover, 2013). This leads to reduced fragmentation of the protostellar gas cloud and, ultimately, larger stellar structures. The first stars are the only stellar population that necessarily form in the absence of metals. Thus, it has long been thought that the first stars form with a characteristic mass larger than that of stars that form today. A key prediction from simulations of Population III star formation is their characteristic mass. The initial mass function (IMF) of the first stars — which describes the relative number of stars that form as a function of their mass — is still an open question.

1.2.1 Underlying mass distribution

The concept of a stellar IMF was first introduced by Salpeter (1955). In this paper, the IMF of the local stellar population was modelled as a power law:

$$\xi(M) = \frac{dN}{dM} \propto M^{-\Gamma} \tag{1.2.1}$$

The slope, Γ, is found to be $\Gamma = 2.35$ for stars in the solar neighbourhood. This represents a bottom-heavy IMF, where stars preferentially form with lower masses. Alternative forms of the IMF (e.g. Kroupa 2001 and Chabrier 2003) are consistent with a Salpeter power-law for stars (> 1 $M_\odot$). Since then, it has been asked whether this IMF is universal. Or, whether it varies with time and/or environment (Bastian et al., 2010). Given their unique formation history, the first stars are an ideal population to test the universal nature of the IMF.

Some of the first simulations of Population III star formation suggest their initial mass range spanned $(100 - 1000)$ $M_\odot$ (Bromm et al., 1999, 2002; Abel et al., 2000, 2002). Over the past decade, the predicted mass range has decreased to $(10 - 100)$ $M_\odot$ (Yoshida et al., 2006; Stacy et al., 2010; Turk et al., 2009; Greif et al., 2010; Hirano et al., 2014). In fact, there are some simulations that suggest the mass range of these first stars may be comparable to the stars that form today (i.e. ~ 1 $M_\odot$) (Clark et al., 2011; Stacy & Bromm, 2014; Stacy et al., 2016). The true range remains unknown.

Another aspect of the mass distribution that is still a mystery is the multiplicity of the first stars — i.e. the number of stars that form in a given minihalo. Current simulations predict that the first stars form either individually or in small multiples. Uncovering the mass distribution of the first stars is a primary aim of the work presented in this thesis. We will therefore return to this topic frequently, particularly in Chapters 2, 3, and 4.

1.2.2 Eventual collapse

Generally speaking, the first stars are thought to be a relatively massive population ($\gtrsim 10$ $M_\odot$). This means that they likely had short lifetimes and are long since dead. The

ultimate fate of these metal-free stars is dependent on their mass. Those with masses $10 < M/\mathrm{M}_\odot < 70$ end their lives as core collapse supernovae (CCSNe) (Heger & Woosley, 2002; Heger et al., 2003; Heger & Woosley, 2010). Though, a fraction of these progenitors may fail to explode once $M > 20$ $\mathrm{M}_\odot$ and collapse directly into black holes instead (Sukhbold et al., 2016; Sukhbold & Adams, 2019; Burrows et al., 2019). The transition to pulsational pair instability SNe occurs ~ 70 $\mathrm{M}_\odot$ (Woosley, 2017). This fate persists until $M > 140$ $\mathrm{M}_\odot$, when pair instability SNe occur. Above 260 $\mathrm{M}_\odot$, the stars are thought to collapse directly into black holes. These distinct fates will in turn produce distinct chemical yields. The energies associated with these events will also vary. Thus, the dynamical and chemical impact of the first stars on the formation of the first galaxies depends on their underlying IMF (Nomoto et al., 2013).

1.3 The first galaxies

It is clear that the first stars had a substantial impact on the early Universe. The radiation from these stars kick-started the epoch of reionisation (Barkana & Loeb, 2001) — the period in which neutral hydrogen is reionised to its initial state in the early Universe. The first galaxies are another early contributor to the reionisation epoch. The size and number abundance of the first galaxies are impacted by the first stars. In turn, the properties of the first stars have a further indirect impact on the rate of cosmic reionisation.

Current theory suggests that the minihalos in which the first stars form do not evolve into the first galaxies. Instead, the first galaxies may be the atomically cooled halos $\sim 10^8$ $\mathrm{M}_\odot$ that form around $z \sim 10$. A schematic of this from Bromm & Yoshida (2011) is shown in Figure 1.1. This picture is driven by two processes that essentially inhibit further star formation in the initial minihalos: (1) the radiative feedback of the first stars, and (2) their energetic SNe. The first process creates a pressure wall that suppresses the gas density in the minihalos. The second process disrupts the gas in the halos and leaves them without enough gas to fuel further star formation (Bromm et al., 2003; Kitayama et al., 2004). A

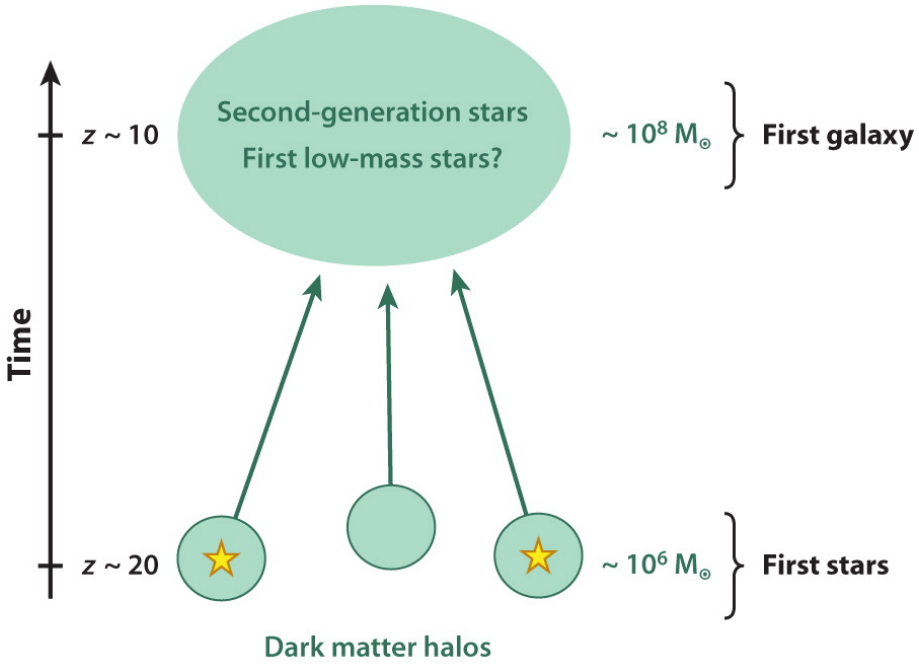

AR Bromm V, Yoshida N. 2011.
Annu. Rev. Astron. Astrophys. 49:373–407

Figure 1.1. Schematic of the formation of the first galaxies.

consequence of this is that it takes time for the gas in these large dark matter halos to settle, cool, and facilitate further star formation. This time frame is expected to be some 10^7 years (Johnson & Bromm, 2007; Yoshida et al., 2007; Alvarez et al., 2009; Bromm & Yoshida, 2011). Between this period and the onset of enrichment from the second generation of (Population II) stars, enriched gas will retain the chemical fingerprint of the first SNe (i.e. the first metals).

1.3.1 The first metals

The death of the first stars marks the onset of complex chemical enrichment in our Universe. A natural question is therefore what metals did the first stars produce and where did they end up?

Given the expected mass range of Population III stars ($\sim 10 - 100$ $M_{\odot}$), it is the yields of Population III CCSNe that are the dominant source of the first metals. To predict the yields

of Population III CCSNe, we rely on simulations of the evolution and eventual collapse of metal-free progenitors like those of Woosley & Weaver (1995); Heger & Woosley (2002); Chieffi & Limongi (2004); Meynet et al. (2006); Ekström et al. (2008); Heger & Woosley (2010); Limongi & Chieffi (2012). These simulations follow the fusion of metals within a stellar core and during the explosive nuclear burning phase that ends its life. They use nucleosynthetic reactions to track the production of metals and calculate the eventual yields of these metals following the core collapse.

These simulations are invaluable when it comes to investigating the properties of Population III stars using their surviving chemistry. However, it should be noted that the mechanism through which stars collapse is still unknown (Melson et al., 2015). They therefore rely on parameterisations of the explosions to successfully predict CCSNe yields. This introduces a degree of uncertainty that is currently unaccounted for in most published yield grids. A potential solution to this uncertainty may be to empirically determine the yields of Population III SNe using the observed chemistry of relic environments (e.g. Haze Nuñez et al., 2021). This approach is relatively new and would circumvent the need to model the explosion mechanism of the SNe.

1.4 Stellar archaeology

The surface abundances of stars are a snapshot of the chemical composition of the gas from which they formed. Exploiting this physicality to study the chemistry of the early Universe is known as stellar archaeology (Frebel, 2010; Frebel & Norris, 2015). The stars that formed in the wake of the first SNe hold clues about the Population III properties. Some of these stars, those with masses < 0.8 $M_{\odot}$, are expected to survive until the present day. While we may not be able to detect a metal-free star locally, we may be able to detect their chemistry in these stellar relics.

When searching for the chemistry of the first stars, we are looking for gas that has *only* been enriched by the first SNe. This gas has necessarily experienced minimal processing through stars and is therefore largely devoid of metals. A typical metallicity indicator is

the relative Fe abundance. When discussing chemical abundances, we tend to quote the log of the number abundance ratio of two elements relative to their solar value:

$$[\mathrm{X/Y}] = \log_{10}(N_\mathrm{X}/N_\mathrm{Y}) - \log_{10}(N_\mathrm{X}/N_\mathrm{Y})_\odot \,. \tag{1.4.1}$$

An object is considered to be extremely metal-poor (EMP) when [Fe/H] < -3 (i.e. when it is 1000 times more Fe poor than the Sun).

Perhaps the most interesting revelation to come from searching for Population III stars is the discovery of these stellar relics. So far, > 650 EMP stars have been found in the halo of the Milky Way and the surrounding dwarf galaxies[1].

The most iron-poor star to date has a relative iron abundance [Fe/H] < -7.1 (Keller et al., 2014); this is over 10 000 000 times more iron-poor than the Sun! More conservatively, the most iron-poor star with a detectable iron abundance is [Fe/H] $= -6.2 \pm 0.2$ (Nordlander et al., 2019). These stars included, there are 6 known stars with [Fe/H] < -5 (Frebel et al., 2005; Aoki et al., 2006; Christlieb et al., 2002, 2004; Allende Prieto et al., 2015; Frebel et al., 2015). All show a strong overabundance of carbon relative to iron. This chemical peculiarity has come to be recognised as a signature of enrichment from Population III stars, when combined with a 'normal' abundance of neutron capture elements (i.e. CEMP-no stars; Beers & Christlieb, 2005).

Historically, it has been assumed that the *most* metal-poor stars have been enriched by the SN of one Population III progenitor. This may hold true for the stars described above due to their incredibly low Fe abundance. However, this may not be the case for Population II stars that are more moderately EMP (i.e. those with $-5 <$ [Fe/H] < -3). The alternative approach has been to compare the chemistry of these stars to the IMF weighted abundance of elements predicted from Population III yields (e.g. Cayrel et al., 2004). There are simulations that suggest Population II stars form from the yields of multiple Population III SNe (Jeon et al., 2015; Ritter et al., 2015). Given that the first stars may form in small multiples, there is utility in considering a model somewhere in between these two

[1]According to the SAGA database (Suda et al., 2008) that had been last updated in 2019 at the time of writing.

extremes.

A study of 12 stars with [Fe/H] < -4 found that 68% (i.e. 7 out of 12) of these stars could not be easily reproduced by the Heger & Woosley (2010) yields of one Population III SN (Placco et al., 2016). It may therefore be necessary to consider a second class of progenitor for these stars; for example Population III stars that undergo fast rotation or aspherical SNe (Meynet et al., 2006; Ezzeddine et al., 2019). Or, indeed, it may be that these ill-fit stars have been enriched by multiple SNe.

In this thesis, we present a stochastic chemical enrichment model that aims to unravel the number of Population III stars that have enriched a relic environment. This coincides with a renewed effort in modelling the chemistry of metal-poor environments enriched by multiple SNe. Notably, a semi-analytic model has been developed to distinguish between mono- and multi-enriched second generation stars (Hartwig et al., 2018b). A further stochastic model has been developed to assess the source of [Eu/Fe] in metal-poor stars (Brauer et al., 2021). These come almost two decades after the empirical stochastic model proposed by McWilliam & Searle (1999).

1.4.1 Ultra faint dwarf galaxies

We are yet to distinguish between the metal-poor stars in the halo of the Milky Way and those in the surrounding dwarf galaxies. However, the ultra faint dwarf galaxies (UFDs) that orbit the Milky Way typically contain a metal-poor stellar population (Martin et al., 2008; Frebel, 2010; Ji et al., 2015). These UFDs may be close descendants of the first galaxies (Bromm & Yoshida, 2011). The proposed star formation histories of these UFDs are relatively simple (Tolstoy et al., 2009). They are thought to have experienced minimal star formation episodes and, as such, their stars may hold clues to the earliest episodes of chemical enrichment.

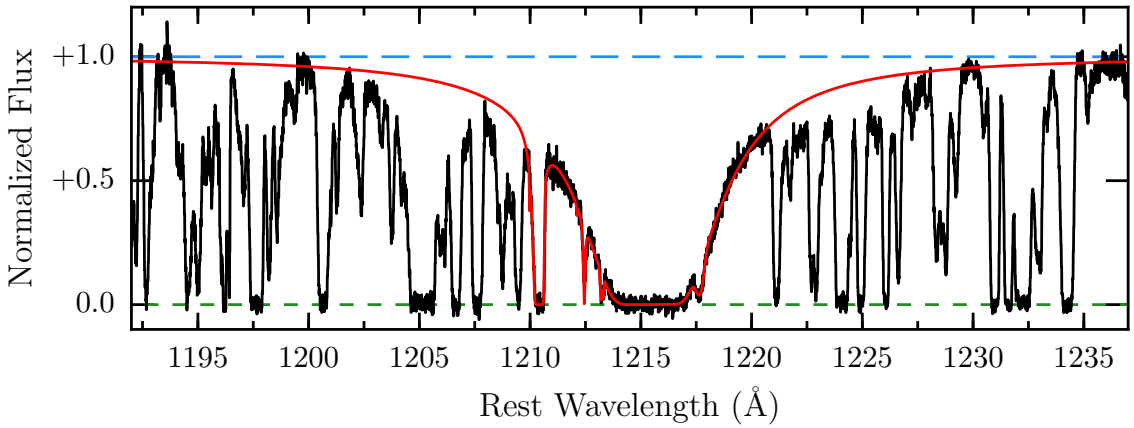

Figure 1.2. An example of the Lyα absorption of the DLA presented in Cooke et al. (2017). This is, in fact, the most metal-poor DLA currently known.

1.5 Damped Lyman-α systems

The ability of stellar relics to retain the Population III fingerprint locally cannot be overvalued. However, if we extend our investigation to the high redshift Universe, we can directly search for the gas enriched by the first SNe.

To study gas in the high redshift Universe, we rely on a technique known as quasar absorption line spectroscopy. This process uses light from an unrelated, background quasar to study intervening gas on the line-of-sight between the quasar and our telescope[2]. The intervening gas removes light from the spectrum of the quasar and, in turn, the resulting absorption can reveal properties of the gas cloud such as its redshift, metallicity, and kinematic properties.

Of particular interest to this thesis are the gas reservoirs with the largest column density of neutral hydrogen. A damped Lyman-α (DLA) system is an absorption line system with a column density of neutral hydrogen in excess of $N(\mathrm{H\,I}) > 10^{20.3}$ atoms per cm^2 (Wolfe et al., 2005). The Lyα absorption profiles of DLAs are imprinted with distinct damping wings (hence the name). An example of this profile is shown in Figure 1.2. The wings in the Lyα absorption are a consequence of natural broadening that becomes prominent at large column densities.

[2]It is also possible to use energetic explosions that occur within distant galaxies (i.e. gamma ray bursts) as the background light source.

1.5.1 Lessons from line profiles

The absorption profile of any atomic transition, like that of Lyα, can be modelled by a Voigt profile. The Voigt profile takes into account both the natural broadening expected from quantum mechanical effects and the Doppler broadening expected from motions of the atoms in the gas. Specifically, it is the convolution of a Lorentzian (that describes the natural broadening) and a Gaussian (that describes the Doppler broadening) (Mihalas, 1978). The Lorentzian profile is dependent on the properties of the transition, like the oscillator strength, the wavelength of the transition, and the column density of the atomic species. Thus, at the large column densities where the wings of this profile become prominent, we can readily determine the column density of the absorbing hydrogen. To determine further properties, such as the cloud kinematics and the metallicity, it is necessary to observe absorption features due to the metals associated with the gas reservoir.

1.5.2 Typical DLA properties

A benefit to DLAs is that the gas reservoirs of hydrogen are mostly neutral. Surveys have found that these DLAs contain the majority ($\gtrsim 80\%$) of neutral gas in the redshift interval $0 < z < 5$ (Péroux et al., 2003; Wolfe et al., 2005; Prochaska et al., 2005). Since neutral gas is needed to form H_2, and hence make stars, these reservoirs are the ideal environment for star formation (Wolfire et al., 2003). DLAs therefore contain the majority of fuel for star formation in the early Universe.

The large column density of neutral hydrogen means that DLAs are self-shielded from external radiation with photon energies between $13.6\,\mathrm{eV} \leq h\nu \leq 400\,\mathrm{eV}$ (Wolfe et al., 2005). A consequence of this is that the constituent metals reside in a dominant ionisation state that is determined by their respective ionisation potentials. This means that the observed transition of the dominant species (like O I and Fe II) can be used to determine

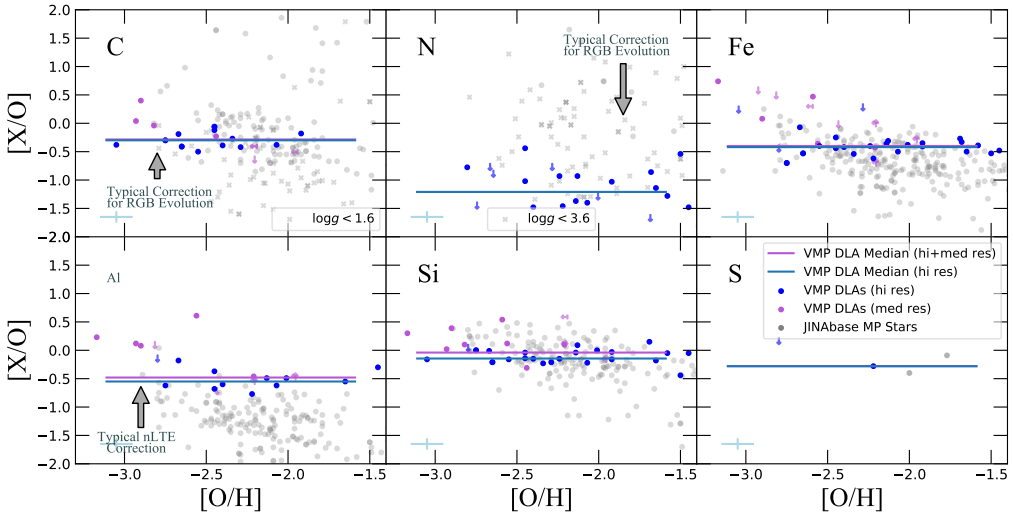

Figure 1.3. C, N, Fe, Al, Si, and S abundance ratios as a function of [O/H] from Haze Nuñez et al. (2021). The blue points show VMP DLAs with high resolution data. The purple are those with medium resolution data. The horizontal bars show the median VMP DLA abundance ratios with (purple) and without (blue) including the medium resolution spectra. The grey points are metal-poor stars from the JINA database (Abohalima & Frebel, 2018); the grey crosses are giants whose surface abundances have been altered by evolutionary processes. The red smaller points are ultra-faint/dwarf galaxies[3].

the column density of O and Fe without the need for ionisation corrections (Vladilo et al., 2001). This is not the case for lower column density systems (Viegas, 1995). DLAs are therefore the ideal environment to study the evolution of metals across cosmic time (Pettini et al., 1994; Prochaska et al., 2003; Rafelski et al., 2012). These works have found a generally increasing trend in metallicity as a function of time with a large degree of variance in any given redshift interval. Above $z > 2$, the typical DLA metallicity is $\sim 1/10\ Z_{\odot}$. As with stellar relics, it is the *most* metal-poor DLAs that may be imprinted with the chemical fingerprint of the first stars and, thus, of interest to this thesis.

1.5.3 The most metal-poor DLAs

The first survey of very metal-poor (VMP; [Fe/H] < -2) DLAs with a high resolution spectrograph revealed the abundances of [C/O] followed the same trend in [O/H] as

[3]The compilation of dwarf galaxies is from an online table compiled by Alexander Ji available at: `https://github.com/alexji/alexmods/`. The original references are provided in Haze Nuñez et al. (2021).

similarly metal-poor halo stars (Pettini et al., 2008). This consistency was reaffirmed with subsequent surveys (e.g. Cooke et al., 2011a,b) suggesting that the most metal-poor DLAs may be enriched by a similar, possibly primordial, population of stars as the stellar relics in the halo of the Milky Way. Indeed, the most metal-poor DLA currently known can be modelled with the yields of a Population III progenitor (Cooke et al., 2017). Given the similar trends in the abundances observed across the stellar and gaseous relics (see Figure 1.3 from Haze Nuñez et al. 2021), these DLAs may be the gas that form some Population II stars. To understand the relationship between the first stars, the stellar relics, and the most metal-poor DLAs, we must consider how metal-poor DLAs are related to cosmic structure.

The nature and variation of DLA host galaxies at high redshift is still unknown. The first DLA survey suggested that DLAs may be associated with the discs of high redshift galaxies (Wolfe et al., 1986). Then, an alternate theory arose that suggested DLAs are 'protogalactic' clumps that will evolve into modern day galaxies (Haehnelt et al., 1998). Searches for the emission from DLA host galaxies aim to illuminate this issue. Recently, the use of integral field spectrographs have proven to be fruitful tools for these searches (Péroux et al., 2011, 2012; Fumagalli et al., 2017; Mackenzie et al., 2019; Joshi et al., 2021). As has the Atacama Large Millimeter/submillimeter Array (ALMA) (e.g. Møller et al., 2018; Neeleman et al., 2018; Klitsch et al., 2021). Though the majority of searches have led to non-detections (Kulkarni et al., 2000; Fynbo et al., 2010; Fumagalli et al., 2015; Møller et al., 2018; Ranjan et al., 2020), there are now $\sim$ 20 known host galaxies associated with DLAs $z > 2$ (Krogager et al., 2017; Joshi et al., 2021). It is unclear whether the low detection rate of DLA host galaxies is due to observational challenges or whether it is an indication of the fraction of the population associated with active star formation. A review of observational efforts suggests there may be a steep relationship between the emission luminosity of the host galaxy and the metallicity of the DLA (Krogager et al., 2017). The detected systems are indeed skewed towards higher metallicities. The prospect of detecting the hosts of the most metal-poor DLAs may therefore be infeasible with current instruments. Consequently, we look to other means to determine their properties.

The mass of a DLA host galaxy may be indicated by the proposed 'mass-metallicity' relation (Ledoux et al., 2006; Murphy et al., 2007; Prochaska et al., 2008; Neeleman et al., 2013; Christensen et al., 2014). These studies find that DLAs with the largest velocity widths, which is used as a proxy for host mass, show the highest metallicities. If this relationship holds in the EMP regime, the most metal-poor DLAs are hosted in the lowest mass galaxies. Indeed, an analysis of the kinematics of VMP DLAs suggests that the most metal-poor DLAs are hosted by the lowest mass structures capable of forming stars at $z \sim 3$ (Cooke et al., 2015). This is based on a trend of decreasing velocity widths for increasingly metal-poor DLAs.

It has further been suggested that there is a link between metal-poor DLAs and the dwarf galaxy population; particularly, the *most* metal-poor DLAs and the UFDs (Cooke et al., 2015; Berg et al., 2015; Skúladóttir et al., 2018; Welsh et al., 2019). The analysis of the kinematics, chemistry, and physical properties of the most metal-poor DLAs highlight the parallels that can be drawn between these gas reservoirs in the early Universe and the local dwarf galaxy population. Though, see Yuan & Cen (2016) and Jeon et al. (2019) for an alternate picture.

The ancestral relationship between the most metal-poor DLAs and their local descendants is yet to be established. As is the relationship between these gas reservoirs and the stellar relics in both the halo of the Milky Way and the surrounding dwarf galaxies. Furthermore, the link between UFDs and the first galaxies is yet to be understood (Bromm & Yoshida, 2011). Studying the chemical enrichment of these environments may be one of the best tools at our disposal to draw parallels between them.

1.5.4 Finding these DLAs

Thanks to the Sloan Digital Sky Survey (SDSS), it has been possible to investigate the low metallicity tail of the DLA population for the last decade (Pettini et al., 2008; Penprase et al., 2010; Cooke et al., 2011b). The technique for identifying these metal-poor DLAs has been honed over the years and is currently a 3 step process: First, we exploit the SDSS spectroscopic data (R $\sim$ 1 500) to identify quasars with candidate EMP DLAs along their

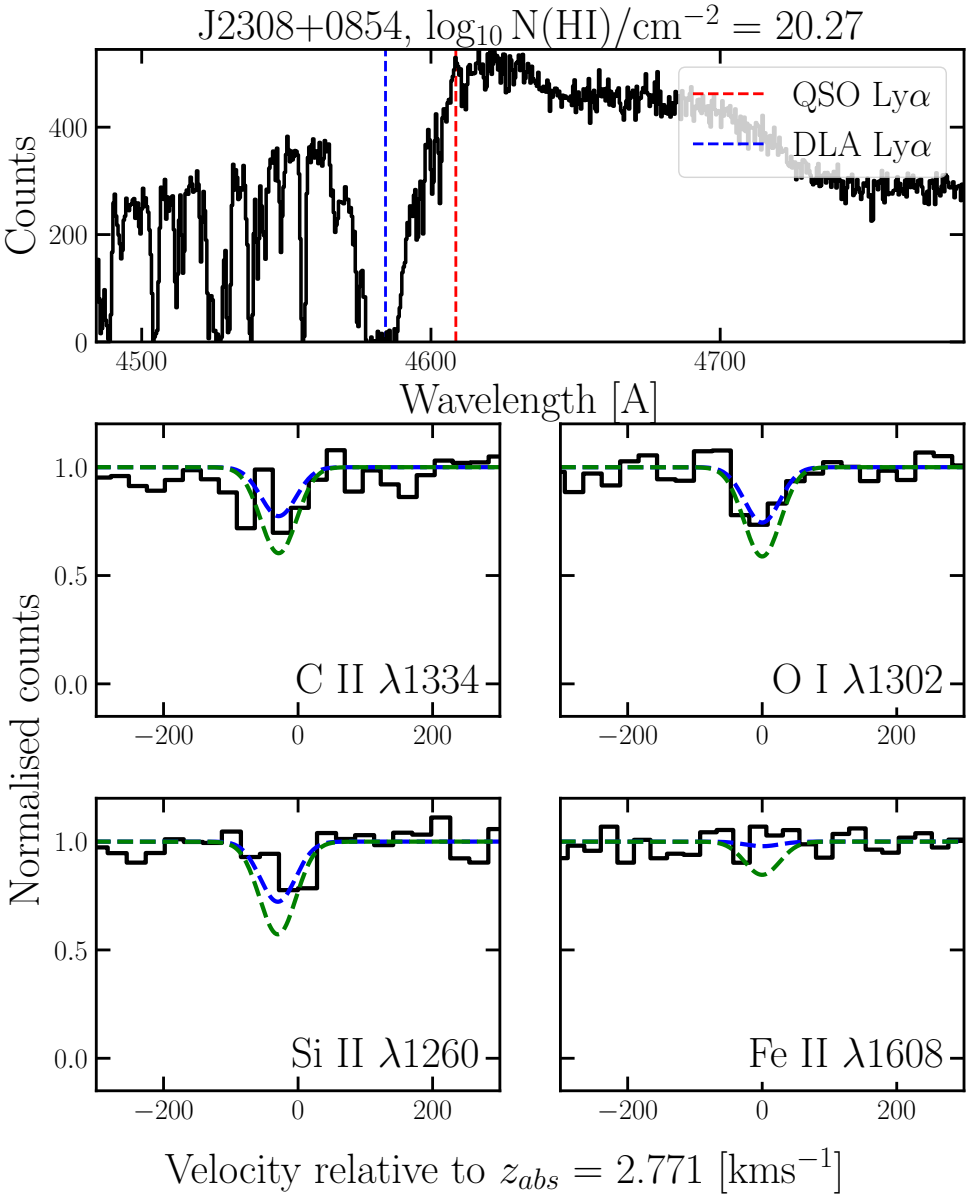

Figure 1.4. An example of a metal-poor DLA collected using WHT/ISIS ($R \sim 65$ km s^{-1}). The strongest metal lines typically associated with DLAs include C II λ1334, O I λ1302, Si II λ1260, and Fe II λ1608. The lack of absorption in the bottom four panels indicate this is an ideal candidate for follow up observations with a high resolution spectrograph. These data show a DLA observed in stage 2 of the discovery process described in the text. The blue and green dashed lines correspond to [Fe/H] = −3 and −2 respectively.

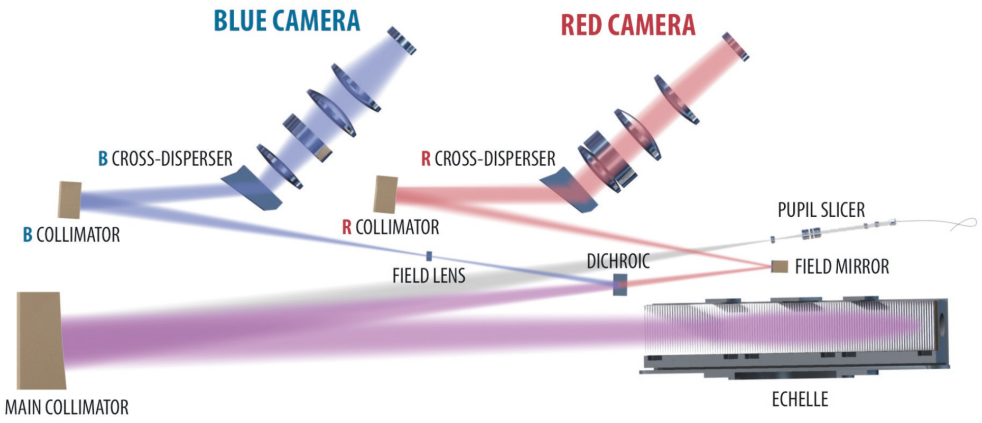

Figure 1.5. Light path of ESPRESSO from ESO ESPRESSO P108 manual. An early version of this figure is in Pepe et al. (2010).

sightline. These candidates are selected based on damped H I Lyα absorption combined with undetected absorption at the expected location of the associated metal lines (see Figure 1.4). Second, we collect follow up observations using an intermediate resolution spectrograph (R $\sim$ 4 000). Finally, the most promising candidates identified from this intermediate step (those that have the weakest – or undetected – metal absorption features) are then observed with a high resolution spectrograph (R $\sim$ 40 000) to reliably determine the detailed chemical abundances and cloud model of the system.

The typical velocity width of a metal-poor DLA is $\sim$ 10 km s^{-1}. Thus, these high resolutions are needed to avoid imprinting the instrument profile on the observed metal line profiles. High (R $\sim$ 40 000) resolution echelle spectrographs are typically mounted on 8 – 10 m telescopes. Though, the Echelle Spectrograph for Rocky Exoplanets and Stable Spectroscopic Observations (ESPRESSO; Pepe et al., 2010) on the Very Large Telescope (VLT) operated by the European Southern Observatory (ESO) is fed light from the four Unit Telescopes (UTs) in unison when operating in 4UT mode. To produce high resolution spectra, an echelle spectrograph takes advantage of high diffraction orders. The grating is optimised to diffract light at high incidence angles which is related to the diffraction order via:

$$\lambda m/d = \sin(\theta_i) + \sin(\theta_r) \tag{1.5.1}$$

λ is the wavelength, m is the order, d is the separation between grating grooves, and θ is the incident (subscript i) or diffracted (subscript r) angle defined relative to the normal

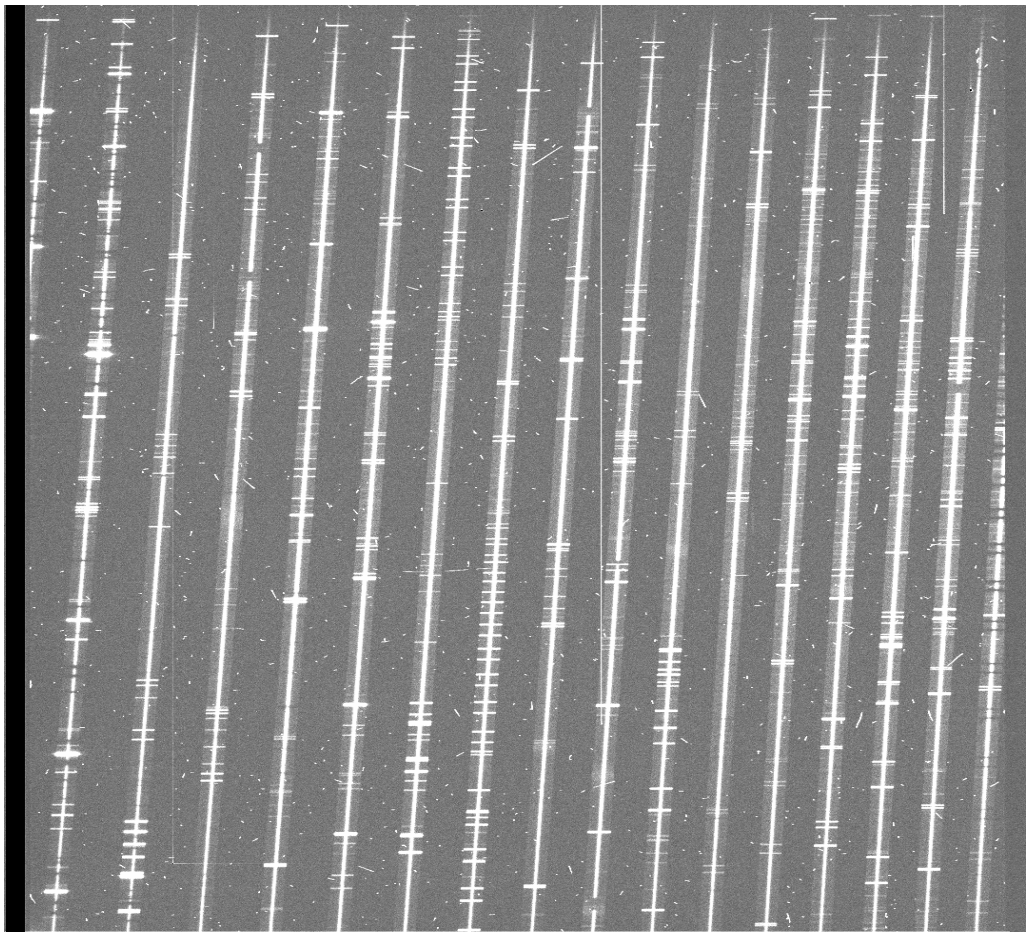

Figure 1.6. Example of a science frame collected with $R \sim 40\,000$ echelle spectrograph. Each vertical line represents a different echelle order; each line shows part of a single quasar spectrum, which can be stitched together during the data reduction.

of the grating. The resulting spectrum can then be passed through a cross-disperser to distinguish between light from overlapping orders (see Figure 1.5 for an example of the light path of ESPRESSO). The placement of this cross-disperser is such that the orders are separated in the spatial direction. Each echelle order is then projected onto different locations on a CCD (see Figure 1.6 for an example science frame). As part of the data reduction, each order is extracted and stitched together to make a single high resolution spectrum, that can then be processed, reduced, and analysed.

1.6 Thesis overview

This thesis aims to address how we can investigate the properties of the elusive first stellar population through their surviving chemistry. We hope to demonstrate what can be revealed about early structure formation and chemical evolution in the process. The number abundance of these stars, their typical mass range, and the energy with which they underwent core collapse influenced the rate of cosmic reionisation, the rate of metal enrichment, and the size of the first galaxies. Specifically, we investigate environments that may have been enriched by the first stellar population and use our analysis to identify the most useful chemical tracers of Population III enrichment.

In Chapter 2, we present a novel stochastic chemical enrichment model that can be used to investigate enrichment by both Population III and Population II stars. Previous investigations of the Population III IMF have been restricted to two scenarios: either the relic environments have been enriched by one Population III SN, or, they have been enriched by an IMF weighted abundance of elements. The true case is somewhere in between and this model has been developed to overcome this limitation. We display the utility of this model through an analysis of the most metal-poor DLAs currently known. In Chapter 3, we conduct a similar analysis using the abundances of metal-poor Milky Way halo stars. A comparison of these investigations allows us to draw parallels between the chemical enrichment of the gaseous and stellar relics.

Chapter 4 showcases the first bound on the carbon isotope ratio of a near-pristine DLA. This isotope ratio is a possible diagnostic of enrichment by the hypothetical low mass (~ 1 M$_\odot$) Population III stars. It can also be used as a 'chemical clock' to investigate the time frame of chemical enrichment. We use the entire known chemistry of this absorption line system to infer the enrichment timescale of the DLA towards J0035−0918.

Chapter 5 is dedicated to investigating the [O/Fe] abundances of the most metal-poor DLAs. Current observations suggest that VMP DLAs exhibit a plateau in [O/Fe] $\sim +0.4$. There is tentative evidence of an up-turn in the [O/Fe] abundances of DLAs in the EMP regime. This may be an empirical indication of enrichment from metal-free stars. We present the

precise [O/Fe] abundance determinations of two near-pristine DLAs to investigate this trend.

We summarise the work presented in this thesis in Chapter 6 and suggest possible avenues of future work.

CHAPTER 2

Modelling the chemical enrichment of Population III supernovae: the origin of the metals in near-pristine gas clouds

---

The following chapter is reprinted from the publication "Modelling the chemical enrichment of Population III supernovae: The origin of the metals in near-pristine gas clouds" (Welsh et al., 2019). In this paper, we present a novel stochastic chemical enrichment model and use it to investigate the properties of the first stars using the chemistry of the most metal-poor DLAs. This model estimates the number of massive Population III SNe that have enriched these DLAs, along with their underlying mass distribution, and the typical explosion energy of their SNe. This model is motivated by the possibility that some relic environments may have been enriched by the yields of multiple SNe. Our main results suggest that the most metal-poor DLAs have been enriched by $N_{\star} \lesssim 72$ (2σ) massive stars, with masses $M \lesssim 40$ M$_{\odot}$. The underlying IMF is consistent with a Salpeter distribution. Due to the similarity between the Population III and Population II yields, we cannot distinguish whether these DLAs are predominantly enriched by first or second generation stars.

Abstract: The most metal-poor, high redshift damped Lyman α systems (DLAs) provide a window to study some of the first few generations of stars. In this paper, we present a novel model to investigate the chemical enrichment of the near-pristine DLA population. This model accounts for the mass distribution of the enriching stellar population, the typical explosion energy of their supernovae, and the average number of stars that contribute to the enrichment of these DLAs. We conduct a maximum likelihood analysis of these model parameters using the observed relative element abundances ([C/O], [Si/O], and [Fe/O]) of the 11 most metal-poor DLAs currently known. We find that the mass distribution of the stars that have enriched this sample of metal-poor DLAs can be well-described by a Salpeter-like IMF slope at $M > 10$ M$_\odot$ and that a typical metal-poor DLA has been enriched by $\lesssim 72$ massive stars (95 per cent confidence), with masses $\lesssim 40$ M$_\odot$. The inferred typical explosion energy ($\hat{E}_{\rm exp} = 1.8^{+0.3}_{-0.2} \times 10^{51}$ erg) is somewhat lower than that found by recent works that model the enrichment of metal-poor halo stars. These constraints suggest that some of the metal-poor DLAs in our sample may have been enriched by Population II stars. Using our enrichment model, we also infer some of the typical physical properties of the most metal-poor DLAs. We estimate that the total stellar mass content is $\log_{10}(M_\star/{\rm M}_\odot) = 3.5^{+0.3}_{-0.4}$ and the total gas mass is $\log_{10}(M_{\rm gas}/\ {\rm M}_\odot) = 7.0^{+0.3}_{-0.4}$ for systems with a relative oxygen abundance [O/H] ≈ -3.0.

2.1 Introduction

The first stars in the Universe necessarily formed out of a primordial environment, heralding an epoch known as the cosmic dawn, at a redshift of $z \sim 20 - 30$ (Barkana & Loeb, 2001). At high densities, collapsing primordial gas relied chiefly on molecular hydrogen, an inefficient coolant, to radiate energy and facilitate collapse. As a result, it is believed that primordial gas was unable to form low mass stars; instead, small multiples of relatively massive stars are thought to have formed in small clusters (Abel et al., 2002; Glover, 2013). Elements heavier than lithium, known as metals, were forged within the cores of these

first stars. When the first stars ended their lives, some as supernovae (SNe) explosions, the surrounding gas was enriched with these heavy elements, altering the process of all subsequent star formation. The incorporation of metals into star-forming gas facilitates numerous cooling pathways. Metal-enriched gas can therefore collapse and fragment more effectively than primordial gas. The unique formation history of the first, metal-free, population is expected to be evident from its stellar Initial Mass Function (IMF) — the characteristic mass of which is thought to be relatively larger than that of populations which form from metal-enriched gas.

Lacking direct observations, the most direct means to pin down the mass distribution of metal-free stars is to simulate their formation in a cosmological setting (e.g. Tegmark et al. 1997; Barkana & Loeb 2001; Abel et al. 2002; Bromm et al. 2002; Turk et al. 2009; Greif et al. 2010; Clark et al. 2011; Hirano et al. 2014; Stacy et al. 2016). Overall, these works indicate that the first stars, also known as Population III (or Pop III) stars, had masses in the range of $10 - 100$ $M_{\odot}$ and formed obeying a relatively bottom-light distribution compared with that of star formation today (see Bastian et al. 2010 for a recent review). These massive stars would have had distinctly short lifetimes; none could have survived long enough to be observed today. The fact that a metal-free star has yet to be detected, in spite of both historic and on-going surveys (e.g. Bond 1980; Beers et al. 1985; Ryan et al. 1991; Beers et al. 1992; McWilliam et al. 1995; Ryan et al. 1996; Cayrel et al. 2004; Beers & Carollo 2008; Christlieb et al. 2008; Roederer et al. 2014; Howes et al. 2016; Starkenburg et al. 2017), supports these theoretical works.

We can observationally probe the properties of this potentially extinct population via indirect methods. Namely, we search for the unique chemical fingerprint that metal-free stars leave behind once they explode as Type II core-collapse SNe. To reliably infer the properties of Population III stars, we must therefore isolate systems that have only been chemically enriched by the SNe of metal-free stars. Historically, this has been achieved by searching for surviving Extremely Metal-Poor (EMP) stars, which are characterised by

an iron abundance that is 1000 times less than that of the Sun[1] (see Beers & Christlieb 2005 and Frebel & Norris 2015 for a review of this field). These surviving EMP stars were among the second generation of stars to form in the Universe and may have been exclusively enriched by Population III SNe.

As suggested by Erni et al. (2006), Pettini et al. (2008), Penprase et al. (2010), and Crighton et al. (2016), it is also possible to search for the signatures of Population III stars in the large reservoirs of neutral hydrogen that are found along the line-of-sight towards unrelated, background quasars. The relative metal abundances of these gaseous systems are encoded with information about the stars that have contributed to their enrichment. Thus, the most metal-deficient systems are invaluable tools for studying the earliest episodes of chemical enrichment. Indeed, some of the most metal-poor gaseous systems may have been solely enriched by the first generation of stars (e.g. Crighton et al. 2016; Cooke et al. 2017) or, in some cases, remained chemically pristine (e.g. Fumagalli et al. 2011; Robert et al. 2019). In this work, we focus on the highest column density systems, $N(\mathrm{H\,I}) > 10^{20.3}\mathrm{cm}^{-2}$, known as Damped Lyman-$\alpha$ systems (DLAs). At these high column densities, the gas is self-shielding; hydrogen is predominantly neutral, while the other elements usually reside in a single, dominant ionisation state. Spectral absorption features associated with the dominant ionic species can therefore be used to determine the relative abundances of elements without the need for ionisation corrections. The oxygen abundance of these systems can be determined reliably because charge-transfer reactions ensure that oxygen closely follows that of hydrogen (Field & Steigman, 1971), and we expect dust depletion to be minimal for oxygen (e.g. Spitzer & Jenkins 1975), particularly in the lowest metallicity DLAs[2] (Pettini et al., 1997; Akerman et al., 2005; Vladilo et al., 2011; Rafelski et al., 2014). Since oxygen is predominantly sourced from the SNe of massive stars, it can be considered an informative tracer of chemical enrichment (Henry et al., 2000). Throughout this work, we therefore characterise the metallicity of DLAs using their oxygen abundance.

[1]The use of iron as a metallicity tracer is a consequence of our ability to reliably detect its associated absorption features in stellar spectra.

[2]In addition, provided that an optically thin O I absorption line is available, the determination of the O I column density, and hence the oxygen abundance, does not depend on the geometry or kinematics of the gas cloud.

The most metal-poor DLAs are typically studied at $z \sim 3$, when the age of the Universe is ~ 2 Gyr, therefore, there is a possibility that some of these gas clouds were enriched by subsequent generations of Population II stars. Furthermore, even if all of the metals in near-pristine DLAs come from metal-free stars, it is currently unclear if these metals were produced by stars in the same halo; the minihalos in which the first stars formed are not thought to have evolved into the first galaxies (Bromm & Yoshida, 2011). The energetic SNe of the first stars are known to have disrupted the gas within these minihalos — likely to the point where substantial retention, and subsequent star formation, is implausible (Bromm et al., 2003; Greif et al., 2007, 2010). Therefore, if the chemical signature of metal-free star formation is detected in near-pristine DLAs, it may have migrated from its initial birthplace, through the intergalactic medium, and into the halos which now host the most metal-poor DLAs. Consequently, the metals in near-pristine gas clouds may represent the combined chemical imprint from multiple minihalos.

To explore this possibility, and to infer the physical properties of the first stars from the chemistry of EMP DLAs, we require nucleosynthesis simulations that follow the complete chemical evolution of a metal-free star from its initial phases through to the explosive burning phase of its eventual SN explosion. There are several independent groups that have refined this detailed calculation over the years (Woosley & Weaver, 1995; Chieffi & Limongi, 2004; Tominaga et al., 2006; Heger & Woosley, 2010; Limongi & Chieffi, 2012). The relative abundances of metals expelled by the first stars depend on various stellar properties. Parameters commonly considered in the SN calculations include the initial progenitor star mass, the explosion energy, and the mixing between stellar layers. The Woosley & Weaver (1995; hereafter WW95), Heger & Woosley (2010; hereafter HW10), and Limongi & Chieffi (2012; hereafter LC12) calculations all indicate that the ratio of the yields of carbon and oxygen expelled from the SNe of metal-free stars decreases almost monotonically with an increasing progenitor mass. HW10 also find that the ratio of silicon to oxygen, for a given progenitor mass, is sensitive to the explosion energy of the progenitor star.

In this paper, we present a novel stochastic enrichment model to investigate the properties

on an enriching population of metal-free stars using the relationships found in the HW10 yield set. Our stochastic enrichment model considers the mass distribution of an enriching population as well as the typical SN explosion energy. We employ this model to investigate the enrichment history of the 11 most metal-poor DLAs currently known beyond a redshift of $z = 2.6$. This analysis complements and extends recent work that approaches this same problem using EMP stars (e.g. Ji et al. 2015; Fraser et al. 2017; Ishigaki et al. 2018). We start by describing our model in Section 2.2. We summarise the data that are used in our analysis in Section 2.3 and discuss the results of this analysis in Section 2.4. In Section 2.5, we discuss the possibility of alternative sources of enrichment, the stability of our model, and infer some of the physical properties of the most metal-poor DLAs. We list our main conclusions and discuss the future applications of our model in Section 2.6.

2.2 Stochastic enrichment model

In this section, we describe our stochastic chemical enrichment model of Population III enriched systems. Throughout this work we use the definition:

$$[\mathrm{X/Y}] = \log_{10}\left(N_{\mathrm{X}}/N_{\mathrm{Y}}\right) - \log_{10}\left(N_{\mathrm{X}}/N_{\mathrm{Y}}\right)_{\odot} \tag{2.2.1}$$

which represents the number abundance ratio of elements X and Y, relative to the solar value. We focus our attention on the [C/O], [Si/O], and [Fe/O] ratios, as these elements are most commonly detected in near-pristine gas. We use the solar ratios as recommended by Asplund et al. (2009). The solar values associated with these elements are[3]: $\log_{10}\epsilon_{\mathrm{C}_\odot} = 8.43$, $\log_{10}\epsilon_{\mathrm{O}_\odot} = 8.69$, $\log_{10}\epsilon_{\mathrm{Si}_\odot} = 7.51$, and $\log_{10}\epsilon_{\mathrm{Fe}_\odot} = 7.47$.

Relative element abundance ratios can be determined to a precision of ~ 0.01 dex (e.g. Cooke et al., 2018), provided that the data are collected with a high spectral resolution ($R \gtrsim 40,000$) echelle spectrograph and are recorded at signal-to-noise ratio (S/N $\gtrsim 15$ per pixel; Wolfe et al., 2005). This high precision allows us to infer the properties of the stars that were responsible for the chemical enrichment of near-pristine gas (e.g. the stellar

[3] $\log_{10}\epsilon_{\mathrm{X}} = \log_{10}\left(N_{\mathrm{X}}/N_{\mathrm{H}}\right) + 12$.

mass distribution) and the details of the SN explosion that ended the progenitor stars' lives (e.g. kinetic energy, stellar mixing).

2.2.1 Mass distribution model and likelihood function

We model the mass distribution of metal-free stars as a power-law of the form $\xi(M) = k\,M^{-\alpha}$, where α is the power-law slope ($\alpha = 2.35$ for a bottom-heavy Salpeter IMF[4]), and k is a multiplicative constant that is set by defining the number of 'enriching stars', $N_\star$, that form between a minimum mass $M_{\rm min}$ and maximum mass $M_{\rm max}$, given by:

$$N_\star = \int_{M_{\rm min}}^{M_{\rm max}} k M^{-\alpha} {\rm d}M \ . \tag{2.2.2}$$

In this work, $N_\star$ therefore represents the number of stars in this mass range that have contributed to the enrichment of a system, i.e. the 'enriching stars'. Note that, in a given metal-poor DLA, the enriching stars may have formed in separate minihalos which later merged or had their chemical products mixed. In this sense, the chemistry of metal-poor DLAs may represent a relatively 'well-sampled' IMF of the first stars. In addition to the mass distribution, we also consider the typical SN explosion energy of the enriching stars $E_{\rm exp}$, which is a measure of the kinetic energy of the SN ejecta at infinity.

Using a sample of the most metal-poor DLAs, and their constituent abundance ratios, we can investigate the likelihood of a given enrichment model by calculating the probability of the observed abundance ratios, R_o, given the abundance ratios expected from that enrichment model, R_m:

$$\mathcal{L} = \prod_n p_n(R_o|R_m) \ , \tag{2.2.3}$$

where n refers to the $n^{\rm th}$ metal-poor DLA in our sample. The probability of an observed abundance ratio (e.g. [C/O]) is given by

$$p_n\big(R_o|R_m\big) = \int p\big(R_o|R_i\big) p\big(R_i|R_m\big) {\rm d}R_i \ . \tag{2.2.4}$$

[4]i.e. the first local measurement of the stellar IMF (Salpeter, 1955). See Chabrier (2003) for an alternative functional form.

The first term of this integral describes the probability of a given observation being equal to the intrinsic (i.e. true) abundance ratio of the system, R_i. This distribution is modelled by a Gaussian, where the spread is given by the observational error on the chemical abundance ratio. The second term of the integral in Equation 2.2.4 describes the probability of obtaining the intrinsic abundance ratio given the IMF defined in Equation 2.2.2 combined with the nucleosynthesis calculations of the ejecta from the enriching stars. Our sample of the most metal-poor DLAs have a minimum of two observed abundance ratios — both [C/O] and [Si/O] (see Section 2.3). Therefore, in this work, the probability of a system's chemical composition is given by the joint probability of these abundance ratios for a given enrichment model. For the systems that also have an [Fe/O] determination, the probability density is extended to include this ratio as well.

Our model contains five parameters: $N_\star$, α, $M_{\rm min}$, $M_{\rm max}$, and $E_{\rm exp}$. In the case of a well-sampled IMF, $R_i = R_m$; however, as the first stars are thought to form in small multiples (Turk et al., 2009; Stacy et al., 2010), the number of enriching stars is expected to be small. Thus, the IMF of the first stars is stochastically sampled. Due to the stochasticity of the IMF, we have to construct abundance ratio probability distributions, $p(R_i|R_m)$, for each combination of our fiducial model parameters. The range of model parameters we consider are:

$$\begin{aligned} 1 \leq \quad & N_\star & \leq 100\,, \\ -5 \leq \quad & \alpha & \leq 5\,, \\ 20 \leq \quad & M_{\rm max}/{\rm M}_\odot & \leq 70\,, \\ 0.3 \leq \quad & E_{\rm exp}/10^{51}{\rm erg} & \leq 10\,. \end{aligned}$$

In what follows, we assume that stars with masses > 10 M$_\odot$ are physically capable of undergoing core-collapse. Therefore, this parameter is fixed at a value $M_{\rm min} = 10$ M$_\odot$. We also consider a maximum mass, $M_{\rm max}$, above which all stars are assumed to collapse directly to a black hole, and do not contribute to the chemical enrichment of their surroundings. We impose a uniform prior of $20 < M_{\rm max}/{\rm M}_\odot < 70$ on the maximum mass of the enriching stars — this upper bound corresponds to the mass limit above which pulsational pair-instability

SNe are believed to occur (Woosley, 2017). Similarly, we impose a uniform prior on the explosion energy, a choice that is driven by the yield set utilised in this analysis. We describe these nucleosynthesis yields in more detail in the following section. The explored range of $E_{\rm exp}$ covers all feasible explosion energies given our current understanding of core-collapse SNe.

2.2.2 Ejecta of metal-free stars

Our analysis relies on simulations of the evolution and eventual SN explosions of massive metal-free stars. In our work, we adopt the HW10 yields as our fiducial model and utilise the yields of WW95 and LC12 as points of comparison. In HW10, the nucleosynthetic yields of elements expelled from the SNe of massive metal-free stars are calculated as a function of the progenitor star mass, explosion energy, and the degree of mixing between the stellar layers.

The main impediment to the rigour of these SNe yield calculations is the uncertainty surrounding the ultimate explosion of a massive star (e.g. Melson et al. 2015). To overcome this, the simulations are performed in one dimension and the explosion is parameterised by a mixing prescription combined with a piston (i.e. a time-dependent momentum deposition that is characterised by a final kinetic energy of the ejecta at infinity, $E_{\rm exp}$). In HW10, the width of the mixing region is defined as a fraction of the He core size. Their simulations consider 14 mixing widths. However, they recommend adopting a width that is 10 per cent of the He core size, as this provides the best fit to observations of the light curve of SN 1987A. These model yields have been found to provide good fits to the abundance patterns of EMP stars, specifically those from Cayrel et al. (2004). However, we note that to properly account for mixing driven by Rayleigh-Taylor instabilities and rotation it is necessary to perform these simulations in two or three spatial dimensions (e.g. Joggerst et al. 2010a,b; Vartanyan et al. 2018). Further simplifications arise from performing these simulations in isolation, for non-rotating stellar models with negligible magnetic fields and no mass loss. The incorporation of rotation has been shown to induce additional mixing between stellar layers and lead to modest mass loss (Ekström et al.,

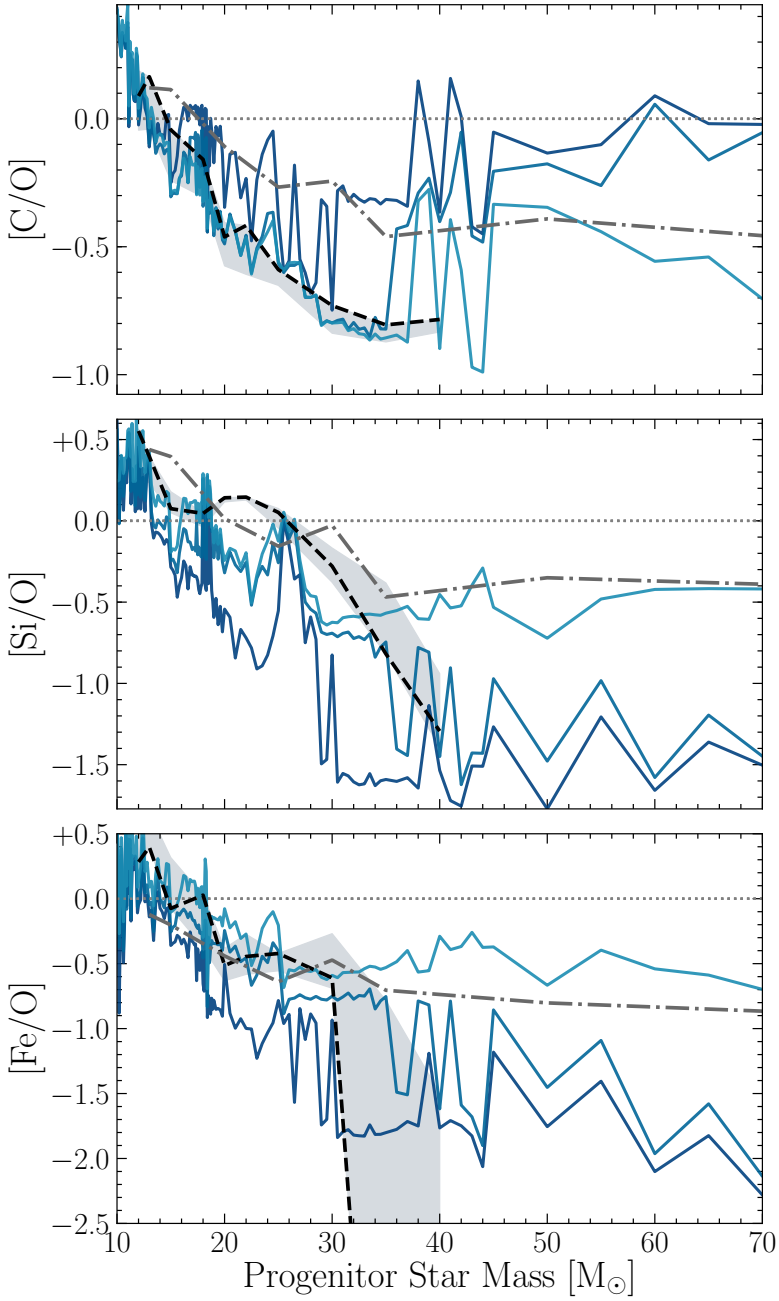

Figure 2.1. Relationship between the ejected [C/O], [Si/O], and [Fe/O] abundance ratios as a function of the stellar progenitor mass for a range of explosion energies. The dark blue line corresponds to a 1.2 B explosion while the progressively lighter lines correspond to a 1.8 B and 5 B explosion respectively (note 1 B = 10^{51}erg). Yields are taken from HW10 and are shown relative to the solar values recommended by Asplund et al. 2009. The solar abundances are marked by the horizontal dotted grey line. The dashed black curves show the abundance ratios expected from a progenitor with a metallicity 10^{-4} that of the Sun ($Z_{\odot}$); these yields are taken from WW95 for a typical explosion energy of 1.2 B. Also shown, via the dot-dashed grey lines, are the yields of massive metal-free stars as calculated by LC12. The explosion energy associated with these progenitors is $\sim$ 1 B, however the precise value varies with progenitor mass (as for the WW95 yields). The grey-shaded region encompasses the yields expected from all stars in a metallicity range of $10^{-4} < Z/Z_{\odot} < 1$, based on the yields computed by WW95.

2008). Work by Yoon et al. (2012) has suggested that this mass loss increases in the presence of magnetic torques.

The parameter space explored by HW10 spans masses from $(10 - 100)$ $M_\odot$ and explosion energies from $(0.3 - 10) \times 10^{51}$ erg. This space is evaluated across 120 masses and 10 explosion energies. The average mass spacing between successive yield calculations is $< 1M_\odot$ (and in some cases, as low as $0.1\,M_\odot$). For comparison, the average mass spacing in LC12 is $> 4M_\odot$. As can be seen from Figure 2.1, the ejected yields fluctuate rapidly across a small range of progenitor star masses. The HW10 calculations are the only yield calculations with a mass spacing small enough to account for this behaviour, which is thought to arise due to the non-linear interactions between the burning shells within a star (Müller et al., 2016; Sukhbold et al., 2018). Utilising the HW10 yields enables us to investigate the properties of our enriching stars with a finer mass resolution than would be afforded by other yield models.

As can be seen from Figure 2.1, the [C/O] abundance ratio evolves almost monotonically with progenitor mass for stars that explode with an energy $\gtrsim 1.8$ B and are < 40 $M_\odot$. The shells in which carbon and oxygen form are relatively close to the surface of a star; for explosions above ~ 1.8 B, these outer layers are mostly ejected. However, elements closer to the iron peak, like silicon and iron, are more dependent on the energy of the explosion, and are more likely to fall back onto the newly formed central compact object. Therefore, the combined analysis of the [C/O] and [Si/O] ratios of a system enriched by one SN would place constraints on the mass and explosion energy of the enriching star. Section 2.2.3 describes how we extend this to systems that have been enriched by a small number of stars, as opposed to just a single star.

As a point of comparison, the grey shaded regions in Figure 2.1 indicate the yields of massive Population II and Population I stars calculated by WW95. This comparison suggests that the relative yields of the most abundant elements are almost indistinguishable between metal-free and metal-enriched massive stars. Given the similarity of the yields of these elements across different stellar populations, we use the HW10 models owing to their fine mass resolution and the large grid of explosion energies, regardless of whether

the most metal-poor DLAs were enriched by Pop. III or Pop. II stars. We consider the potential of enrichment from alternative sources in Section 2.5.

2.2.3 Model abundance ratios

The first stars likely formed in small multiples, which necessarily means that their underlying mass distribution is stochastically sampled. To account for this, we construct abundance ratio probability distributions using Monte Carlo simulations. For a given IMF model, we stochastically sample the distribution and use the resulting progenitor star masses to calculate the total yield of C, O, Si, and Fe, based on the HW10 simulations. For the case of [C/O], the total yield of carbon and oxygen supplied by all of the stars is used to determine the resulting number abundance ratio:

$$N_{\rm C}/N_{\rm O} = m_{\rm O}/m_{\rm C}\frac{\sum_{i=1}^{N_\star} M_{{\rm C},i}}{\sum_{i=1}^{N_\star} M_{{\rm O},i}} \tag{2.2.5}$$

where $m_{\rm C}$ and $m_{\rm O}$ are the masses of a single carbon and oxygen atom, respectively; $M_{{\rm C},i}$ and $M_{{\rm O},i}$ are the masses of these elements that are expelled from the SN of star i within the multiple. From this we obtain a stochastically sampled [C/O] ratio. This is repeated 10^3 times to construct the probability density function, $p(R_i|R_m)$ in Equation 2.2.4, of [C/O] for a given mass distribution model and explosion energy. In actuality this sampling procedure is performed for [C/O], [Si/O], and [Fe/O] simultaneously and we consider the 3D joint probability density function of all of the ratios. In Figure 2.2 we have marginalised over both [Si/O] and [Fe/O] to illustrate the sensitivity of each model parameter to the resulting [C/O] distribution. The successive panels correspond to changing the slope, number of enriching stars, minimum mass, maximum mass, and explosion energy respectively. The example model parameters used in Figure 2.2 (grey-dashed curves) are: $\alpha = 2.35$, $N_\star = 6$, $M_{\rm min} = 10$ M$_\odot$, $M_{\rm max} = 35$ M$_\odot$, and $E_{\rm exp} = 1.8$ B. Note that when we compare the observed abundance ratios of a sample of systems to those from the adopted HW10 yields, we are assuming that all of the SNe that enriched these systems are well-modelled by the

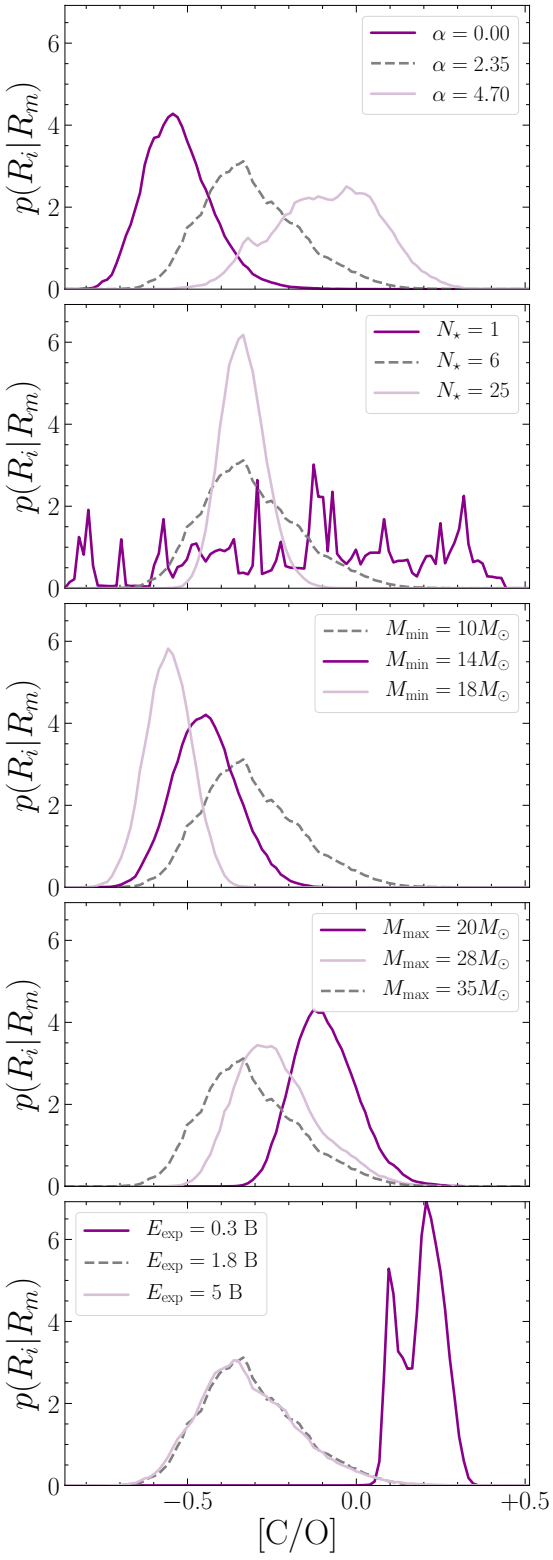

Figure 2.2. The [C/O] distribution for a range of enrichment models. The successive panels correspond to changing the slope, number of enriching stars, minimum mass, maximum mass, and explosion energy, respectively. Unless otherwise stated in the legend, the model parameters of these distributions are $\alpha = 2.35$, $N_\star = 6$, $M_{\rm min} = 10$ M$_\odot$, $M_{\rm max} = 35$ M$_\odot$, and $E_{\rm exp} = 1.8$ B (displayed as the grey dashed line in all panels as a point of comparison).

same explosion energy. It is likely that SNe with a range of explosion energies contributed to the enrichment of metal-poor DLAs. Due to computational limitations, we cannot treat the explosion energies of individual stars stars independently; our chosen prescription should therefore be considered to represent the 'typical' $E_{\rm exp}$ of the enriching stars. In the future we may consider a mass dependent explosion energy. However, the present generation of explosive nucleosynthesis models are not quite at the point whereby the kinetic energy released by the SN explosion is known as a function of the progenitor mass. Indeed, the expected functional form may not be parametric at all; recent calculations suggest that there are 'islands of explodability' for massive stars (e.g. Sukhbold et al. 2018). Furthermore, the latest models of core-collapse SNe by Müller et al. (2019) indicate that $\sim 10\,{\rm M}_{\odot}$ stars tend to yield somewhat low kinetic energy (~ 0.3 B). Given the uncertainty surrounding the appropriate parameterisation, we favour our chosen prescription due to its simplicity and reserve the consideration of alternatives for future investigations. We can nevertheless consider how our assumption might impact our inferred parameter values. For a given value of $N_{\star}$, our model assumes that all stars explode with the same final kinetic energy at infinity. If we were to allow every star to explode with a different energy, this likely produces a greater diversity of the element abundances ratios, thus broadening the $p(R_i|R_m)$ distribution. As the second panel of Figure 2.2 highlights, reducing the number of stars that have enriched a system also broadens the distribution of allowed abundances. Consequently, we may infer a lower $N_{\star}$ to account for the spread of a given abundance observed within our sample.

One of the underlying assumptions of Equation 2.2.5 is that the metals ejected by the first stars were uniformly mixed. Considering the time between the first episodes of enrichment and when the metal-poor DLAs in our sample have been observed, it is likely that the enriched gas within these systems has had sufficient time to become well-mixed (see e.g. Webster et al. 2015b). In any case, when we measure the relative element abundances of a gas cloud, we are taking the average across the entire sightline. Therefore, the measured abundance ratio of a given gas cloud should be representative of the number ratio in Equation 2.2.5 even if it contains pockets of unmixed SNe ejecta.

2.2.4 Likelihood sampling technique

The likelihood function (Equation 2.2.3) is sampled using a Markov Chain Monte Carlo (MCMC) procedure. We utilise the EMCEE software package (Foreman-Mackey et al., 2013) for this purpose. We draw 8.4×10^5 samples across 400 walkers each taking 2100 steps. We adopt a conservative burn-in that is half the length of the original chains. We consider the chains converged once doubling the number of steps taken by each walker has no impact on the resulting parameter distributions. We also repeat the analysis using a different seed to generate the initial randomised positions of the walkers. As our results do not change, this provides an additional test of convergence. We display the results of our MCMC analysis using the CORNER software package (Foreman-Mackey, 2016). To check that our results are not driven by a single observational data point within our sample we perform a bootstrap analysis to gauge the sampling error associated with our maximum likelihood estimates.

2.3 Data

Our sample consists of the abundance ratios of the most metal-poor DLAs currently known. Specifically, that of [C/O], [Si/O], and when available, [Fe/O]. These abundances have been determined from high resolution spectra taken with either the ESO Ultraviolet and Visual Echelle Spectrograph (UVES; Dekker et al. 2000) or the Keck High Resolution Echelle Spectrometer (HIRES; Vogt et al. 1994). In Table 2.1, we list the chemical abundances of these systems.

We focus on DLAs with a redshift of $z \geq 2.6$ to minimise the potential for enrichment from later generations of star formation (Welsh et al, in prep). Other possible sources of enrichment will be discussed in Section 2.5. Figure 2.3 shows the joint [C/O], [Si/O], and [Fe/O] abundance ratios of the systems in our sample. These data are overplotted on the joint probability distribution of [C/O] versus [Si/O] (left) and [Si/O] versus [Fe/O] (right) given the same example model shown in Figure 2.2. To offer a point of comparison,

Table 2.1. Abundance ratios of metal-poor gas clouds with known hydrogen column densities

QSO	$z_{\rm abs}$	$\log_{10}$ N(H I)	[Fe/H]	[O/H]	[C/O]	[Si/O]	[Fe/O]	References
J0140–0839	3.6966	20.75	−3.45 ± 0.24	–2.75 ± 0.05	–0.30 ± 0.08	0.00 ± 0.09	–0.70 ± 0.19	1,2
J0311–1722	3.7340	20.30	< −2.01	–2.29 ± 0.10	–0.42 ± 0.11	–0.21 ± 0.11	< +0.28	2
J0903+2628	3.0776	20.32	< −2.81	–3.05 ± 0.05	–0.38 ± 0.03	–0.16 ± 0.02	< +0.24	3
Q0913+072	2.6183	20.34	−2.82 ± 0.04	–2.40 ± 0.04	–0.36 ± 0.01	–0.15 ± 0.01	–0.42 ± 0.04	4,5
J0953–0504	4.2029	20.55	−2.95 ± 0.21	–2.55 ± 0.10	–0.50 ± 0.03	–0.16 ± 0.03	–0.40 ± 0.22	6
J1001+0343	3.0784	20.21	−3.18 ± 0.15	–2.65 ± 0.05	–0.41 ± 0.03	–0.21 ± 0.02	–0.53 ± 0.15	2
J1016+4040	2.8163	19.90	...	–2.46 ± 0.11	–0.21 ± 0.05	–0.05 ± 0.06	...	5
Q1202+3235	4.9770	19.83	−2.44 ± 0.16	–2.02 ± 0.13	–0.33 ± 0.11	–0.43 ± 0.09	–0.42 ± 0.18	7
J1337+3153	3.1677	20.41	−2.74 ± 0.30	–2.67 ± 0.17	–0.19 ± 0.11	–0.01 ± 0.10	–0.07 ± 0.31	8
J1358+6522	3.0673	20.50	−2.88 ± 0.08	–2.34 ± 0.08	–0.27 ± 0.06	–0.23 ± 0.03	–0.54 ± 0.08	4,9
J2155+1358	4.2124	19.61	−2.15 ± 0.25	–1.80 ± 0.11	–0.29 ± 0.08	–0.07 ± 0.06	–0.35 ± 0.26	10

1: Ellison et al. (2010), 2: Cooke et al. (2011b), 3: Cooke et al. (2017), 4: Cooke et al. (2014), 5: Pettini et al. (2008), 6: Dutta et al. (2014), 7: Morrison et al. (2016), 8: Srianand et al. (2010), 9: Cooke et al. (2012), 10: Dessauges-Zavadsky et al. (2003)

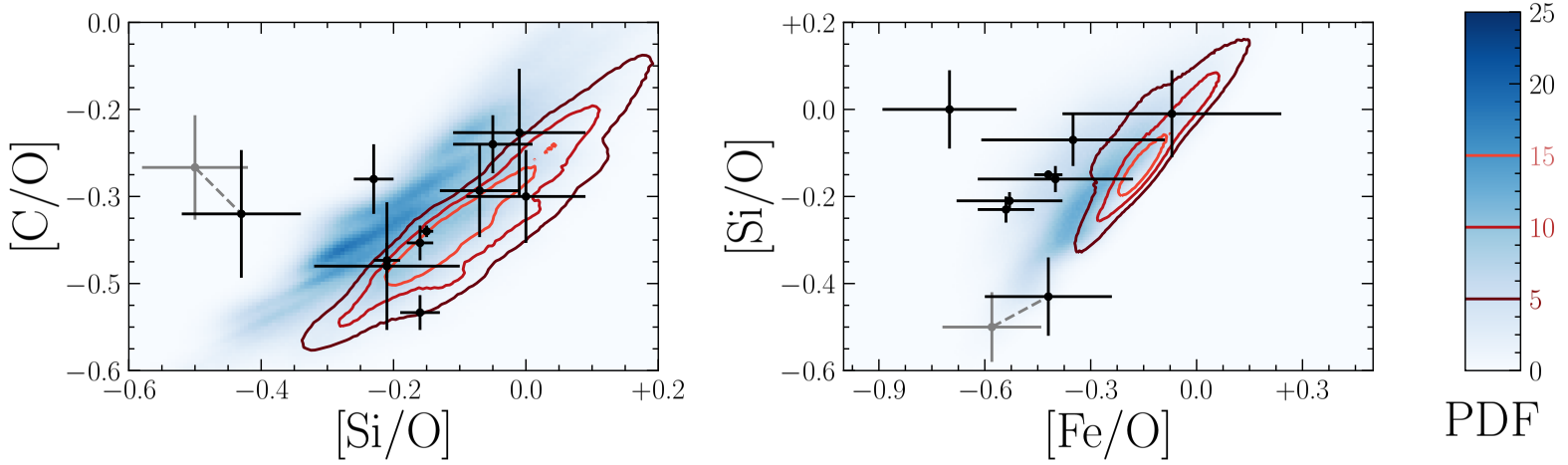

Figure 2.3. The [C/O], [Si/O], and [Fe/O] abundance ratios of the high redshift ($z \geq 2.6$) systems used in our analysis (black symbols with error bars) overplotted on the joint probability distributions (blue shaded distributions) of [C/O] and [Si/O] (left) and [Si/O] and [Fe/O] (right) of an example model where $\alpha = 2.35$, $N_\star = 6$, $M_{\rm min} = 10\ {\rm M}_\odot$, $M_{\rm max} = 35\ {\rm M}_\odot$, and $E_{\rm exp} = 1.8$ B (i.e. the same example model shown by the grey dashed curves in Figure 2.2). The red contours show the same joint probability distributions for the case of a 5 B explosion. The colours of the contours correspond to the probability region they encompass (as indicated on the colourbar). The grey data points highlight the abundance ratios of the sub-DLA along the line-of-sight towards Q1202+3235 adopted by Morrison et al. (2016). The grey dashed lines connect these data to that adopted in this work (black symbols; see text).

we also overplot the abundance ratio distributions for an explosion energy of 5 B (red contours), with all other model parameters unchanged. This highlights the sensitivity of [Si/O] and [Fe/O] to the explosion energy. In this figure, we display two different abundance determinations of the sub-DLA at $z_{\rm abs} = 4.9770$ along the line-of-sight to the quasar Q1202+3235. The authors of the discovery paper (Morrison et al., 2016) model the absorption system with multiple velocity components. Some of these velocity components show C II and Si II absorption features without corresponding O I absorption, indicating the presence of ionised gas. Morrison et al. (2016) measure the total element column densities of the system by summing over all of the velocity components and performing ionisation corrections. Instead, we prefer to solely consider the uncorrected column densities of the *primary* velocity component, which shows corresponding absorption from O I, C II, and Si II (i.e. the absorption component at $z_{\rm abs} = 4.977004$, which is the absorption predominantly arising from neutral gas). In each panel of Figure 2.3, the chemical abundance reported by Morrison et al. (2016) is shown by a grey symbol and is connected to our determination (black symbol) by a grey dashed line. Our determination results in a lower [C/O] and [Fe/O] ratio as well as a higher [Si/O] ratio.

2.4 Fiducial model analysis

Our fiducial model assumes that stars with masses above 10 $M_\odot$ can undergo core-collapse. We therefore impose a hard prior on the lower mass bound of our model IMF. The remaining model parameters are free to vary within limited bounds, as described in Section 2.2. In Figure 2.4, we show the posterior distributions (black histogram; diagonal panels) and 2D projections (grey contours) of the model parameters, based on the 11 most metal-poor DLAs at redshift $z \geq 2.6$. In the following subsections we discuss each parameter distribution individually. Throughout, the quoted errors on our maximum likelihood estimates are found using a bootstrap analysis of these data. The errors indicate the stability of our maximum likelihood estimates by measuring the variability of this statistic across multiple

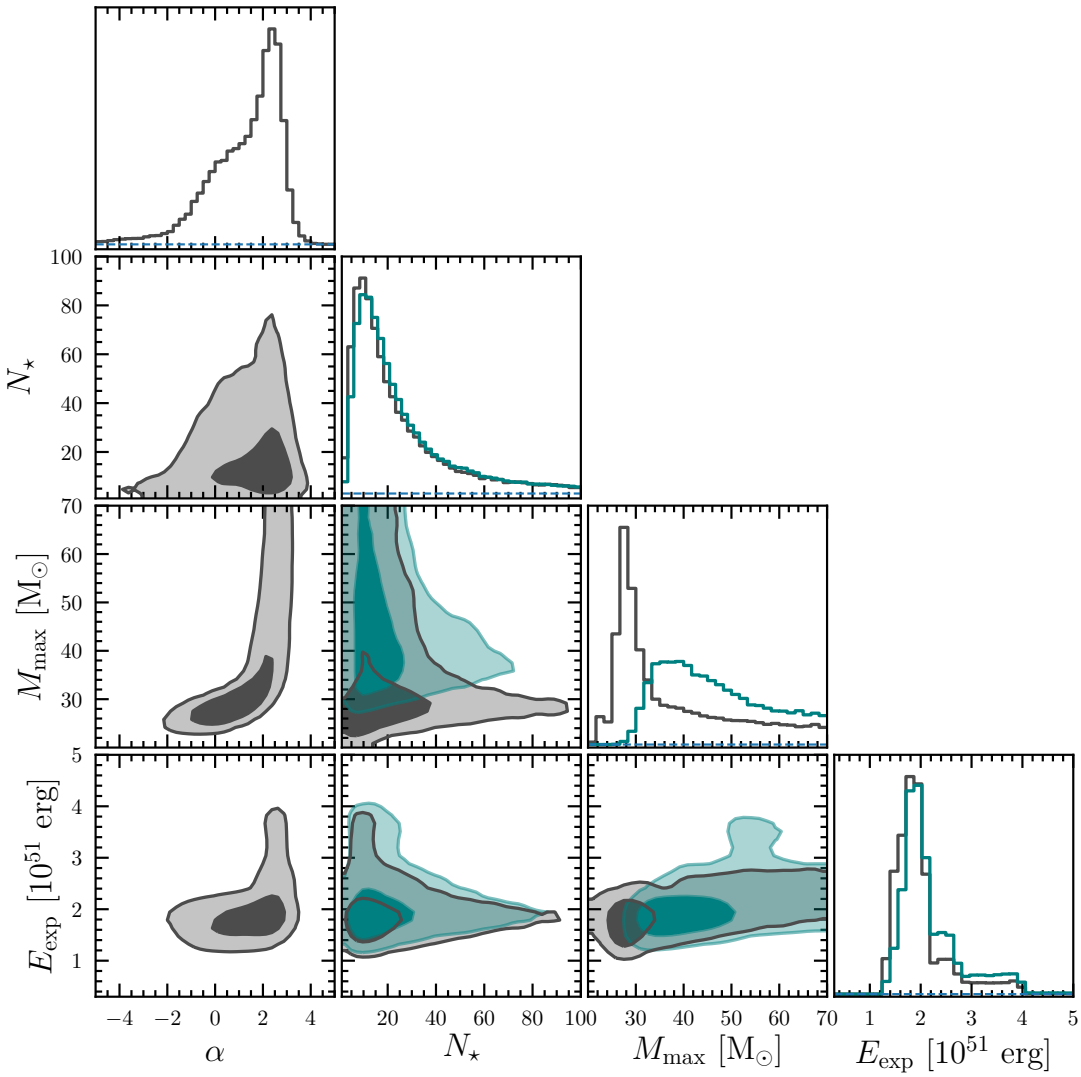

Figure 2.4. The marginalised maximum likelihood distributions of our fiducial model parameters (main diagonal), and their associated 2D projections, given the high redshift, metal-poor DLAs listed in Table 2.1. The dark and light contours show the 68 per cent and 95 per cent confidence regions of these projections respectively. The horizontal blue dashed lines mark where the individual parameter likelihood distributions fall to zero. The grey distributions correspond to the analysis of the full parameter space, described in Section 2.2. The green distributions are the result of imposing a Salpeter slope for the IMF (i.e. $\alpha = 2.35$).

data realisations. Specifically, they are the 68 per cent confidence regions around the median maximum likelihood estimates across all bootstraps.

2.4.1 Slope

The maximum likelihood estimate of the slope parameter is $\hat{\alpha} = 2.5 \pm 0.2$. Within the bootstrapped errors, this estimate encompasses a Salpeter distribution. Our result is therefore consistent with empirical determinations of the power-law slope of the IMF at $M \gtrsim 1\ \mathrm{M}_{\odot}$. However, there is a broad tail towards a flatter, and even top heavy, slope. Given the broad range of α values recovered by our fiducial model, we have recalculated the results after imposing a strong Salpeter-like prior on the slope parameter, $\alpha = 2.35$. The result of this analysis is overplotted in Figure 2.4 (green contours). The distributions of $N_{\star}$ and E_{exp} are virtually unchanged under the assumption of a Salpeter IMF, while the M_{max} distribution is broadened and shifted towards a higher mass limit. This suggests that the enrichment of the systems in our sample can be well-described by stars drawn from a Salpeter-like IMF. A Salpeter-like IMF could indicate that the chemical signature of the DLAs in our sample are dominated by the contribution from second generation stars. However, further work is needed to distinguish the signature of Population II versus Population III enrichment. To isolate the chemical signature of the first stars, we should restrict our analysis to the *most* metal-deficient DLAs, ideally, those with [O/H] < -3. Currently, there are not enough systems known within this regime to implement such an analysis — only one system, J0903+2628, has been found with an oxygen abundance [O/H] < -3 (Cooke et al., 2017).

2.4.2 Enriching stars

As can be seen in the second panel of Figure 2.2, the *intrinsic* spread of the relative element abundance ratios is sensitive to the sampling of the IMF. Specifically, the distribution of [C/O] becomes more centrally concentrated as more stars enrich each system (i.e. in the limit of a well-sampled IMF, all DLAs would exhibit an almost identical [C/O] ratio).

Thus, if the scatter between the data points is larger than the quoted errors, then we can use the scatter to probe the sampling of the IMF. For our fiducial model, the maximum likelihood estimate of the number of enriching stars is $\hat{N}_\star = 10 \pm 4$. The 95$^{\text{th}}$ percentile of this distribution suggests $N_\star \lesssim 72$. These statistics are unchanged under the assumption of a Salpeter IMF. From this, we conclude that a typical DLA in our sample has been enriched by a small number of massive stars.

2.4.3 Maximum mass

The maximum likelihood estimate of the upper mass limit of enriching stars is $\hat{M}_{\text{max}} = (28 \pm 1)\ \text{M}_\odot$. The interquartile range of this distribution spans $(28-45)\ \text{M}_\odot$. As can be seen in Figure 2.4, the posterior distribution on M_{max} has a broad tail towards high progenitor masses. This should be expected, since the data are consistent with a bottom-heavy IMF. This means that stars preferentially form with lower masses, and higher mass stars are not well-sampled. As the most massive stars have a low occurrence rate, it is difficult to discern the maximum cutoff mass, above which stars do not contribute to the enrichment of metal-poor DLAs. In the case of a Salpeter IMF, the maximum likelihood estimate of M_{max} shifts to a larger value ($\approx 40\ \text{M}_\odot$) and the overall distribution becomes broader.

Regardless of whether we impose a prior on the slope parameter, the maximum likelihood estimate of the upper mass limit is $< 40\ \text{M}_\odot$. This limit was also reported by Ishigaki et al. (2018) who investigated the chemical enrichment of metal-poor halo stars. Our results tentatively support the work of Sukhbold et al. (2016) (see also, Burrows et al. 2019). These authors found that, when an explosion model is powered by neutrinos, only a fraction of the stars above 20 $\text{M}_\odot$ have sufficient energy to successfully launch a SN explosion. The remaining stars are presumed to collapse directly to black holes. Recent work by Sukhbold & Adams (2019) suggests that the apparent mass dependence of a progenitor's 'explodability' may be the consequence of a transition in the dominant carbon burning regime that occurs within the presupernova cores of progenitors at $\sim 20\ \text{M}_\odot$. This scenario is supported observationally by Adams et al. (2017), who have identified a potential failed SN in the form of a star that disappeared from multi-epoch LBT imaging; a technique

envisioned by Kochanek et al. (2008) and later implemented by Gerke et al. (2015) and Reynolds et al. (2015). We note that this result is also consistent with Heger et al. (2003), which reports the direct collapse of metal-free stars above 40 $M_\odot$.

2.4.4 Explosion energy

The maximum likelihood estimate of the typical explosion energy is $\hat{E}_{\rm exp} = 1.8^{+0.3}_{-0.2} \times 10^{51}$ erg. Under the assumption of a Salpeter IMF, $\hat{E}_{\rm exp} \approx 2 \times 10^{51}$ erg, which is consistent with the results of our fiducial model within the bootstrapped error bounds. The distribution of this parameter is the most well-defined, with an interquartile range spanning $(1.7 - 2.1) \times 10^{51}$ erg.

Our inferred enrichment model indicates that it is the lowest mass progenitors that are responsible for the enrichment of the DLAs in our sample. For these stars, simulations predict $< 10^{51}$ erg explosions (e.g. Müller et al. 2019). The high [Fe/O] yields associated with the high energy explosions of the lowest mass progenitors from HW10 may therefore be unrepresentative of a realistic scenario. It is these high [Fe/O] yields of the lowest mass progenitors that drive our analysis to disfavour models with high typical explosion energies (see the red contours in Figure 2.3 for an example of how an increase in the explosion energy impacts the expected range of observed abundances). We find it encouraging that our analysis shows no evidence for the models disfavoured by these simulations. As mentioned in Section 2.2.3, a potential future avenue of investigation is the consideration of a mass dependent explosion energy model; this may help accommodate the behaviour seen in recent simulations (Müller et al., 2019).

In HW10, the authors found that the abundance patterns of EMP halo stars (i.e. the Cayrel et al. 2004 sample) are best described by enrichment from SNe, typically with $0.6 \lesssim E_{\rm exp}/10^{51}$ erg $\lesssim 1.2$. In contrast to this, a similar analysis performed by Grimmett et al. (2018) found that the abundance patterns of EMP halo stars are best described by the yields of $(5 - 10) \times 10^{51}$ erg explosions (i.e hypernovae). This preference towards enrichment by a population of high energy SNe was also reported by Cooke et al. (2017) and Ishigaki et al. (2018). Furthermore, the observed overabundance of [Zn/Fe] in the

most metal-poor halo stars (Primas et al., 2000; Cayrel et al., 2004), is thought to be due to enrichment by a population of hypernovae (Umeda & Nomoto, 2002). Although the explosion energy that we derive in this work is somewhat lower than that found in other studies, our DLA sample probes a somewhat higher metallicity regime, $-3.0 \lesssim [\mathrm{O/H}] \lesssim -2.0$, where metal-poor stars exhibit solar relative abundances of [Zn/Fe]. The metal-poor DLAs in our sample may therefore be displaying the signature of enrichment from massive Population II stars that ended their lives with more moderate energy SN explosions.

2.5 Discussion

In the previous section, we investigated the properties of a metal-free stellar population that can describe the chemical abundance patterns of the metal-poor DLA population. The results of our fiducial model analysis suggest that the DLA abundances are well-described by enriching stars drawn from a Salpeter-like IMF at $M > 10$ M$_\odot$. These results also suggest that a typical metal-poor DLA has been enriched by $\lesssim 72$ massive stars (95 per cent confidence) and that these gas clouds have not been significantly enriched by stars with masses $\gtrsim 40$ M$_\odot$. The ability to recover a constraint on the IMF slope through the analysis of 11 systems is an encouraging sign that this model is a powerful tool. We find that the potential of this analysis is maximised when we demand that a given enrichment model is able to simultaneously reproduce all of the abundance ratios observed within a system.

In this section, we discuss the impact of alternative enrichment sources and the sensitivity of our results to the choice of chemical yields. We also highlight some of the inferences that can be made about metal-poor DLAs given an appropriate enrichment model.

2.5.1 Alternative enrichment sources

As mentioned in Section 2.3, we restrict our analysis to systems found beyond a redshift of $z = 2.6$ to minimise the potential for enrichment from non-Pop III stars (Welsh et al. 2019, in prep.). However, given that second generation stars are expected to have formed before this epoch, we must consider avenues through which metal-enriched stars can wash out the signature of Population III stars in the most metal-poor DLAs. Possible mechanisms include:

(i) Mass loss from Asymptotic Giant Branch (AGB) stars,

(ii) Type Ia SNe ejecta, and

(iii) Population II core-collapse (Type II) SNe ejecta.

We now discuss each of these possible enrichment avenues in turn.

2.5.1.1 AGB stars

Intermediate mass ($1 - 6$ M$_\odot$) Population II stars are capable of producing a significant quantity of carbon during their AGB phase (Karakas, 2014; Höfner & Olofsson, 2018). In what follows, we use the model parameter distributions of our fiducial model (with a prior $\alpha = 2.35$; green histograms in Figure 2.4) to estimate the number of AGB stars that may have contributed to the enrichment of the metal-poor DLAs in our sample. Using a similar approach to that adopted in Section 2.2, we then perform Monte Carlo simulations to sample stars within the AGB mass range. The carbon lost by these stars is determined using the AGB yield calculations performed by Karakas & Lattanzio (2007) and updated in Karakas (2010). Comparing the distribution of carbon expected from AGB stars to that expected from massive metal-free stars, we find that AGB stars can match ($\approx$ 110 per cent) the carbon yield from massive stars. The yields of all other elements considered in our analysis are negligible. For this estimate, we only consider the contribution from stars with masses $M > 2$ M$_\odot$ since lower mass stars have lifetimes in excess of 2 Gyr; given that

Population II stars likely formed at $z < 10$, stars with $M \lesssim 2\ \mathrm{M}_{\odot}$ will still be on the main sequence when most of the DLAs in our sample are observed (typically $z \sim 3$). Note, the contribution of carbon from Population II AGB stars would be even less if these stars were born more recently than $z \simeq 10$. To estimate how the presence of AGB stars could impact our inferences, we have repeated our analysis under the assumption that half of the carbon in a given system can be attributed to AGB stars. We find a preference towards both higher typical explosion energies and a flatter IMF slope; $N_{\star}$ and M_{max} are almost unchanged. However, a more sophisticated prescription is necessary to fully explore this scenario.

2.5.1.2 Type Ia SNe

Type Ia SNe are another potential source of metals in the most metal-poor DLAs. For many decades, it has been appreciated that the combination of [α/Fe] and [Fe/H] can indicate when a system has been chemically enriched by SNe Ia (see the discussion by Tinsley 1979 and Wheeler et al. 1989). Type Ia SNe occur after long-lived, low mass stars have become white dwarfs, therefore there is a delay in the onset of chemical enrichment from these SNe compared to that of Type II core-collapse SNe. The yields of Type Ia SNe are rich in Fe-peak elements, while those of Type II SNe are rich in both α-capture and Fe-peak elements. The short lifespans of massive stars mean that an environment is first enriched with the products of Type II core-collapse SNe. This produces an IMF-weighted abundance ratio of [α/Fe]. As the system evolves, the pool of high mass progenitors is quickly exhausted, and the [α/Fe] ratio plateaus until the onset of enrichment by Type Ia SNe. The Fe-rich ejecta of these SNe cause a decline in [α/Fe], known as the 'metallicity-knee' (or 'α-knee'). This can be observed by measuring the abundances of stars over a range of metallicities in a galaxy (Matteucci & Brocato, 1990; Matteucci, 2003). In the Milky Way, the knee occurs at [Fe/H] ≈ -1, while for some dwarf spherodial galaxies (dSphs), the knee has been identified at lower metallicities (Tolstoy et al., 2009). Sculptor and Fornax, two dSphs, show a decline in [α/Fe] at [Fe/H] ≈ -1.8 and [Fe/H] ≈ -1.9, respectively (Starkenburg et al., 2013; Hendricks et al., 2014; Hill et al., 2018). A similarly positioned knee has been observed across the DLA population by Cooke et al. (2015). They find that [α/Fe]

begins to fall when [Fe/H] $\gtrsim -2.0$. For the systems used in our analysis [Fe/H] < -2.0 (see Table 2.1); this places our DLA sample in the plateau of [α/Fe] and suggests that they have likely not yet been significantly contaminated by Type Ia SNe ejecta.

2.5.1.3 Population II core-collapse SNe

The ejecta of metal-enriched (i.e. Population II) core-collapse SNe are also a potential source of C, O, Si, and Fe, which may pollute the metal-free (Population III) signature in metal-poor DLAs. As Figure 2.1 highlights, at the explosion energies recovered by our fiducial model analysis, the relative yields of the most abundant elements are almost independent of the metallicity of the progenitor star. It is therefore difficult to uniquely delineate Population II versus Population III stars using only the most abundant chemical elements. However, it is nevertheless possible to search for several key chemical signatures in the metal-poor DLA population that might tease out the enrichment by Population III stars, including: (1) a very low value of $N_\star$ (e.g. $\sim\ 1-5$) might indicate that only a few massive stars contributed to the enrichment of the metal-poor DLA population; (2) if the first stars formed from an IMF with a slope parameter, α, that is different from Salpeter, we might expect to uncover an evolution of the slope parameter at the lowest metallicities; (3) we could measure the relative chemical abundances of elements near the Fe-peak (e.g. [Zn/Fe]; Primas et al. 2000; Umeda & Nomoto 2002; Cayrel et al. 2004), which may provide a more sensitive diagnostic of enrichment by metal-free stars. This may become possible with the next generation of 30 m class telescopes. At present, given that we only have access to the most abundant metals, we cannot uniquely distinguish between the yields of metal-free and slightly metal-enriched massive stars. Note that this prediction of a low $N_\star$ may be negated if the metal-poor DLAs contain the chemical products of multiple minihalos. However, given the relatively large value of $N_\star$ recovered by our fiducial model analysis, in addition to an IMF slope parameter that is consistent with investigations of current star formation, it appears likely that some of the metal-poor DLAs in our sample have been enriched by Population II stars.

2.5.2 Impact of yield choice

In this subsection, we consider the impact of our model yield choice. To this end, we have explored several different yield sets to determine the sensitivity of our model parameter inferences to the yields. First, we repeat our analysis considering the SNe yields of massive metal-enriched stars. Specifically, we consider progenitors whose metallicity is 10^{-4} $Z_{\odot}$, using the WW95 yield calculations. An inspection of the expected abundance ratios under the assumption of the WW95 yields, indicates that these yields are less able to reproduce the observed data compared to our fiducial yield choice. We come to the same conclusion when considering the yields of metal-free stars as calculated by LC12 (see Appendix A.1 for a detailed comparison). We note that the WW95 and the LC12 yields are not calculated across a grid of fixed explosion energies. Across the range of progenitor masses, the final kinetic energy of the SN ejecta varies, but is typically $\sim 10^{51}$ erg for both yield sets. To test how this limitation impacts our results, we have repeated our analysis using the HW10 yields, after imposing a strong prior on the SN explosion energy. We found that the model parameter estimates varied significantly between a moderate (1.2×10^{51} erg) explosion and that of a high energy (5×10^{51} erg) explosion. Thus being able to include the explosion energy as a free parameter allows the model to find a better fit to the available data.

A factor which impacts the yields of these calculations is the adopted rates of both the 3α reaction (which creates ^{12}C) and the $^{12}C(\alpha,\gamma)^{16}O$ reaction (which destroys ^{12}C). Adopting different determinations of these reaction rates can influence whether ^{12}C or ^{16}O is the dominant product of helium burning and, in turn, impact the yields of all elements (Weaver & Woosley, 1993). Currently, these reaction rates have an associated uncertainty of $\sim$ 10 per cent (West et al., 2013). HW10 adopt a $^{12}C(\alpha,\gamma)^{16}O$ reaction rate comparable to the most recent determination by An et al. (2016) who recommend a reaction rate[5] of $(7.83 \pm 0.35) \times 10^{15}$ cm^{3}mol^{-1}s^{-1} at T = 9×10^8 K, the temperature at which stellar helium burning occurs. Therefore, given the accuracy of the reaction rate adopted by HW10, in combination with the fine mass resolution and explosion energy

[5]This value corresponds to $S_{\rm tot}(300\,{\rm keV}) = (167.2 \pm 7.3)$ keV b. This value agrees fortuitously well with the rates adopted by HW10 (175 keV b), WW95 (170 keV b), and LC12 (165 keV b).

grids, and the fact that the HW10 models more accurately reproduce the available data (see Appendix A.1), we consider the HW10 yields to be the superior choice for our analysis.

2.5.3 Inferred properties of DLAs

Given the fiducial results of our enrichment model analysis, we now investigate some of the typical physical properties of the DLAs in our sample. These systems are only seen in absorption. Directly determining their total stellar content would be challenging, and we have no direct means to observationally investigate their total gas content. However, our analysis provides an indication of the enriching stellar population, which can be used to extrapolate an estimate of the total stellar mass and gas mass[6].

In what follows, we use the parameter distributions of our enrichment model analysis to describe the IMF of the enriching population, $\xi(M)$. The total stellar mass of a typical system can then be inferred using the equation:

$$M_{\star} = \int_{M_{\rm min}}^{M_{\rm max}} \xi(M) M \mathrm{d}M \ , \tag{2.5.1}$$

where $\xi(M)$ represents the IMF of the system. Note that our enrichment model is only sensitive to the yields of stars > 10 M$_{\odot}$. Therefore, if we assume that low mass stars have also formed in very metal-poor DLAs (as would be expected if these gas clouds have been enriched by Population II stars), these stars will constitute a significant fraction of the total stellar mass. For this inference, we must consider an IMF that is best able to account for the contribution of both low mass and high mass stars. In what follows, we adopt a Chabrier (2003) IMF, such that stars below 1 M$_{\odot}$ are modelled by a log-normal distribution. Given a bottom-heavy IMF, stars more massive than 100 M$_{\odot}$ provide a negligible contribution to the total stellar mass of a system, therefore we adopt an upper mass limit of $M_{\rm max} = 100$M$_{\odot}$. The left panel of Figure 2.5 shows the total stellar mass inferred for a typical metal-poor

[6]Recall, at the explosion energies recovered by our fiducial model analysis, the relative yields of both [C/O] and [Si/O], for a given progenitor mass, appear to be almost indistinguishable between Population II and Population III stars (see Figure 2.1). Therefore, in the following calculations we consider the HW10 yields to be an appropriate estimator of both Population II and Population III core-collapse SNe yields.

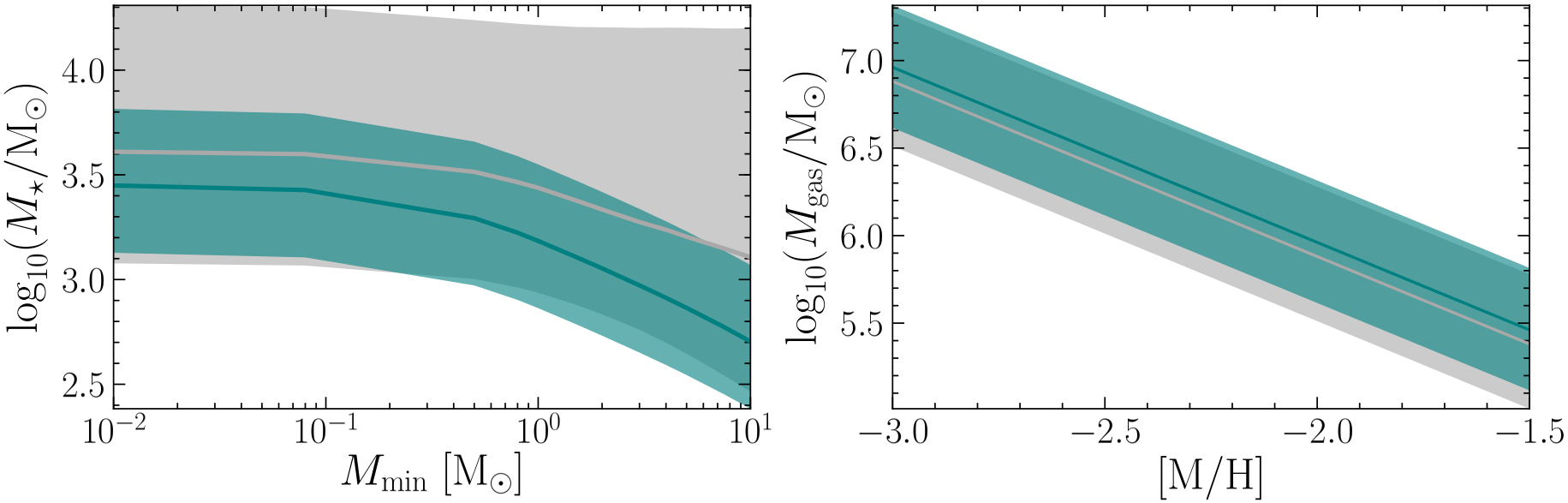

Figure 2.5. Inferred physical properties of metal-poor DLAs, based on the likelihood distributions of our model parameters. The grey distribution shows the expected stellar content when the model IMF slope is allowed to vary. The green distribution is the resulting stellar content under the assumption of a Salpeter IMF slope. The solid lines indicate the median value and the shaded region encompasses the 16^{th} and 84^{th} percentiles. The left panel shows the total stellar mass within a given system as a function of the minimum mass with which stars can form. In this case we have adopted a Chabrier (2003) IMF and assumed that both low- and high-mass stars have contributed to the total stellar content. The right panel shows the total gas mass expected within these systems as a function of their metal content. The metal content [M/H] has been inferred from that of [O/H], which is a common proxy. Note that for a given position in our model parameter space, there are a range of possible ejected metal masses. In this scenario we assume that the most probable value is representative. We also assume 100 per cent retention of the metals. If some metals were not retained, this would lead us to overestimate the gas mass.

DLA as a function of the minimum mass with which stars can form. We show the inferred stellar mass from both our fiducial model analysis and the case of a Salpeter IMF slope at high masses. From this we see that, for the case of a Salpeter IMF slope, if the stars within very metal-poor DLAs can form down to 0.1 $M_\odot$, then the total stellar mass formed over the lifetime of the system is $\log_{10}(M_\star) = 3.5^{+0.3}_{-0.4}$ $M_\odot$. This value is comparable to the stellar content of the faint Milky Way satellite population (Martin et al., 2008; McConnachie, 2012), which typically span a mass range of $\sim (10^2 - 10^5)$ $M_\odot$, and are still expected to contain gas at redshift $z \sim 3$ (Oñorbe et al., 2015; Wheeler et al., 2018). We suggest that, given a more robustly determined enrichment model, our inference could allow us to draw parallels between the metal-poor DLA population and their potential galactic descendants. A precise inference of the stellar mass content could also help discern whether the most metal-poor DLAs are the progenitors of some Ultra Faint Dwarf (UFD) galaxies.

We can also use the results of our analysis to infer the typical total gas mass of metal-poor DLAs. Given an enrichment model, we can determine the mass of metals that have been introduced, to a previously pristine environment, through SNe ejecta. In the same way that we construct the distribution of [C/O] for a given enrichment model (described in Section 2.2), we can also construct a distribution of the ejected metal mass. For simplicity, we take the most probable value of this distribution to be representative. Thus, by sampling the parameter distributions shown in Figure 2.4 and calculating the associated ejected metal mass, we can build a distribution of the typical metal mass expected within our systems. We can then infer the typical mass of gas that has been mixed with the metals of core-collapse SNe, as a function of the measured [O/H] metallicity of the gas. For a given [O/H] abundance and ejected oxygen mass, Equation 2.2.1 can be used to determine the expected mass of hydrogen that has been mixed with the metals of the Type II core-collapse SNe yields. As metals contribute a negligible amount to the overall system mass, the total gas mass is given by the sum of the contribution from both hydrogen and helium. We assume that the helium mass fraction is equal to the primordial value ($Y_P \simeq 0.247$; Pitrou et al. 2018). The right panel of Figure 2.5 shows the total gas mass of a typical system as a function of the system's metal abundance. For an extremely metal-deficient system

i.e. [M/H] ~ -3.0, the total gas mass, under the assumption of a Salpeter IMF slope for high mass stars, is $\log_{10}(M_{\rm gas}/\,{\rm M}_{\odot}) = 7.0^{+0.3}_{-0.4}$. This suggests that stars may constitute just $\approx$ 0.03 per cent of the mass fraction of the most metal-deficient DLAs. As a point of comparison, Cooke et al. 2015 found that the mass of warm neutral gas within a typical metal-poor DLA is $\log_{10}(M_{\rm WNM}/\,{\rm M}_{\odot}) = 5.4^{+1.9}_{-0.9}$. This was calculated using a sample of DLAs with a typical [O/H] abundance of [O/H] ≈ -2.0. Our calculation of the total gas mass within systems of this metallicity suggests that warm neutral gas may constitute $\approx$ 30 per cent of the total gas mass.

2.6 Conclusions

We present a novel, stochastic chemical enrichment model to investigate Population III enriched metal-poor DLAs using their relative metal abundances; this model considers the mass distribution of the enriching stellar population, the typical explosion energy of their SNe, and the average number of enriching stars. We use this model to investigate the chemical enrichment of the 11 most metal-poor DLAs at $z \geq 2.6$. We conduct a maximum likelihood analysis of the enrichment model parameters, given relative abundances ([C/O], [Si/O] and [Fe/O]) of this sample of metal-poor DLAs. Our main conclusions are as follows:

(i) The mass distribution of the stars that have enriched the sample of metal-poor DLAs can be well-described by a Salpeter-like IMF slope.

(ii) The average system has been enriched by $\lesssim 72$ massive stars (95 per cent confidence), with a maximum likelihood value of $\hat{N}_{\star} = 10 \pm 4$, suggesting that the most metal-poor DLAs are minimally enriched.

(iii) Our maximum likelihood estimate of the upper mass limit of enriching stars suggests that the most metal-poor DLAs have been predominantly enriched by stars with masses $\lesssim 40$ M$_{\odot}$. This provides tentative evidence in support of the suggestion that

some stars above 20 $M_\odot$ fail to explode, and instead collapse directly to black holes (Sukhbold et al., 2016).

(iv) Our model suggests that the stars that enriched the most metal-poor DLAs had a typical explosion energy $E_{\rm exp} = 1.8^{+0.3}_{-0.2} \times 10^{51}$ erg, which is somewhat lower than that found by recent works that model the enrichment of metal-poor halo stars (Ishigaki et al., 2018; Grimmett et al., 2018).

(v) Using the results of our likelihood analysis, we infer some of the typical physical properties of metal-poor DLAs. We find that the total stellar mass content of metal-poor DLAs is $\log_{10}(M_\star/{\rm M}_\odot) = 3.5^{+0.3}_{-0.4}$, assuming a Chabrier (2003) IMF. We note that this value is comparable to the stellar mass content of faint Milky Way satellites (Martin et al., 2008; McConnachie, 2012) and suggest that, in the future, this inference might allow us to test if some of the most metal-poor DLAs are the antecedents of the UFD galaxy population.

(vi) We also infer the total gas mass of typical metal-poor DLAs as a function of their measured [O/H] metallicity: $\log_{10}(M_{\rm gas}/\,{\rm M}_\odot) = 7.0^{+0.3}_{-0.4}$ for DLAs with [O/H] ≈ -3.0. Comparing this value to the mass of warm neutral gas in metal-poor DLAs $\left(\log_{10}(M_{\rm WNM}/\,{\rm M}_\odot) = 5.4^{+1.9}_{-0.9}\right.$; Cooke et al. 2015$\left.\right)$, we find that ≈ 30 per cent of the gas in a DLA with [O/H] ≈ -2.0 may be in the warm neutral phase.

Finally, we realise the potential for future improvement if we can minimise the potential for contamination from later generations of star formation. Once there is a larger sample of EMP DLAs, we will be able to restrict our analysis to systems with [O/H]≤ -3.0. Alternatively, in the future, we will include in our enrichment model the potential contribution of metals from Population II stars (i.e. by considering the mass loss from intermediate mass AGB stars).

We conclude by suggesting that our stochastic enrichment model, combined with the HW10 nucleosynthetic yields, is a powerful tool to learn about the earliest episodes of star formation. We expect that future applications of this analysis will reveal a distinctive Population III signature and the opportunity to learn about the mass distribution of the first

stars; to this end, we will use our model to explore the enrichment of the most metal-poor stars found in the halo of the Milky Way. Through these systems, we hope to gauge the multiplicity of the first generation of stars.

CHAPTER 3

The stochastic enrichment of Population II stars

The following chapter is reprinted from the publication "The stochastic enrichment of Population II stars" (Welsh et al., 2021). While the previous chapter focused on the enrichment of the metal-poor DLA population, this chapter focuses on the enrichment of the metal-poor stellar population. By design, the metallicity range of this stellar sample is comparable to the DLA sample analysed in the previous chapter. We can therefore compare the chemical enrichment of these relic environments. Given the results of the previous chapter, our analysis suggests that the most metal-poor DLAs have been enriched by < 13 (2σ) Population III minihalos. This analysis can help us trace the dispersion of metals from these initial minihalos to the first galaxies, and the metal-poor DLAs to their local descendants. In this analysis, we also address the sensitivity of our model to both the input data and the adopted nucleosynthetic yields. To take full advantage of this model, we require input data whose systematic errors are well understood and nucleosynthetic yield calculations with known errors.

Abstract: We investigate the intrinsic scatter in the chemical abundances of a sample of metal-poor ([Fe/H] < -2.5) Milky Way halo stars. We draw our sample from four historic surveys and focus our attention on the stellar Mg, Ca, Ni, and Fe abundances. Using these elements, we investigate the chemical enrichment of these metal-poor stars using a model of stochastic chemical enrichment. Assuming that these stars have been enriched by the first generation of massive metal-free stars, we consider the mass distribution of the enriching population alongside the stellar mixing and explosion energy of their supernovae. For our choice of stellar yields, our model suggests that the most metal-poor stars were enriched, on average, by $\hat{N}_\star = 5^{+13}_{-3}$ (1σ) Population III stars. This is comparable to the number of enriching stars inferred for the most metal-poor DLAs. Our analysis therefore suggests that some of the lowest mass structures at $z \sim 3$ contain the chemical products from < 13 (2σ) Population III enriched minihaloes. The inferred IMF is consistent with that of a Salpeter distribution and there is a preference towards ejecta from minimally mixed hypernovae. However, the estimated enrichment model is sensitive to small changes in the stellar sample. An offset of ~ 0.1 dex in the [Mg/Ca] abundance is shown to be sensitive to the inferred number of enriching stars. We suggest that this method has the potential to constrain the multiplicity of the first generation of stars, but this will require: (1) a stellar sample whose systematic errors are well understood; and, (2) documented uncertainties associated with nucleosynthetic yields.

3.1 Introduction

Before the cosmic dawn, essentially all baryons were comprised of hydrogen and helium. The stellar population born from the collapse of this primordial gas transformed their environment irrevocably through the fusion of the first metals (i.e. elements heavier than lithium). As one of the first sources of radiation, these Population III (Pop III) stars were early contributors to the reionisation of the Universe, and, the feedback from these stars influenced the size of the first galaxies (Barkana & Loeb, 2001; Bromm & Yoshida, 2011). This stellar population is also encoded with vital information such as the size and number

abundance of the first star-forming structures in the Universe (i.e. the early dark matter minihaloes) (Abel et al., 2002; Bromm et al., 2002, 2003; Greif et al., 2011; Naoz et al., 2012). Studying this stellar population can therefore shed light on parts of the Universe's history that are currently shrouded in mystery.

In principle, these Population III stars are straight-forward to identify. They are the only stellar population whose atmospheres are expected to be entirely metal-free (at least initially). However, the search for these stars has spanned almost 4 decades and, as of yet, none have been found (Bond, 1980; Beers et al., 1985, 1992; Keller et al., 2007; Christlieb et al., 2008; Aoki et al., 2013; Caffau et al., 2013; Li et al., 2015; Aguado et al., 2016; Howes et al., 2016; Starkenburg et al., 2017; Da Costa et al., 2019). While the first stars have eluded detection, these ongoing surveys have found an ever increasing number of stars that are increasingly deficient in iron. The surviving extremely metal-poor (EMP) stars, whose iron abundances are less than 1/1000 the solar value (i.e. [Fe/H] < -3), are referred to as stellar relics[1]. Their surface abundances are thought to be a window to the chemical composition of the gas from which they formed. Studying the chemistry of these stars may therefore reveal the properties of the stellar population that preceded them. This approach, termed 'stellar archaeology', has become one of the leading observational probes of Population III properties in recent years (Frebel, 2010).

A key property, yet to be uncovered, is the underlying mass distribution of Population III stars. Current simulations suggest that, as these stars formed in the absence of metals, their typical mass range spanned $\sim 10 - 100$ $M_\odot$ (Clark et al., 2008; Stacy et al., 2010; Clark et al., 2011; Greif et al., 2012; Stacy et al., 2016). The Population III initial mass function (IMF) is therefore thought to be distinct from that of later stellar populations. The majority of stars in this expected mass range enrich their environment through core-collapse supernovae (CCSNe). Searches for a Population III signature therefore rely on simulations of stellar evolution, like those of Woosley & Weaver (1995); Umeda & Nomoto (2002, 2003); Chieffi & Limongi (2004); Umeda & Nomoto (2005); Tominaga et al. (2007);

[1]Here, and throughout this paper, [X/Y] denotes the logarithmic number abundance ratio of elements X and Y relative to their solar values $X_\odot$ and $Y_\odot$, i.e. $[X/Y] = \log_{10}\left(N_X/N_Y\right) - \log_{10}\left(N_X/N_Y\right)_\odot$.

Heger & Woosley (2010); Limongi & Chieffi (2012), to compare the chemical abundances expected from Population III CCSNe to those observed in the atmospheres of surviving Population II stars.

Carbon-enhanced ([C/Fe] > +0.7) EMP stars that show 'normal' relative abundances of neutron-capture elements (i.e. CEMP-no stars) are considered to be the most likely descendants of the first stars (Beers & Christlieb, 2005; Frebel & Norris, 2015). It has been suggested that the CEMP-no stars in the metallicity regime $-5 <$ [Fe/H] < -4 are the most promising probes of Population III properties (Placco et al., 2016). However, only 11 stars are currently known to meet this criteria[2]. It is also unclear what fraction of Population II stars are likely to present as CEMP-no stars in the local Universe (Ji et al., 2015; Hartwig & Yoshida, 2019). Thus, searches for a Population III chemical signature generally include EMP stars alongside CEMP-no stars.

Cosmological hydrodynamic simulations have suggested that Population III stars likely formed either individually or in small multiples (Greif et al., 2010; Stacy et al., 2010; Susa et al., 2014). However, traditional comparisons between the observed stellar abundances and the simulated yields have been restricted to two scenarios, either: (1) one progenitor is responsible for the enrichment of a surviving star (e.g. Frebel et al. 2015; Ishigaki et al. 2018; Nordlander et al. 2019; Ezzeddine et al. 2019); or (2) the observed abundances can be modelled by the IMF weighted yields from these simulations (e.g. Heger & Woosley 2010). Though, the use of semi-analytic models has enabled the consideration of multiple enriching progenitors (Karlsson, 2005; Karlsson & Gustafsson, 2005; Hartwig et al., 2018a).

In this paper, we use a novel approach to analyse the chemistry of the most metal-poor stars, and use this tool to infer the number of massive Population III stars that have enriched the surviving metal-poor stellar relics. Previously, we have applied this tool to investigate the enrichment of the *most* metal-poor damped Lyman-α systems (DLAs) (Welsh et al., 2019, 2020). We now extend this work to investigate the stochastic enrichment of a sample of

[2]As documented by the Stellar Abundances for Galactic Archaeology (SAGA) database — an invaluable tool for exploring and compiling stellar samples from existing surveys of metal-poor stars (Suda et al., 2008, 2011; Yamada et al., 2013; Suda et al., 2017).

Table 3.1. .
Summary of surveys that we consider in this work.

survey	programme size	sample size	N_{giants}	σ_{Mg}	σ_{Ca}	σ_{Ni}
C04	35	32	32	0.12	0.11	0.06
B09	19	18	0	0.06	0.11	0.07
Y13	38	12	6	0.11	0.12	0.15
R14	313	188	92	0.11	0.15	0.17

metal-poor Milky Way halo stars using their measured [Mg/Ca] and [Ni/Fe] abundances. While not the subject of this work, we note that the potential for inhomogeneous metal-mixing at the sites of Population II star formation is an additional complication that is an interesting avenue for further investigations (Salvadori et al., 2010; Sarmento et al., 2017; Hartwig et al., 2018b; Tarumi et al., 2020).

Our paper is organised as follows. Section 3.2 describes the observational sample used in this paper. Section 3.3 motivates the use of a stochastic enrichment model. In Section 3.4 we outline this model and apply it to the observational data. The results are discussed in Section 3.5 before drawing overall conclusions in Section 3.6.

3.2 Data

The stellar abundances considered in this work are a compilation of four sources. Specifically, that of: Cayrel et al. (2004; hereafter C04), Bonifacio et al. (2009; hereafter B09), Yong et al. (2013; hereafter Y13), and, Roederer et al. (2014; hereafter R14). C04 and B09 are part of the *First Stars* series. Note that we only consider the programme stars reported by Y13 (and not the literature stars used in their analysis). A summary of these data can be found in Table 3.1 where programme size indicates the number of stars reported in the original works, sample size indicates the number of objects used in our analysis, and σ_X indicates the median error associated with the reported [X/Fe] values. Across all samples there are 11 metals in common[3]. In our paper, we restrict our analysis to the Mg, Ca, Fe, and Ni relative abundances of these samples. The choice of elements is primarily

[3]These elements include: C, Mg, Si, Ca, Sc, Ti, Cr, Mn, Fe, Co, and Ni.

driven by the perceived confidence in both the observed abundances and the simulated yields. Furthermore, the abundances of these elements are amongst those most commonly reported throughout the chosen stellar samples. Additionally, they are sensitive to the properties (e.g. mass, metallicity, stellar mixing etc.) of the stars that synthesised these elements. Finally, as discussed in Section 3.4, our modelling technique is computationally expensive, so we are currently limited to selecting only a small number of the most reliable elements.

The abundances adopted in our work have been computed under the assumption of local thermodynamic equilibrium (LTE) using 1D model atmospheres. These models do not capture possible spatial inhomogenities. Mg, Ca, and Ni abundances are often determined from the spectral features of neutral species; these lines are generally thought to be more susceptible to non-LTE processes than those of ionised species (Asplund, 2005). We do not apply non-LTE corrections to these data, but the impact of this decision is discussed in Section 3.5.1. Similarly, Fe I lines are known to be affected by overionisation (Thévenin & Idiart, 1999). This can in-turn impact the estimated surface gravity of the star. These departures from LTE can be accounted for through comparisons of the Fe I and Fe II abundances. We note that this correction may be imperfect as Fe II lines may also form in regions that depart from LTE.

We apply a metallicity cut at [Fe/H] < -2.5. This ensures our sample of metal-poor halo stars is of comparable metallicity to the sample of DLAs analysed by Welsh et al. (2019). This criteria is more lax than the limit commonly imposed when investigating Population II chemical enrichment; these studies often reserve their analysis for EMP stars with [Fe/H] < -3. These stars are considerably less numerous and are often analysed individually; including these stars, from additional sources, would risk biasing our sample towards the *most* chemically peculiar stars currently known. As summarised in Table 3.1, we consider 32 stars from C04, 18 stars from B09, 12 stars from Y13, and 188 stars from R14. Figure 3.1 shows the abundances of these survey stars as a function of their [Fe/H] abundance. Note that to be included in our sample, a star must be sufficiently metal poor ([Fe/H] < -2.5) and have bounded [Mg/Fe], [Ca/Fe], and [Ni/Fe] abundances.

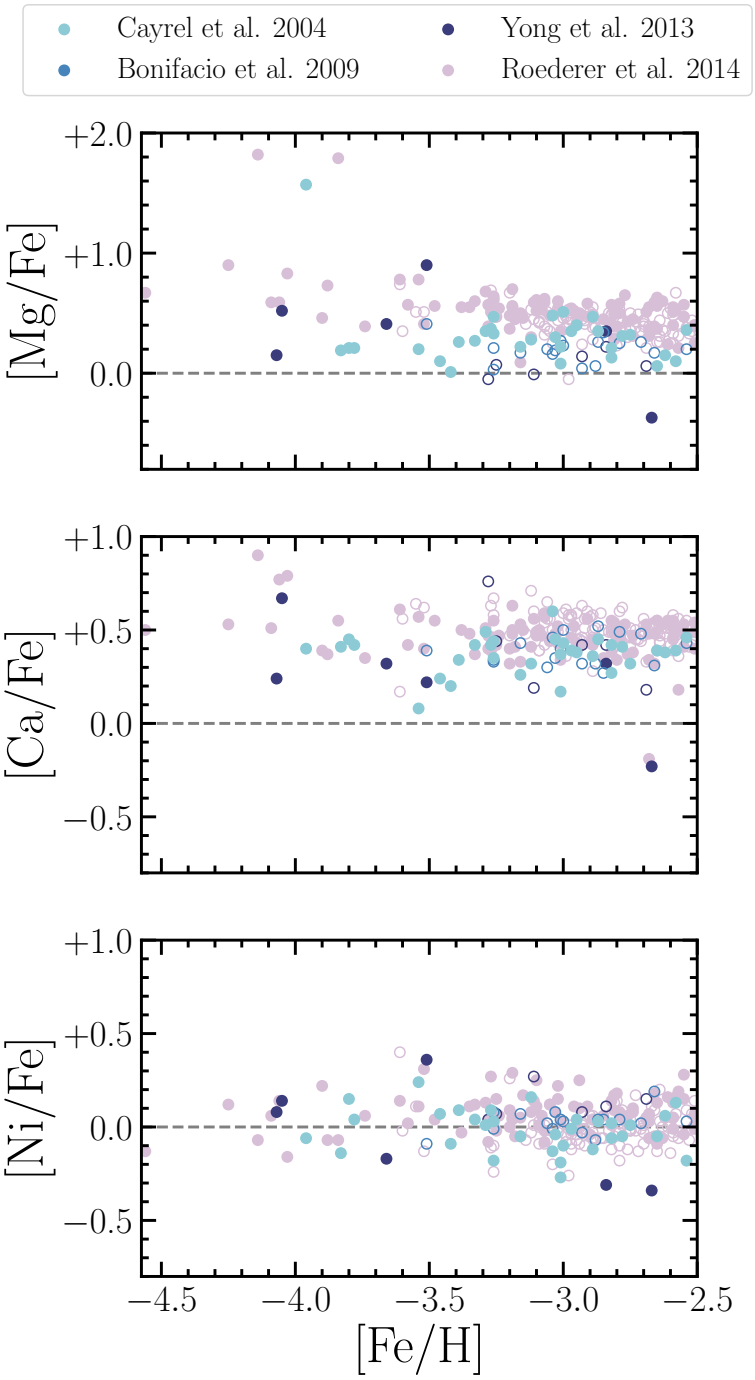

Figure 3.1. From top to bottom, the successive panels show the measured [Mg/Fe], [Ca/Fe], and [Ni/Fe] abundances of our stellar sample as a function of their [Fe/H] abundances. The colour of the marker indicates the source of the data (defined in the legend and used throughout this paper). The fill of the marker indicates the evolutionary stage of the star — giants are shown by filled circles while non-giants are shown by hollow circles. The horizontal dashed line indicates the solar value. Note the different y-axis scale used in the top panel.

Table 3.2. Solar abundances adopted in this analysis and those used in sample sources.

Element	This Work	C04	B09	Y13 / R14
Mg	7.56	7.58	7.58	7.60
Ca	6.29	6.36	6.36	6.34
Fe	7.47	7.50	7.51	7.50
Ni	6.21	6.25	6.25	6.22

This sample contains stars in various stages of their evolution. We make no initial distinction between the abundances of giants and non-giants — though, they can be distinguished in Figure 3.1 through the fill of the markers. Note that below [Fe/H] < -3.5, our sample almost exclusively contains giant stars (which are known to be more susceptible than dwarfs to non-LTE processes).

The adopted metallicities, [Fe/H], are determined solely from Fe I abundances. The relative abundance ratio between any two elements is determined by considering the abundances of species in the same ionisation state. In these works, Mg is determined using the spectral features of neutral species, therefore [Mg/Fe] is given by [Mg I/Fe I], together with its associated error.[4] The solar values adopted in this paper are taken from Asplund et al. (2009) and are shown in Table 3.2 alongside those adopted by the original sources. Note that all of the measured relative abundances and chemical yields that are used in this work have been registered onto the same solar abundance scale (see second column of Table 3.2).

To investigate the properties of Population III stars using the chemical abundances of Population II stars, we require a homogeneous stellar sample whose photospheric abundances are not dominated by systematic effects. As highlighted in Figure 3.1, the R14 data is known to show an elevated [Mg/Fe] abundance relative to the other samples. The origin of this offset, as found by R14, is due to the way that the effective temperature $T_{\rm eff}$ is determined across the different samples. C04, B09, and Y13 utilise a combination of photometric and spectroscopic information to determine $T_{\rm eff}$. R14 primarily consider spectroscopic data in their determination of $T_{\rm eff}$. We find that this offset between the R14 data and the other samples can be minimised when considering the abundance ratios of elements close to one another in atomic number — in this case [Mg/Ca] and [Ni/Fe]. The generalised

[4]Note, in the case of C04, the errors of [X I/Fe I] are given by the errors reported for [X/Fe].

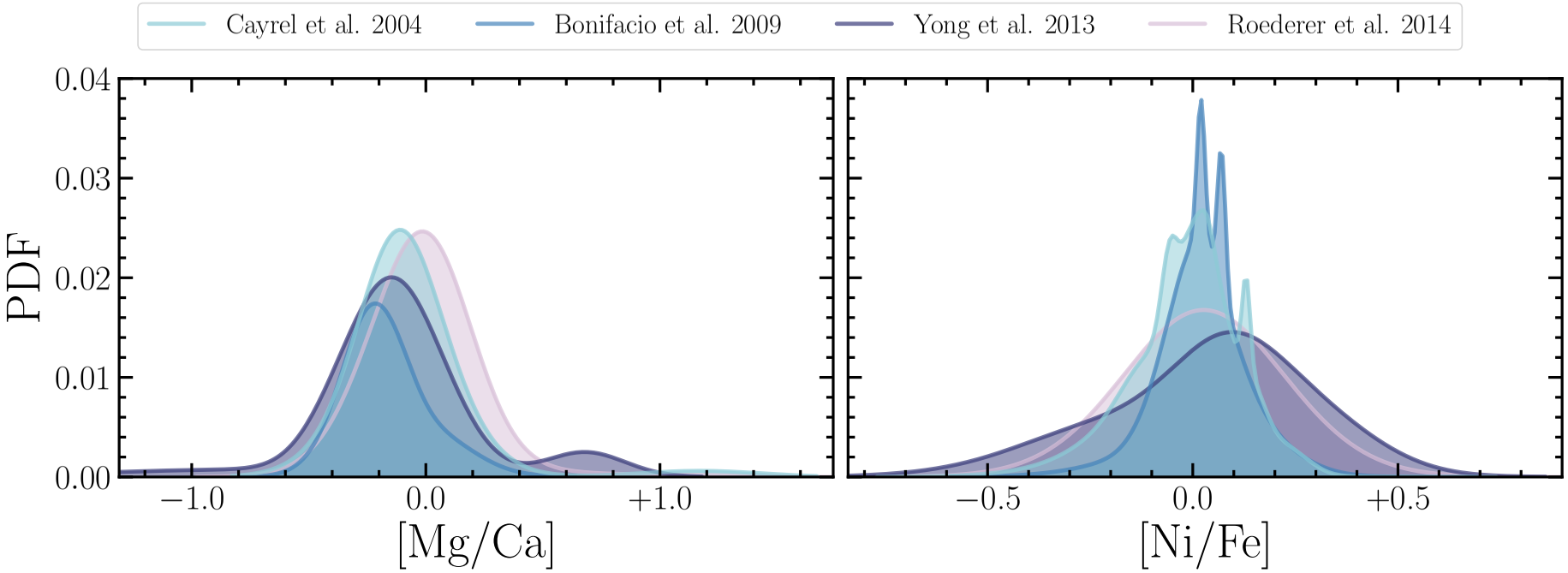

Figure 3.2. Generalised histograms showing the [Mg/Ca] (left) and [Ni/Fe] (right) abundance distributions of the individual samples. The colour indicates of the source of the data. The chemical abundance of each object has been treated as a Gaussian with a standard deviation given by the observational error. Considering the abundance ratios of elements close to one another in atomic number minimises the differences seen between the samples.

histograms of these abundance ratios for each sample are shown in Figure 3.2. When comparing the abundances of these stars to the yields of Population III SNe, we therefore draw parallels between the observed and simulated [Mg/Ca] and [Ni/Fe] abundances [5]. This allows us to consider the stars from all four surveys simultaneously and take advantage of the large dataset afforded by R14. We note that there are a number of stars that appear in multiple surveys. For these objects, we adopt the abundances derived from data with the superior spectral resolution. The numbers quoted in Table 3.1 represent the data after the removal of duplicates; there are 250 unique stars in this sample.

Finally, we note that the stars comprising the *First Stars* series (C04, B09) are thought to be kinematically associated with either the Gaia Sausage-Enceladus satellite or *in-situ* star formation (Di Matteo et al., 2020). In the context of our work, it is important that we focus on only the *most* metal-poor stars; at somewhat higher metallicity, the signature of Pop III stars will be increasingly washed out by the early star formation history of the dwarf galaxy where the Pop II star was born. Thus, provided our stellar sample are purely enriched by Pop III stars, the origin of the star is not critical to our analysis.

3.3 Intrinsic scatter

Before we model the chemical enrichment of these data in detail, we first motivate the importance of employing a stochastic chemical enrichment model given the present sample of stars. Treating each stellar survey independently, we have investigated if the reported abundances show significant *intrinsic* scatter that cannot be explained by the observational errors. To quantify this additional scatter, we model each abundance ratio as a Gaussian centred about $[X/Fe]_{cent}$ whose error is given by the expression:

$$\sigma_{tot}^2 = \sigma_{obs}^2 + \sigma_{int}^2 \,. \tag{3.3.1}$$

Thus, the dispersion of the data is given by the observed error σ_{obs} and an additional intrinsic component σ_{int} added in quadrature. We therefore consider two model parameters

[5]Note that the distributions shown in Figure 3.2 are almost identical for giants and non-giants.

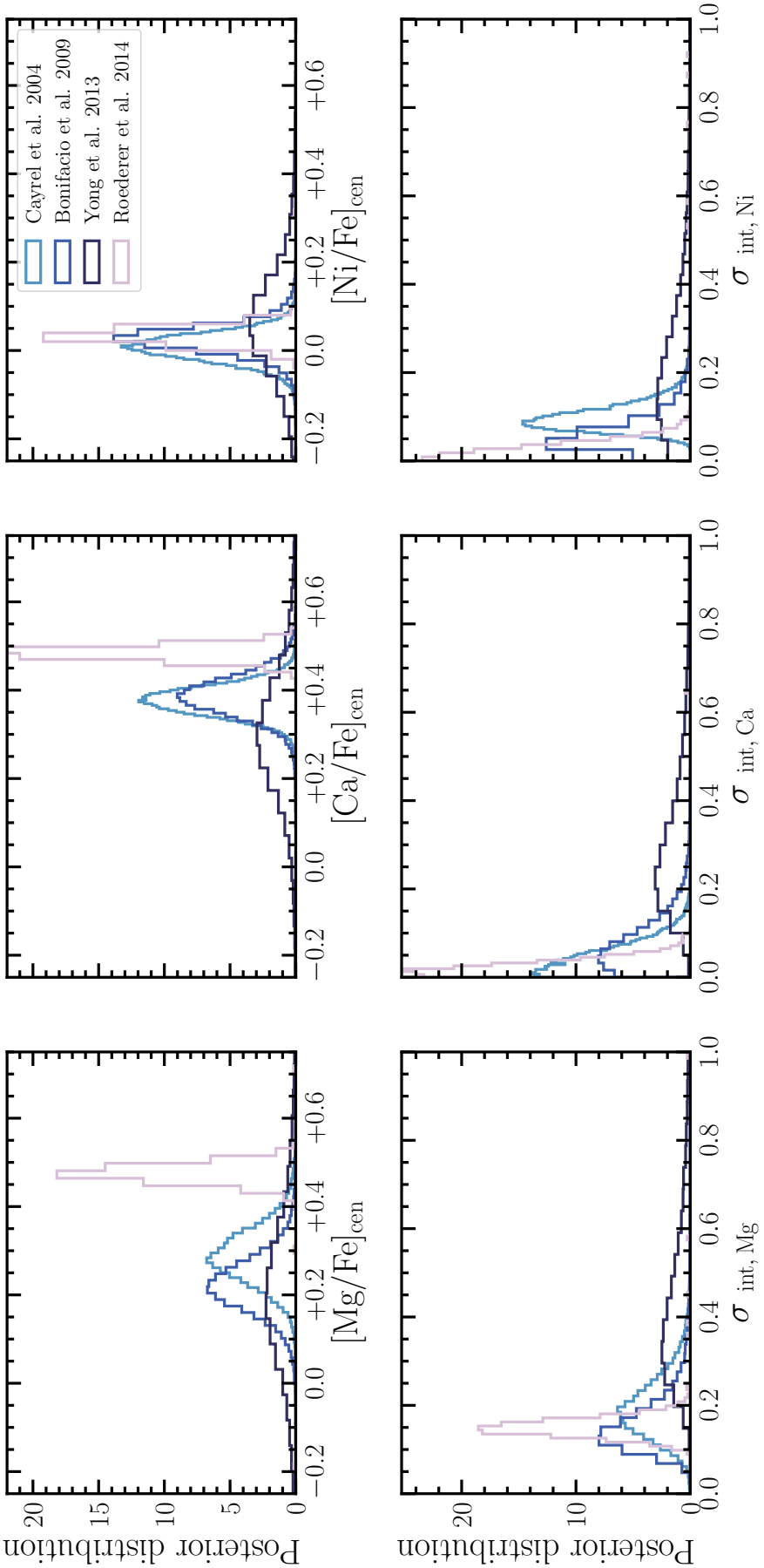

Figure 3.3. The top row shows the posterior distributions of the central [Mg/Fe] (left), [Ca/Fe] (centre), and [Ni/Fe] (right) abundance ratios estimated for each survey independently. The bottom row shows the posterior distributions of the intrinsic scatter associated with these central values. The colour of the histogram indicates the source of the data (as indicated in the legend).

([X/Fe]$_{\rm cent}$ and $\sigma_{\rm int}$) that we determine independently for each abundance ratio and each sample.

When looking at the [Mg/Fe], [Ca/Fe], and [Ni/Fe] abundances of the individual surveys, we have consistently found a non-zero intrinsic scatter associated with the [Mg/Fe] abundances of all the stellar samples. This intrinsic scatter is estimated using a Markov Chain Monte Carlo (MCMC) procedure that simultaneously estimates the central values [Mg/Fe]$_{\rm cent}$, [Ca/Fe]$_{\rm cent}$, and [Ni/Fe]$_{\rm cent}$ of a sample, alongside their associated additional error components $\sigma_{\rm int,Mg}$, $\sigma_{\rm int,Ca}$, and $\sigma_{\rm int,Ni}$. For details of this calculation and an example of the converged analysis of the C04 data, see Appendix B.1. Figure 3.3 shows the resulting posterior distributions of this analysis for all stellar samples used in this work. The bottom left panel of this figure shows the posterior distribution of the intrinsic scatter present in the [Mg/Fe] data. This intrinsic scatter implies that either: (1) there is a consistent intrinsic scatter associated with the [Mg/Fe] abundances of the stars in every sample; or (2) the [Mg/Fe] abundance errors are all consistently underestimated by ~ 0.15 dex. In this paper, we consider the first possibility, but note that there may also be some non-physical origin of this scatter. For example, the impact of assuming LTE may affect stars of a given metallicity, temperature, and/or surface gravity more significantly than others.

We have repeated this analysis after removing the peculiar stars with [Mg/Fe]$> +1$ (see the top panel of Figure 3.1). This modification affects both the C04 and R14 data. We find that the estimated intrinsic scatter is reduced across both samples; however, both the revised C04 and revised R14 samples independently support a statistically significant deviation (1.5σ) from zero intrinsic scatter. We have also investigated whether this scatter is dependent on the metallicity of the star. Focusing on the C04 sample, we found that the enhanced [Mg/Fe] abundance of CS 22949 – 037 is difficult to replicate alongside the other data. If it is removed from the sample, we find no strong dependence with metallicity. The result is mirrored when considering the R14 data. The B09 and Y13 samples are deemed too small to reliably capture any relationship between the intrinsic scatter and the metallicity of a star.

We emphasise that, irrespective of trends with metallicity, the intrinsic scatter in [Mg/Fe]

is non-negligible for each sample when treated independently. The scatter in this data may highlight the inhomogeneous nature of the environments within which these stars formed. To understand the chemical abundances of these objects it is therefore necessary to consider a stochastic chemical enrichment model.

3.4 Stochastic enrichment

Using a model of stochastic chemical enrichment in combination with the yields from simulations of stellar evolution, we can test if the observed chemical abundances of Population II stars are consistent with enrichment by Population III SNe. This model assumes that the number of Population III stars responsible for enriching a given environment is given by the integral:

$$N_\star = \int_{M_{\rm min}}^{M_{\rm max}} k M^{-\alpha} {\rm d}M \tag{3.4.1}$$

where M is the mass of the Population III star, α controls the slope of the power-law, and k is a multiplicative constant dependent on the number of stars forming within the mass range bounded by $M_{\rm min}$ and $M_{\rm max}$. In addition to the mass distribution of the enriching stars, we consider the typical explosion energy of the Population III SNe as well as the degree of mixing between the stellar layers. To determine the abundances expected from a given model, we rely on simulations of stellar evolution. Our fiducial choice of nucleosynthetic yields, described below, are those of Heger & Woosley (2010; hereafter HW10).

The HW10 simulations calculate the yields of massive Population III stars that end their lives as Type II SNe. This simulation suite reports a grid of chemical yields as a function of: (1) the progenitor star mass; (2) the mixing between the stellar layers during the explosion, and; (3) the kinetic energy of the SNe ejecta at infinity. These yields have been calculated using non-rotating, 1D models under the assumption of spherical symmetry. They do not account for mass loss or magnetic fields. The Rayleigh-Taylor instabilities that aide mixing between the stellar layers cannot be captured by 1D models. In these simulations mixing is achieved by moving a boxcar of width ΔM through the star, typically four times.

ΔM is described as a fraction of the He core size $f_{\rm He}$. The boxcar width that reproduces the hard X-ray and optical lightcurves of SN 1987A is 10 per cent of the He core size ($f_{\rm He} = 0.100$). The eventual collapse of the progenitor, and the subsequent SN explosion, is simulated by depositing momentum at the base of the oxygen burning shell. The strength of this explosion is parameterized by the kinetic energy of the ejecta at infinity. The typical explosion energy of a SN is $E_{\rm exp} = 1$ B (where 1 B = 10^{51} ergs). The HW10 yields have been calculated for 16,800 combinations of these three parameters (progenitor mass, stellar mixing, and explosion energy).

Figure 3.4 shows the yields of [Mg/Ca] and [Ni/Fe] as a function of progenitor star mass for a range of explosion energies. The left and right set of panels show the simulated yields for two mixing prescriptions. Those on the left adopt the value recommended by HW10 (10 per cent of the He core size). Those on the right indicate the yields of SNe that undergo minimal mixing between stellar layers (1 per cent of the He core size). From this figure it is clear that the yields of both [Mg/Ca] and [Ni/Fe] are highly variable for low values of the SNe explosion energy and/or the mixing width. There is a more consistent relationship with progenitor mass when $f_{\rm He} = 0.1$. In this case, there is a general trend of increasing [Mg/Ca] with increasing progenitor mass, while [Ni/Fe] shows no strong evolution across the considered mass range. The variability across the indicated parameter space highlights that small changes in the progenitor properties can have a distinct impact on the resulting yields; this is, in part, due to the nonlinear interactions that occur between the burning layers of the star. The minimal mixing during the explosive nuclear burning phase is a further aide to this variability, as can be seen through comparing the panels on the left and right of Figure 3.4.

3.4.1 Stochastic sampling

To determine how the simulated Population III yields compare to the observed abundances of stellar relics, it is necessary to consider how these objects may have been chemically enriched. In their respective minihaloes, the first stars are thought to form either individually or in small multiples. Thus, the surviving Population II stars may have been enriched by

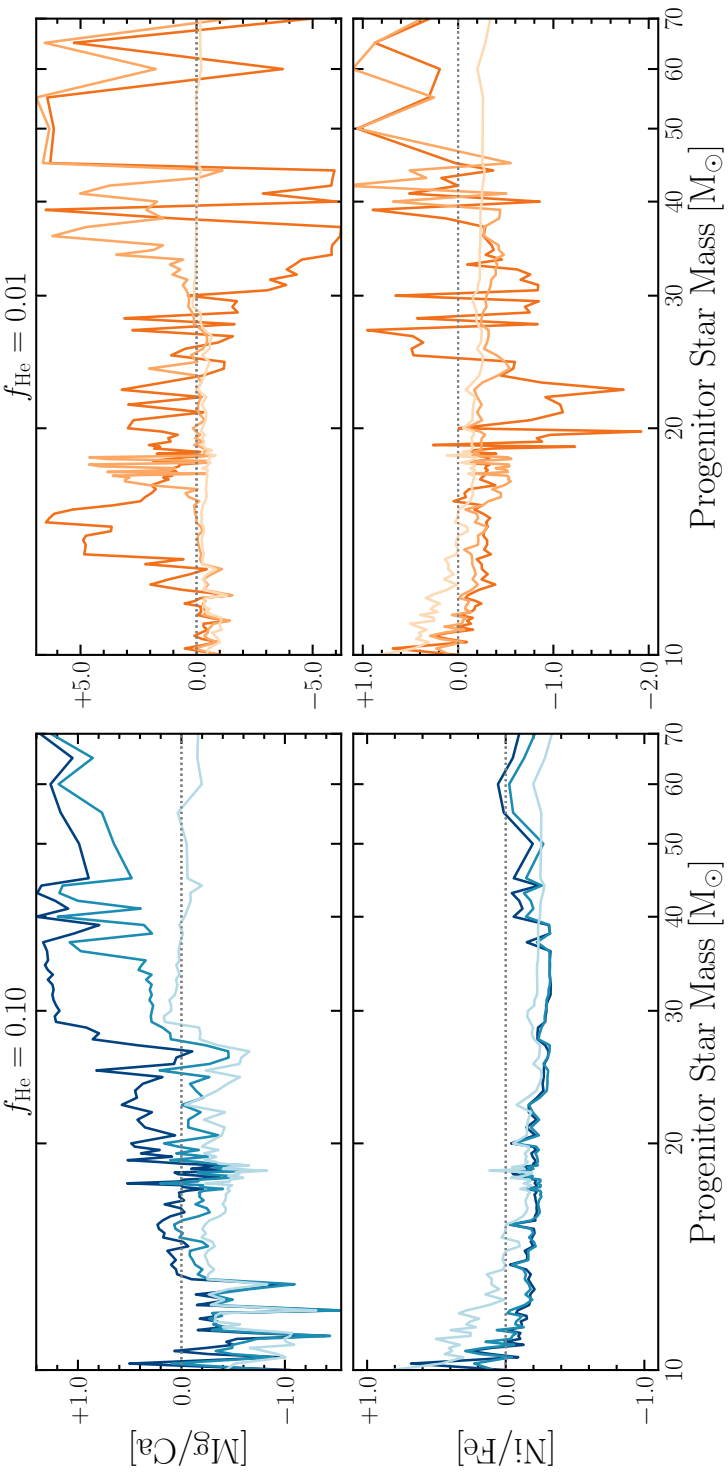

Figure 3.4. [Mg/Ca] and [Ni/Fe] yields as a function of the progenitor star mass for a range of stellar properties. As indicated by the title, the two left-hand panels show the yields associated with stars that undergo the fiducial amount of mixing between stellar layers (10 per cent of the He core size). The progressively lighter blue lines correspond to progressively more energetic explosions. Specifically, dark to light shades highlight a 0.9, 1.8, and 10 B explosion, respectively. The orange lines in the right-hand panels highlight the variability of the yields when a star experiences minimal mixing between the stellar layers (1 per cent of the He core size). The progressively lighter orange lines correspond to the same change in explosion energy. Finally, the horizontal dotted line indicates the solar abundance of these abundance ratios.

the chemical products of multiple SNe. The progenitors of these SNe formed obeying an underlying mass distribution. Given the small number of Population III stars forming in each minihalo, this mass distribution would have necessarily been stochastically sampled. The relative abundances of the stellar population enriched by Population III SNe may therefore show an intrinsic spread.

For any given enrichment model, we would like to calculate the probability of observing each star in our sample. The probability of observing a given abundance pattern (e.g. [Mg/Ca] and [Ni/Fe]) is

$$p_n\big(R_o|R_m\big) = \int p\big(R_o|R_i\big)p\big(R_i|R_m\big)\mathrm{d}R_i \ . \tag{3.4.2}$$

The first term of this integral describes the probability of *observing* a given abundance pattern (R_o) given the intrinsic abundance ratios of the system, R_i. In other words, this variable describes how close the observed measurement is to the true value. We model each abundance ratio by a Gaussian whose spread is given by the observational error. The second term of this integral describes the probability of obtaining an intrinsic abundance pattern given the stochastic enrichment model defined by Equation 3.4.1.

To determine the expected distribution of relative abundances given an enrichment model (i.e. $p(R_i|R_m)$), we construct a grid of IMF model parameters, and sample each grid point 10^3 times. For each iteration, we use the sampled stellar masses to determine the yields of the associated SNe. It is assumed that the SNe ejecta are well-mixed. The resulting number abundance ratio of [Mg/Ca], for example, is therefore given by the total yield of Mg relative to the total yield of Ca from all of the sampled stars. Using this Monte Carlo sampling technique, we can build an N-dimensional probability density function of the expected yields, where N is the number of abundance ratios under consideration. In this work we consider the [Mg/Ca] and [Ni/Fe] abundance ratios (thus, N=2).

In this work, $p(R_i|R_m)$ describes the joint probability of simultaneously producing any given combination of [Mg/Ca] and [Ni/Fe]. Figure 3.5 illustrates how the different enrichment model parameters influence the expected distribution of [Mg/Ca]. The successive panels correspond to changing the slope, number of enriching stars, minimum mass,

maximum mass, explosion energy, and stellar mixing, respectively. The fiducial model parameters used in Figure 3.5 (grey-dashed curves) are: $\alpha = 2.35$, $N_\star = 6$, $M_{\rm min} = 10\,{\rm M}_\odot$, $M_{\rm max} = 35\,{\rm M}_\odot$, $E_{\rm exp} = 0.9$ B, and $f_{\rm He} = 10$ per cent. From this figure it is clear that the expected distributions of intrinsic abundances are sensitive to the average number of Pop III stars that enriched the second generation of stars. Thus, given an appropriate sample of observed stellar abundances, this model can be used to estimate the average number of Population III SNe that have chemically enriched the surviving Population II stars. Under the assumption that each surviving star is enriched by the well-mixed SNe ejecta from one minihalo, this analysis can be used to gauge the multiplicity of the first stars.

3.4.2 Likelihood analysis

The likelihood of an enrichment model is given by:

$$\mathcal{L} = \prod_n p_n(R_o|R_m) \ , \tag{3.4.3}$$

To estimate the enrichment model parameters that provide the best fit to the observed abundances, we utilise the EMCEE software package (Foreman-Mackey et al., 2013) to conduct an MCMC likelihood analysis. In this analysis, we adopt uniform priors across all of the model parameters bounded by:

$$\begin{aligned} 1 \leq \quad & N_\star & \leq 100 \ , \\ -5 \leq \quad & \alpha & \leq 5 \ , \\ 20 \leq \quad & M_{\rm max}/{\rm M}_\odot & \leq 70 \ , \\ 0.3 \leq \quad & E_{\rm exp}/10^{51}{\rm erg} & \leq 10 \ , \\ 0 \leq \quad & f_{\rm He} & \leq 0.25 \ . \end{aligned}$$

These boundary conditions are chosen to cover the physically motivated parameter space, given our assumptions about Population III star formation. The number of massive stars that chemically enrich their environment via CCSNe is expected to be small. The slope of the power-law that dictates Population III star formation is still unknown, we therefore

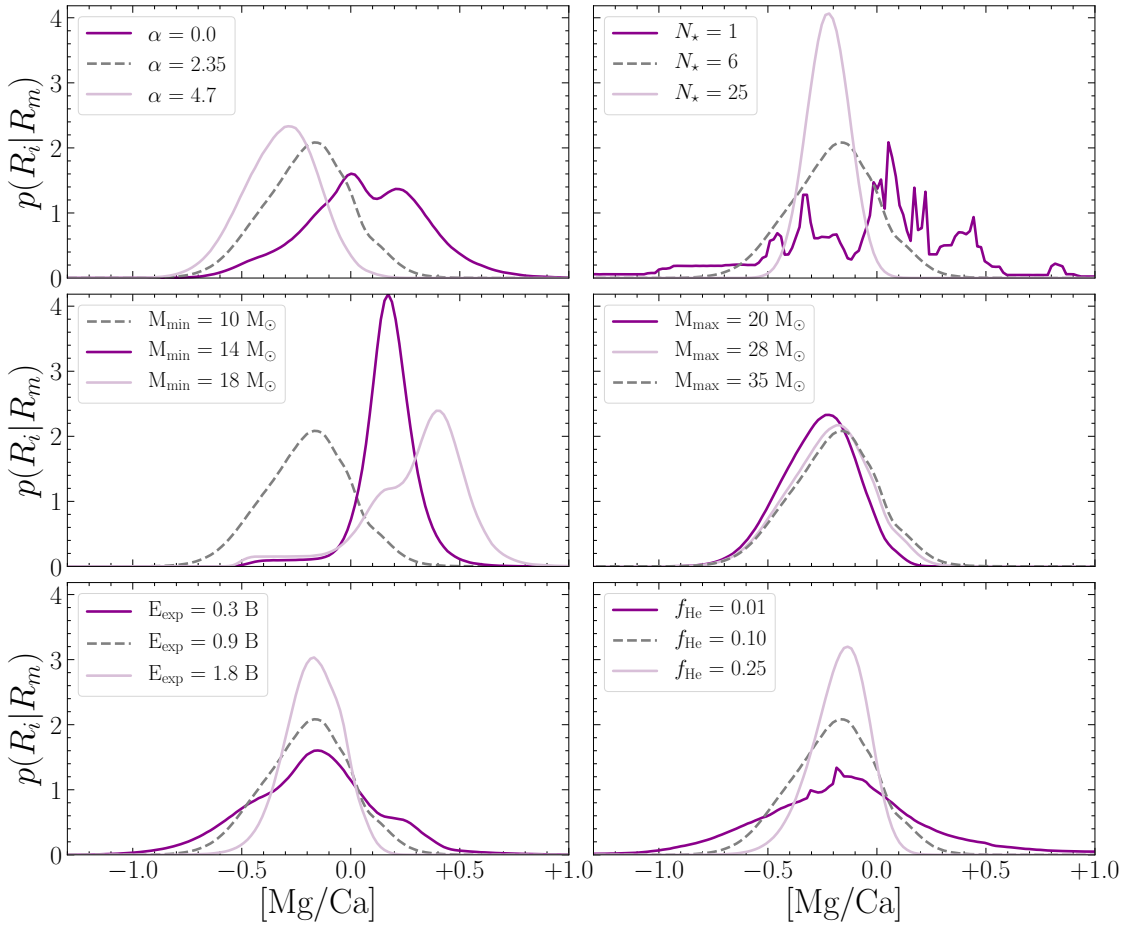

Figure 3.5. Probability distribution of the intrinsic [Mg/Ca] ratio that would be expected for a range of underlying enrichment models. From top left to bottom right, the successive panels correspond to changing the slope, number of enriching stars, minimum mass, maximum mass, explosion energy, and degree of mixing. Unless otherwise stated in the legend, the model parameters of these distributions are $\alpha = 2.35$, $N_\star = 6$, $M_{\rm min} = 10\ {\rm M}_\odot$, $M_{\rm max} = 35\ {\rm M}_\odot$, $E_{\rm exp} = 0.9$ B, and $f_{\rm He} = 10$ per cent (displayed as the grey dashed line in all panels as a point of comparison).

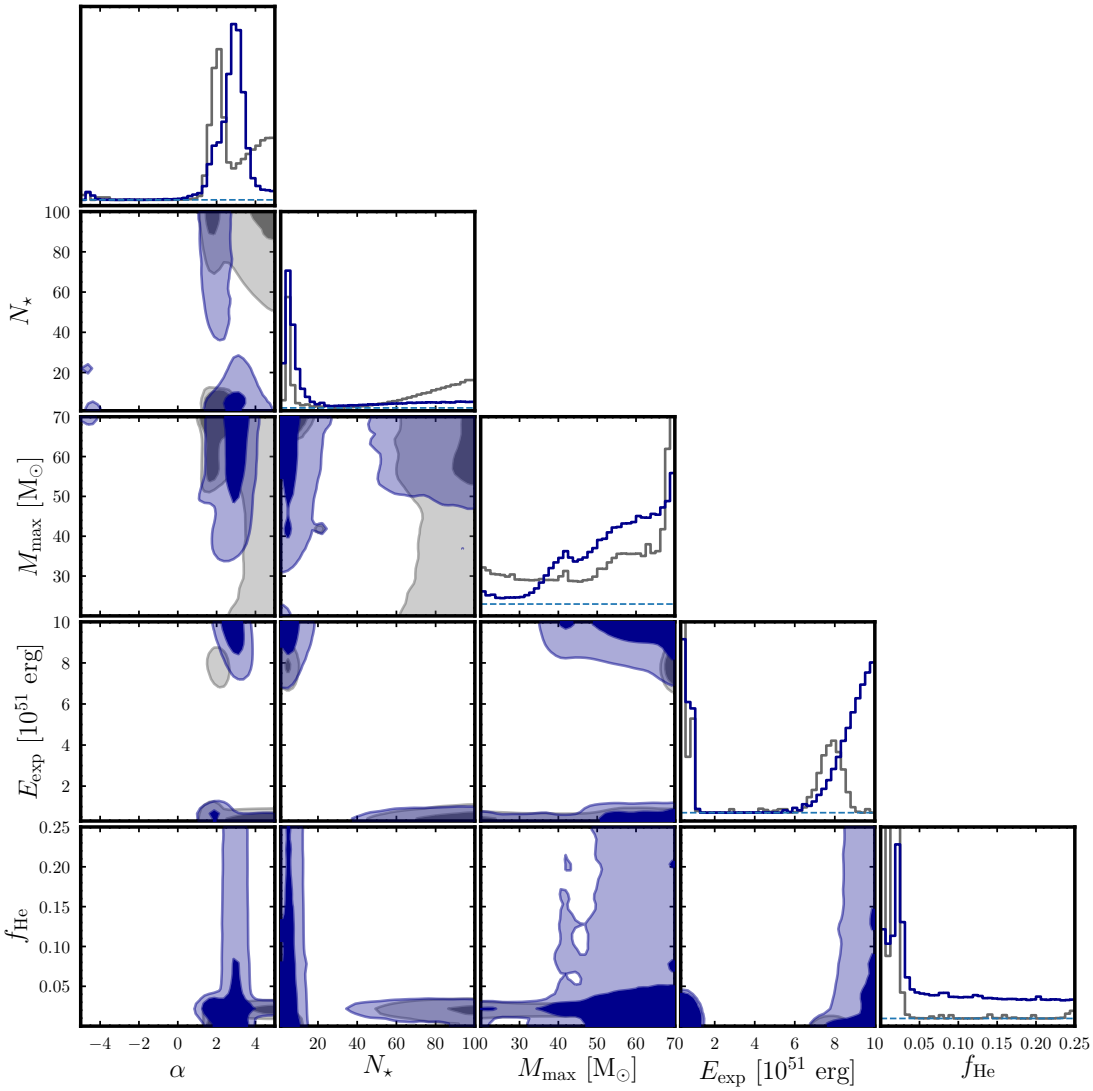

Figure 3.6. The marginalised maximum likelihood distributions of our stochastic chemical enrichment model parameters (main diagonal), and their associated 2D projections, given the abundances of a sample of metal-poor MW halo stars. The dark and light contours show the 68% and 95% confidence regions of these projections, respectively. The horizontal blue dashed lines in the diagonal panels mark where the individual parameter likelihood distributions fall to zero. The grey distributions correspond to the simultaneous analysis of the stars from C04, B09, Y13, and R14. The blue distributions are the result of removing the R14 data from the sample.

have parameterised the IMF of massive stars ($M > 10\ M_{\odot}$) as a power-law IMF, which is consistent with the shape found in the local Universe. The slope of this power-law for local star formation is given by $\alpha = 2.35$ (Salpeter 1955; see Bastian et al. 2010 for a review). The minimum mass of the enriching stars is fixed at $M_{\rm min} = 10\ {\rm M}_{\odot}$ as it is assumed that all stars above this mass limit are capable of undergoing core-collapse. The upper bound on the mass of the enriching stars coincides instead with the onset of pulsational pair instability SNe (Woosley, 2017). The boundary conditions on both the average SN explosion energy and mixing prescription cover all of the values explored in HW10. These simulations calculated the SNe yields for discrete combinations of M, $E_{\rm exp}$, and $f_{\rm He}$; we linearly interpolate over this 3D parameter space for our analysis.

Similar to the approach from Welsh et al. (2019, 2020), we begin our analysis with 400 randomly initialised walkers. These walkers each take 10 000 steps to converge on the stable posterior distributions shown in Figure 3.6. The grey contours highlight the result of considering all of the stars in our chosen sample. We find that the mass distribution of the enriching Population III stars is broadly consistent with a Salpeter ($\alpha = 2.35$) IMF; however, the bottom-heavy tail of the distribution is poorly constrained. Similarly, the maximum mass of the enriching stars is largely unconstrained, while showing a slight preference towards higher values. This analysis suggests that the enriching progenitors have experienced minimal mixing between stellar layers ($f_{\rm He} \sim 0.03$). The remaining parameters, $N_{\star}$ and $E_{\rm exp}$, show two possible scenarios. If $N_{\star} < 20$ then the yields of hypernovae ($E_{\rm exp} \sim 8$ B) are most suitable. Alternatively, if $N_{\star} > 30$, we find that these Population II stars are best modelled with the yields of weak ($E_{\rm exp} \sim 0.3$ B) Population III SNe. This latter scenario is consistent with the result of HW10 (see their figure 12). If we repeat this analysis after removing the R14 data (see the blue contours in Figure 3.6), these two scenarios persist. However, there is a clear preference towards the low $N_{\star}$ scenario that, in this case, also coincides with an unconstrained mixing prescription. Removing the R14 data reduces the allowed parameter space of our model, even though the observed distributions of [Mg/Ca] and [Ni/Fe] of each independent survey are broadly consistent (see Figure 3.2). This highlights that the estimated model parameters are sensitive to

small differences in the observationally measured abundances. Before we investigate the potential origins of this difference, we note that repeating our analysis using only the abundances of the 130 giants in our sample (defined as those with $\log g < 3$) has a negligible impact on our parameter estimates. Similarly, removing potentially peculiar stars with elevated Mg ([Mg/Fe] > +1) does not change the parameter estimates. This is not surprising, as the majority of the stars in our sample have [Mg/Fe] < +1 (see Figures 3.1 and 3.2).

3.4.3 Maximum likelihood results

To investigate the quality of the estimated enrichment models, we use the posterior distributions of the model parameters to generate the expected stellar abundances of [Mg/Ca] and [Ni/Fe]; we then compare these distributions to the observed abundances of the stellar sample. This exercise indicates that our inferred model parameters, based on the C04, B09, Y13, and R14 samples, does not encompass the full extent of the data. In particular, Figure 3.7 highlights a bimodal distribution of [Ni/Fe], which is a result of the bimodal distribution of $E_{\rm exp}$ (and hence $N_\star$) seen in Figure 3.6. As can be seen in Figure 3.4, there are a range of models that can capture the [Ni/Fe] range seen in the data ($-0.4 \lesssim$ [Ni/Fe] $\lesssim +0.4$), including minimally mixed weak SNe and high energy SNe with 'normal' mixing. However, these two possible ways to explain the broad [Ni/Fe] distribution are unable to simultaneously reproduce the observed [Mg/Ca] distributions. In particular, our model does not simultaneously favour supersolar [Mg/Ca] and [Ni/Fe] abundances. This highlights the importance of simultaneously modelling the interdependence of the $p(R_i|R_m)$ distributions for all elements being considered in a stochastic enrichment model, as discussed in Section 3.4.1.

From Figure 3.8, we can see that the distinction between the model and observed distributions are less pronounced when we repeat our analysis after removing the R14 data. The R14 data comprise most of our sample, and exhibit somewhat elevated [Mg/Ca] values, compared with the rest of the sample (see Figure 3.1). While this offset is $\sim$ 0.1 dex,

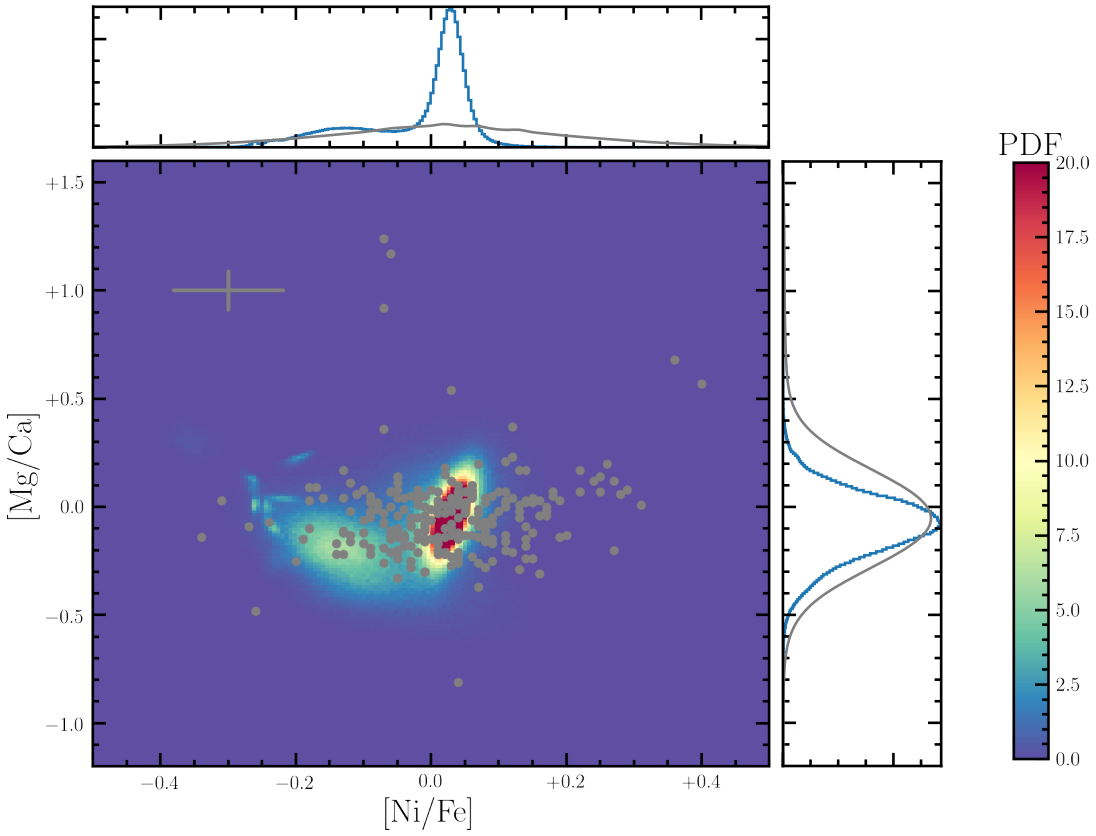

Figure 3.7. [Mg/Ca] and [Ni/Fe] data of all of the samples with the median error plotted in the top left corner. The background contours highlight the PDF of the expected abundances given our inferred chemical enrichment model. The blue histograms in the top and left panels show the 1D projections of the expected [Ni/Fe] and [Mg/Ca] abundances, respectively, given our inferred enrichment model. The grey curves show the generalised histograms of the data used in our analysis.

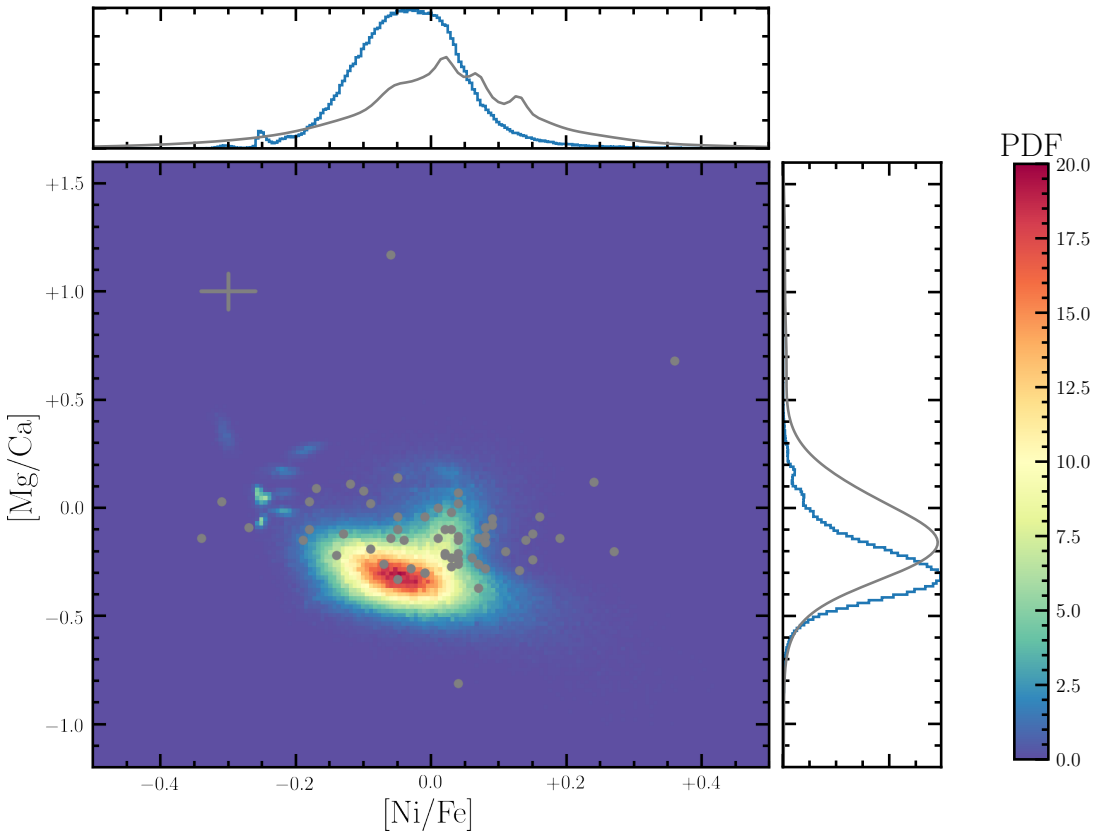

Figure 3.8. Same as Figure 3.7 for the case when we exclude the R14 data from our sample.

combined with the broad distribution of [Ni/Fe], it is large enough to affect the parameter constraints of our model. To investigate this further, we have compared the abundances of the stars that appear in both the *First Stars* series and the R14 sample (in total, there are 26 duplicate stars that also meet our selection criteria). For these stars, the median [Mg/Ca] offset is 0.14 ± 0.07 and the median [Ni/Fe] offset is 0.05 ± 0.13 (where the quoted confidence interval represents a robust estimate of the standard deviation). We can use these offsets to apply a blanket 'correction' to the R14 sample. Repeating our analysis, given this modified sample, produces parameter estimates consistent with those found after removing the R14 data (see Appendix B.2 for the associated corner plot). We therefore conclude that our stochastic chemical enrichment model is able to reproduce the observations if we exclude the R14 data (or, indeed, calibrate these data to that of the other samples). As discussed in Section 3.2, the somewhat elevated Mg abundances reported by R14 are due to their adopted approach for estimating the effective temperature. Going forward, it is clear that the relative element abundance measurements need to be reported with an accuracy of better than ~ 0.05 dex.

Given that our model is able to reproduce the observations when we exclude the R14 data (see Figure 3.8), we favour the maximum likelihood results of our model parameters based on the C04, B09, and Y13 combined sample. We find that the average number of massive Population III stars that best describe the observed [Mg/Ca] and [Ni/Fe] abundances of these Population II stars is $\hat{N}_\star = 5^{+13}_{-3}$ where the quoted errors, here and subsequently, are the 68 per cent confidence region associated with the maximum likelihood value. These stars form obeying a power-law IMF with a slope $\hat{\alpha} = 2.9^{+0.9}_{-0.6}$. The maximum mass of the enriching stars is unconstrained while the marginalised 1D posterior distribution of $E_{\rm exp}$ tends towards the two extremes; if we consider the scenario with $N_\star < 18$, then we infer $\hat{E}_{\rm exp} > 6$ B (95 per cent confidence). Finally, the preferred mixing prescription is $\hat{f}_{\rm He} = 0.03^{+0.10}_{-0.03}$. Thus, our analysis suggests that the observed abundances of this metal-poor stellar sample are best described by enrichment from a small handful of Pop III hypernovae whose progenitors experienced minimal mixing between the stellar layers. Additionally, the slope of the underlying IMF (at least for masses that exceed 10 $M_\odot$) is

consistent with that of a Salpeter distribution ($\alpha = 2.35$).

3.5 Discussion

We first investigate the sensitivity of our results to the stellar atmosphere modelling. We then discuss the limitations of our model, and in particular, the chemical yields of massive stars. We close this section by drawing comparisons between the analysis of the most metal-poor stars and DLAs.

3.5.1 Departures from local thermodynamic equilibrium

One of the assumptions that underpins the observational data is that the absorption lines are all formed in regions of local thermodynamic equilibrium (LTE). Neglecting departures from LTE is common practice when determining the stellar chemical abundances. Including non-LTE processes requires computationally expensive calculations that are generally dependent on the metallicity and surface temperature of the star under consideration, and requires knowledge of the radiative and collisional processes that drive the gas out of LTE. These calculations are unique to the element being considered and, indeed, are also influenced by its initial abundance (Andrievsky et al., 2010). While difficult to compute, these calculations can improve both the accuracy and the precision of the Mg, Ca, and Ni abundance determinations.

Non-LTE Mg abundances for a subset of our stellar sample have been computed by Andrievsky et al. (2010). The non-LTE corrections to Mg typically increase the Mg abundance by ~ 0.3 dex. Although non-LTE corrections to Ca are not currently available for the stars considered in this work, we note that the relative correction to the [Mg/Ca] abundances depends on metallicity (Ezzeddine et al., 2018); around [Fe/H] $\simeq -3$, the [Mg/Ca] abundance should be reduced by ~ 0.1 dex. Furthermore, this correction becomes more significant at even lower metallicity (Sitnova et al., 2019). Therefore, applying a

non-LTE correction to Mg and Ca might bring our model into better agreement with the data. We look forward to a more detailed assessment of the [Mg/Ca] abundances when non-LTE corrections are available for a large fraction of the stellar sample employed in this work.

3.5.2 Assessment of the yields

We now consider potential improvements that could be made to the nucleosynthetic yields used in our model. As discussed in the previous section, the yields are unable to produce supersolar [Mg/Ca] at the same time as supersolar [Ni/Fe] (see Figures 3.4 and 3.7). When removing the R14 data (see Figure 3.8), the model cannot reproduce the large spread of [Ni/Fe] values; in particular, the highest values of [Ni/Fe] deviate from the best-fit model. Assuming that the observed abundances are reliable, this suggests that either: (1) massive metal-free stars are not the only sources responsible for the chemical enrichment of the most metal-poor stars; or (2) the simulated yields do not fully capture the physics that is necessary to reproduce the observed abundances.

Considering the first possibility, there are a number of alternative sources of enrichment that are not considered in this work. These include low mass metal-free stars (e.g Campbell & Lattanzio 2008), pair instability SNe (PISNe) (e.g. Heger & Woosley 2002), pulsational pair-instability SNe (pPISNe) (e.g. Woosley 2017), and rapidly-rotating near-pristine massive stars (e.g. Meynet et al. 2010). There are reasonable reasons to discount the first three sources, for example: (1) the most metal-poor stars are believed to have formed in the very early universe, when there would not have been enough time for low and intermediate mass stars to contribute their enrichment. (2) PISNe produce a lot of metals, but their distinct chemical signatures (e.g. a low [α/Fe] ratio, and a strong odd-even effect) are not seen in any of the stars of our sample. Furthermore, the yields of PISNe are expected to be incorporated in stars of metallicity [Fe/H] ~ -2.0 (e.g. Aoki et al. 2014) which is somewhat higher than the stars in our sample. (3) pPISNe also produce a distinct chemical signature (including a very high [α/Fe] ratio). This signature is not observed in any stars of our sample. Finally, although we cannot discount enrichment from the rotating

near-pristine stars based on the current data, this may become possible in the future by exploring a larger grid of models or by measuring the helium mass fraction of the stellar sample.

We now consider the possibility that the simulated yields are not yet able to fully capture the physics underpinning the stellar evolution and SN explosions of metal-free stars. In recent years substantial progress has been made in simulating CCSNe in 3D (e.g. Vartanyan et al. 2018). However, the mechanism that drives CCSNe is still unknown. We therefore lack a description of these SNe from first principles, and thus model calculations need to parameterise the explosion model. As discussed in Section 3.4, the HW10 simulations are performed in 1D using non-rotating models. Calculations performed in multiple dimensions are better able to capture the impact of both Rayleigh-Taylor instabilities and stellar rotation (Joggerst et al., 2010a,b; Vartanyan et al., 2018). Furthermore, multidimensional models allow for departures from spherical symmetry, providing a more physically motivated scenario. We refer the reader to Müller (2019) for a discussion of potential ways to observationally decipher this explosion mechanism and to Müller (2020) for a review of the state-of-the-art simulations in this field.

Indeed, being able to accurately simulate the complexity of a CCSN is a tall order. Surveys of metal-poor stars (e.g. Starkenburg et al. 2017; Da Costa et al. 2019) are uncovering a slew of chemically peculiar stars whose abundances are challenging to explain through the yields of CCSNe alone. An analysis of the abundances of UMP stars has shown that the HW10 yields are not always sufficient (Placco et al., 2016). Further, the recent detection of elevated Zn in the chemically peculiar star HE 1327-2326 has motivated the consideration of aspherical SNe models (Ezzeddine et al., 2019). We thus conclude that nucleosynthetic yields provide an illustrative model of chemical enrichment, but because of the various simplifications involved, it is not yet clear how accurately the yields will represent the data. Moving forward, we highlight the importance of quantifying the errors of nucleosynthetic yields, and including this uncertainty in the modelling of observational data.

3.5.3 Comparison with DLAs

A complementary approach to studying the chemistry of stellar relics is the study of minimally processed gas at high redshift (Erni et al., 2006; Pettini et al., 2008; Penprase et al., 2010). There are some gaseous systems at $z \sim 3 - 4$ that appear to show *no* discernible metals (e.g. Fumagalli et al. 2011 and Robert et al. 2019). These systems may have remained *entirely* untouched by the process of star formation. There are other systems, whose metallicities are comparable to that of EMP stars, that may have been solely enriched by the first generation of stars (e.g. Cooke et al. 2017). These systems, defined as DLAs if the column density of neutral hydrogen exceeds $\log_{10} N(\mathrm{H\,I})/\mathrm{cm}^{-2} > 20.3$, offer an alternative environment to search for a unique Population III signature.

In contrast to stellar relics, whose abundance determinations require the consideration of complex processes, the underlying physics required to determine the chemical composition of DLAs is rather simple; the column density of neutral hydrogen in these systems is sufficiently high to self-shield the gas, leaving all metals in a single dominant ionisation state. We can therefore determine the elemental abundances of these systems with a high degree of precision ($\sim$ 0.01 dex; Wolfe et al. 2005). Additionally, when investigating these systems (as done in Welsh et al. 2019, 2020) we can utilise the abundance ratios of the most abundant chemical elements, including [C/O]. The simulated [C/O] HW10 yields share an almost monotonically decreasing relationship with progenitor star mass. This is invaluable when attempting to estimate the mass distribution of the enriching stars. While the abundances of DLAs are, in principle, more straightforward to determine, these systems do not necessarily probe the multiplicity of the first stars (i.e. the average number of massive Population III stars forming in a given minihalo). Instead, it is possible that the constituent DLA gas has originated from multiple minihaloes. Thus, the combined analysis of both EMP DLAs and EMP stars offers a novel opportunity to investigate the number of minihaloes that have chemically contributed to these high redshift structures (i.e. $N_{\mathrm{halos}} = N_{\star\,\mathrm{DLAs}}/N_{\star\,\mathrm{Pop\,II}}$). Given the currently available data and suite of yield calculations, we can estimate the posterior distribution of N_{halos} given the inference on

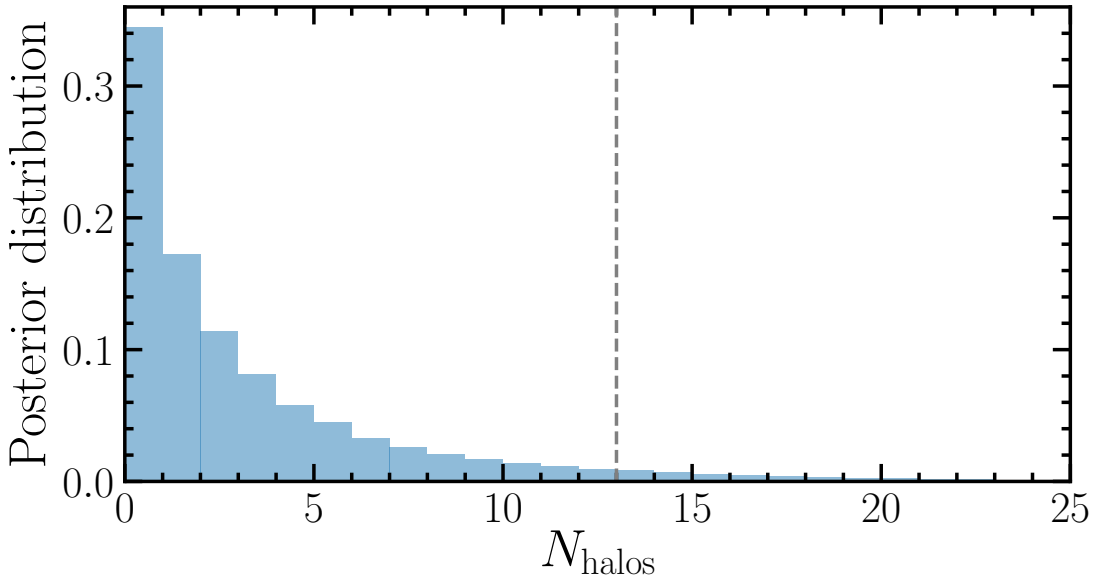

Figure 3.9. The posterior distribution of the average number of minihaloes that may have chemically contributed to the most metal-poor DLAs given our estimate of $N_{\star\,\rm DLAs}$ from Welsh et al. 2019 and our estimate of $N_{\star\,\rm Pop\,II}$ from this work. The vertical dashed line indicates the 95$^{\rm th}$ percentile of this distribution and corresponds to our quoted 2σ upper limit.

$N_{\star\,\rm DLAs}$ from Welsh et al. (2019) and $N_{\star\,\rm Pop\,II}$ from this work. The results of this comparison are shown in Figure 3.9 and indicate that the maximum likelihood value of $\hat{N}_{\rm halos} = 1$. The most metal-poor DLAs may therefore contain the chemical products from just 1 or 2 minihaloes; they could also represent the clouds of gas from which some Population II stars formed. However, the tail of the $N_{\star\,\rm DLAs}$ distribution is quite broad and we therefore conservatively conclude $N_{\rm halos} < 13$ (95 per cent confidence). This upper limit is indicated by the vertical dashed line in Figure 3.9. Given more precise constraints, this tool may provide a test of galaxy formation on the smallest scales. We look forward to comparing the enrichment histories of these systems in detail with future data.

3.6 Conclusions

In this paper we have applied a novel stochastic chemical enrichment model to investigate the possible enrichment history of a sample of metal-poor Milky Way halo stars using the [Mg/Ca] and [Ni/Fe] abundances from four historic surveys (C04, B09, Y13, and R14).

This is the first analysis to consider the number of massive Population III stars that have chemically enriched these stellar relics. Our main conclusions are as follows:

(i) With the adopted nucleosynthetic yields, our stochastic chemical enrichment model is able to reproduce the observed abundances of a stellar subsample comprising the C04, B09, and Y13 data. In this scenario, our model shows preferential enrichment from a low number of Population III hypernovae.

(ii) Specifically, this model suggests that a typical metal-poor star has been chemically enriched by $\hat{N}_{\star} = 5^{+13}_{-3}$ Population III hypernovae ($\hat{E}_{\rm exp} > 6$ B ; 95 per cent confidence) that experienced minimal mixing between the stellar layers ($\hat{f}_{\rm He} = 0.03^{+0.10}_{-0.03}$). The IMF slope of this enriching population is found to be broadly consistent with that of a Salpeter distribution ($\hat{\alpha} = 2.9^{+0.9}_{-0.6}$). Unless otherwise stated, these errors represent the 68 per cent confidence intervals of our estimates.

(iii) We consider the value of $N_{\star}$ reported in this paper to be a proxy for the multiplicity of massive Population III stars. By comparing this result to the $N_{\star}$ value inferred for the most metal-poor DLAs (see Welsh et al. 2019), we estimate the average number of minihaloes that may have chemically contributed to these low mass structures at $z \sim 2-3$. We find $N_{\rm halos} < 13$ (95 per cent confidence). The maximum likelihood value of this distribution suggests that the most metal-poor DLAs may contain the chemical products from only a few minihaloes. In future, with more precise constraints, we hope to probe whether these DLAs resemble the gas that some Population II stars formed from.

(iv) In our analysis we utilise the abundance ratios calculated under the assumption of LTE. Recent work considering the non-LTE corrections to the observed [Mg/Ca] abundance ratios of these data may bring our model into better agreement with the data (Ezzeddine et al., 2018; Sitnova et al., 2019). Similarly, the different methods used to infer the effective temperature of the stars in our sample produce a [Mg/Ca] offset of $\sim +0.1$ dex (see the discussion in R14). Although this difference is small, we

find that the yields (and our model parameters) are sensitive to these small changes in abundance ratios. Thus, in future analyses, we require abundance measurements reported with an accuracy of ~ 0.05 dex to produce reliable estimates.

(v) We also comment that the various parameterisations involved in nucleosynthetic yield calculations mean that it is not yet clear how accurately the adopted yields capture all of the relevant physics. Going forward, it would be helpful to consider the uncertainties of the simulated yields in future analyses.

Finally, we emphasis that utilising this model to investigate the enrichment of both Population II stars and the *most* metal-poor DLAs may reveal, not only the multiplicity of the first stars, but the chemical enrichment of some of the lowest mass structures at $z \sim 3$. It is therefore a promising tool for investigating early structure formation. Future modifications to this model may offer an alternative way to study inhomogeneous metal-mixing and the possibility of externally enriched minihaloes.

CHAPTER 4

A bound on the $^{12}C/^{13}C$ ratio in near-pristine gas with ESPRESSO

The following chapter is reprinted from the publication "A bound on the $^{12}C/^{13}C$ ratio in near-pristine gas with ESPRESSO." (Welsh et al., 2020). In the previous two chapters we modelled the chemical enrichment of the most metal-poor DLAs and the most metal-poor stars from the literature. In these chapters, we searched for the chemical signatures of massive metal-free stars. We now extend this investigation to search for the signatures of low-mass Population III stars using the carbon isotope ratio. This search has recently become possible thanks to the advent of ESPRESSO, the ultra-stable spectrograph. We present the first bound on the carbon isotope ratio in a near-pristine DLA and find the current observational data cannot rule out enrichment from low-mass Population III stars. These ESPRESSO data were collected on 2019 August 28 (PI: R. Cooke; thesis author co-I). The subsequent data reduction was led by the programme PI with help from the myself. Using the entire chemistry of this environment and our stochastic chemical enrichment model, we trace the chemical enrichment history of this DLA. This analysis suggests that the DLA towards J0035−0918 may have experienced a hiatus in star formation following the epoch of reionisation and, thus, may have been impacted by reionisation quenching.

Abstract: Using science verification observations obtained with ESPRESSO at the Very Large Telescope (VLT) in 4UT mode, we report the first bound on the carbon isotope ratio $^{12}C/^{13}C$ of a quiescent, near-pristine damped Lyα (DLA) system at $z = 2.34$. We infer a limit $\log_{10}{}^{12}C/^{13}C > +0.37\,(2\sigma)$. We use the abundance pattern of this DLA, combined with a stochastic chemical enrichment model, to infer the properties of the enriching stars, finding the total gas mass of this system to be $\log_{10}(M_{\rm gas}/{\rm M}_\odot) = 6.3^{+1.4}_{-0.9}$ and the total stellar mass to be $\log_{10}(M_\star/{\rm M}_\odot) = 4.8 \pm 1.3$. The current observations disfavour enrichment by metal-poor Asymptotic Giant Branch (AGB) stars with masses $< 2.4\,{\rm M}_\odot$, limiting the epoch at which this DLA formed most of its enriching stars. Our modelling suggests that this DLA formed very few stars until $\gtrsim 1$ Gyr after the cosmic reionization of hydrogen and, despite its very low metallicity ($\sim 1/1000$ of solar), this DLA appears to have formed most of its stars in the past few hundred Myr. Combining the inferred star formation history with evidence that some of the *most* metal-poor DLAs display an elevated [C/O] ratio at redshift $z \lesssim 3$, we suggest that very metal-poor DLAs may have been affected by reionization quenching. Finally, given the simplicity and quiescence of the absorption features associated with the DLA studied here, we use these ESPRESSO data to place a bound on the possible variability of the fine-structure constant, $\Delta\alpha/\alpha = (-1.2 \pm 1.1) \times 10^{-5}$.

4.1 Introduction

The earliest episodes of star formation can be studied by measuring the chemical composition of near-pristine environments. Indeed, there may be some environments in the Universe that have been solely enriched by the first generation of metal-free stars (also known as Population III stars) — a population of stars that we still know very little about; we are yet to discover a star that shows no detectable metals. However, dedicated surveys (e.g. Bond 1980; Beers et al. 1985, 1992; Keller et al. 2007; Christlieb et al. 2008; Aoki et al. 2013; Caffau et al. 2013; Li et al. 2015; Aguado et al. 2016; Howes et al. 2016;

Starkenburg et al. 2017; Da Costa et al. 2019) have revealed an interesting trend in the chemical composition of the lowest metallicity stars. Notably, there is an overabundance of carbon in some of the most iron-poor stars found in the halo of the Milky Way; indeed, every star with a measured iron abundance [Fe/H] ≤ -5.0 exhibits a strong carbon enhancement[1] (Christlieb et al., 2004; Frebel et al., 2005; Aoki et al., 2006; Frebel et al., 2015; Allende Prieto et al., 2015; Nordlander et al., 2019).

Despite concentrated efforts, and increasingly sophisticated cosmological hydrodynamic simulations, we have yet to establish whether or not low mass ($\sim 1\,M_\odot$) metal-free stars can form. Seminal simulations of Population III star formation, like those of Tegmark et al. (1997); Barkana & Loeb (2001); Abel et al. (2002); Bromm et al. (2002), suggested an initial mass range from $100 - 1000\,M_\odot$. As the resolution of these simulations improved, alongside our ability to incorporate more detailed physics, the predicted minimum mass of the first stars has decreased. Current simulations suggest that Population III stars were dominated by stars in the mass range $10 - 100\,M_\odot$ (Turk et al., 2009; Greif et al., 2010; Clark et al., 2011; Hirano et al., 2014; Stacy et al., 2016). Given that we are yet to discover a metal-free star around the Milky Way, one might conclude that Population III stars were dominated by more massive ($> 10\,M_\odot$) stars that lived relatively short lives. There are, however, simulations that suggest low mass Population III stars can form, either through efficient fragmentation of the primordial gas (Clark et al., 2011; Stacy et al., 2016) or through the re-cooling of preserved pristine gas that has been photoionised by a nearby burst of metal-free star formation (Stacy & Bromm, 2014).

A complementary approach to study the imprints of Population III stars in second generation (Population II) stars is the analysis of metal-poor absorption line systems (Erni et al., 2006; Pettini et al., 2008; Penprase et al., 2010). Of all known damped Lyα systems (DLAs, which are defined as absorption line systems with a neutral hydrogen column density $\log_{10} N(\mathrm{H\,I})/\mathrm{cm}^{-2} > 20.3$), only one gas cloud reportedly shows a carbon enhancement similar to that seen in metal-poor halo stars (Cooke et al. 2011a; see also, Dutta

[1]Here, and throughout this paper, [X/Y] denotes the logarithmic number abundance ratio of elements X and Y relative to their solar values $\mathrm{X}_\odot$ and $\mathrm{Y}_\odot$, i.e. $[\mathrm{X/Y}] = \log_{10}\left(N_\mathrm{X}/N_\mathrm{Y}\right) - \log_{10}\left(N_\mathrm{X}/N_\mathrm{Y}\right)_\odot$.

et al. 2014; Cooke et al. 2015). This system is located at a redshift $z_{\rm abs} \simeq 2.34$ along the line-of-sight to the quasar SDSS J003501.88−091817.6 (hereafter J0035−0918), and displays a large column density of neutral hydrogen, $\log_{10} N({\rm H\,I})/{\rm cm}^{-2} = 20.43 \pm 0.04$. Previous observations of this DLA towards J0035−0918 have shown that it is one of the least polluted reservoirs of neutral gas currently known, with a relative iron abundance almost 1/1000 that of the Sun. DLAs are thought to be self-shielded from external radiation due to their large H I column density; their constituent elements tend to exist in a single, dominant ionisation state. We can therefore determine the chemical abundance patterns of these systems without needing to apply ionisation corrections. We note there are some reservoirs of partially ionised gas that show *no* detectable metals (e.g. Fumagalli et al. 2011 and Robert et al. 2019). The metal paucity of the DLA towards J0035−0918, alongside the originally reported overabundance of carbon, makes this an interesting environment to search for signatures of Population III stars.

Here, we propose an observational approach to assess the existence or absence of low mass Population III stars. Simulations of stellar evolution have shown that most stellar populations predominantly produce ^{12}C. There are only two channels through which low values of ^{12}C/^{13}C can be produced. These involve either: (1) low mass metal-free stars; or (2) metal-poor intermediate mass Asymptotic Giant Branch (AGB) stars (Campbell & Lattanzio, 2008; Karakas, 2010). Note that both metal-free and metal-enriched massive stars (i.e. $M > 10$ M$_\odot$) produce ^{12}C/^{13}C > 100 (Heger & Woosley, 2010).[2] Therefore, by measuring the carbon isotope ratio of a near-pristine gas cloud, we can test if low mass Population III stars might have contributed to the enrichment. Moreover, because stars of different mass produce different quantities of ^{12}C/^{13}C, we can use the measured abundance as a 'clock' to infer the enrichment time scale of a system. As only the intermediate mass metal-poor stars produce significant yields of ^{13}C, there is a finite time in which a system will retain a distinctive low ^{12}C/^{13}C signature before the ^{12}C-rich yields of low mass stars return the isotope ratio to larger values.

[2]While we utilise the yields of non-rotating stellar models, we note that extremely metal-poor, rapidly-rotating massive (> 7 M$_\odot$) stars are capable of producing $4 < ^{12}$C/^{13}C< 77 (Meynet et al., 2010).

A measurement of the carbon isotope ratio in near-pristine gas relies on our ability to distinguish absorption lines that are separated by a small isotope shift; for the C II λ1334 absorption line, ^{13}C is shifted by -2.99 km s^{-1} relative to ^{12}C. In typical metal-poor DLAs, the overall line profile contains a small number ($\lesssim 5$) of absorption clouds spread over a velocity interval of tens km s^{-1}, where each individual absorption component exhibits a total line broadening of $3 - 5$ km s^{-1}. The DLA towards J0035−0918 is particularly quiescent, where the absorption is concentrated in a single component with an estimated total Doppler width of $b \simeq 3.5$ km s^{-1} (Cooke et al., 2015), which is related to the velocity dispersion of the gas, $\sigma = \sqrt{2}\, b$. With such a system, it may be possible to detect ^{13}C as an asymmetry of the C II λ1334 feature. Such an asymmetry will not be present in the absorption lines of other elements.

A measurement of the ^{12}C/^{13}C ratio has never been attempted in a near-pristine environment. The only high redshift bound currently available using absorption line techniques was based on neutral C I absorption lines associated with a metal-rich ([Zn/H]= −0.49) sub-DLA towards HE 0515−4414 (Levshakov et al., 2006). This study utilised the Ultraviolet and Visual Echelle Spectrograph (UVES; Dekker et al. 2000) at the European Southern Observatory (ESO) Very Large Telescope (VLT), and reported a limit ^{12}C/^{13}C$>$ 80 (95 per cent confidence).

Complementary high redshift measurements of the ^{12}C/^{13}C isotope ratio are afforded by sub-mm studies of the ^{12}CO and ^{13}CO emission lines (Béthermin et al., 2018). However, the sensitivity of current instrumentation means that these works are generally focused on relatively metal-rich galaxies at high redshift.

To reach the required level of accuracy, we need to employ a very high spectral resolution instrument that has an accurate wavelength calibration. Such a requirement is now met with the Echelle SPectrograph for Rocky Exoplanet and Stable Spectroscopic Observations (ESPRESSO; Pepe et al. 2010) at the ESO VLT. This high resolution (R $\simeq$ 70, 000 – 140, 000) spectrograph provides an unprecedented level of wavelength accuracy; when used in 4UT mode, the relative velocity accuracy is better than 5 m s^{-1}, corresponding to an accuracy of $\sim 10^{-4}$ Å at 4000 Å.

In this paper, we present the first bound on the $^{12}C/^{13}C$ isotope ratio of the DLA towards J0035−0918 using ESPRESSO data obtained during the science verification process. These data have also allowed us to explore the chemical enrichment history of this DLA and to place a bound on the fine-structure constant variation. The paper is organised as follows. Section 4.2 describes our observations and data reduction. In Section 4.3 we present our data and determine the chemical composition of the DLA towards J0035−0918 using the detected metal absorption line profiles. We then discuss the chemical enrichment history of this system and infer some of its physical properties in Section 4.4, before drawing overall conclusions and suggesting future work in Section 4.5.

4.2 Observations and data reduction

J0035−0918 is a $m_r = 18.89$ quasar at $z_{\rm em} = 2.42$ whose line-of-sight intersects a large pocket of neutral hydrogen. This intervening gas cloud was identified as a DLA at $z_{\rm abs} \simeq 2.34$ from the Sloan Digital Sky Survey (SDSS) discovery spectrum. The lack of metal lines associated with this DLA motivated follow up observations with the HIgh Resolution Echelle Spectrograph (HIRES; Vogt et al. 1994) on the Keck I telescope by Cooke et al. (2011a). Further observations were carried out using UVES by Dutta et al. (2014). The combined analysis of these UVES and HIRES data revealed that the DLA towards J0035−0918 is one of the least polluted neutral gas clouds currently known with [Fe/H] = −2.94±0.06 (Cooke et al., 2015). Furthermore, it is the only very metal-poor DLA to show an overabundance of carbon relative to iron, [C/Fe] = +0.58 ± 0.16 (Cooke et al., 2015). An enhancement of carbon is thought to be a chemical signature of Population III enriched systems (Beers & Christlieb, 2005). While the DLA towards J0035−0918 is not carbon-enhanced to the same degree exhibited by some metal-poor stars, its enhancement of C and N relative to Fe is a rarity amongst the very metal-poor DLA population.

Previous observations indicated that the DLA towards J0035−0918 is particularly quiescent, with a single absorption component exhibiting a total Doppler parameter of $b \simeq 3.5$ km s^{-1}

(Cooke et al., 2015). The ^{12}C and ^{13}C isotopes produce rest frame absorption features at λ1334.5323 Å and λ1334.519 Å , respectively (Morton, 2003); the isotope shift is therefore just 2.99 km s^{-1}. Given the narrow broadening of this system, it is therefore possible to distinguish between the contribution of each C isotope to the total C II λ1334 line profile. Thus, the DLA towards J0035−0918 is a near-ideal environment to measure the carbon isotope ratio and search for the chemical signature of low mass ($\sim$ 1 M$_\odot$) Population III stars. Given the potential promise of this system, we secured new observations with the ultra-stable ESO ESPRESSO spectrograph.

New data were collected with ESPRESSO in 4UT mode (R $\simeq$ 70, 000) on 2019 August 28 spanning the wavelength range 3800 to 7880Å. We acquired 3×2100 s exposures on target using 8×4 binning in slow readout mode. In 4UT mode, the light from the four UTs is incoherently sent to ESPRESSO. The size of the entrance fibre at each UT is 1.0 arcsec. The average seeing during our observations was 0.64 arcsec. These data were reduced using the EsoRex pipeline, including the standard reduction steps of subtracting the detector bias, locating and tracing the echelle orders, flat-fielding, extracting the 1D spectrum, performing a wavelength calibration, and relative flux calibrations.

Due to the faint nature of our target, we have not performed the conventional sky subtraction which would introduce additional sky and read noise into our data.[3] Given that we are already nearing the magnitude limit of what is feasible with this instrument, we decided to maximise the final combined signal-to-noise ratio (S/N) and model the zero level of the data in our analysis. This will be discussed further in Section 4.3.

As a final step, we combined the three individual exposures using UVES_POPLER[4] with a pixel sampling of 2 km s^{-1}. UVES_POPLER allowed us to manually mask cosmic rays and minor defects from the combined spectrum. The final combined S/N of the data near the C II λ1334 absorption line (at observed wavelength $\lambda_{\rm obs}$ = 4457.8 Å) is S/N $\simeq$ 9. The peak S/N of the data is near 5300 Å (S/N $\simeq$ 30). As will be described in the following section,

[3]This is because the science and sky fibres project to the same number of pixels on the detector. For faint objects, performing a sky subtraction results in counting the sky and read noise twice.

[4]UVES_POPLER is available from:
`https://astronomy.swin.edu.au/~mmurphy/UVES_popler/`

alongside these ESPRESSO data, we utilise the spectra from previous observations of the DLA towards J0035−0918 to model the metal line profiles of this absorption system. These data were recorded with a resolution of $R \simeq 40,000$ and a reported S/N per pixel of S/N $\simeq$ 18 at 4500 Å (Cooke et al., 2011a) and S/N $\simeq$ 13 at 5000 Å (Dutta et al., 2014). We refer the reader to these publications for details of these data.

4.3 Results

We exploit the superior wavelength calibration of ESPRESSO to pin down the redshift of the DLA using O, Al, Si, and Fe absorption lines, and search for a shift/asymmetry of the C II line profile — *relative* to the other metals — indicative of absorption from ^{13}C.

Using the Absorption LIne Software (ALIS) package[5]— which uses a χ-squared minimisation procedure to find the model parameters that best describe the input data — we simultaneously analyse the full complement of high S/N and high spectral resolution data currently available. While the ESPRESSO data provide the most reliable wavelength solution, the UVES and HIRES data can be leveraged alongside the ESPRESSO data to enable a more accurate determination of the metal ion column densities and assist in the determination of the zero-level of the ESPRESSO data. To achieve this, the redshift of the DLA is driven by the accurate wavelength solution provided by the ESPRESSO data. The centre of each absorption feature in the UVES and HIRES data is then modelled with an independent velocity offset to ensure that these data are coincident with the well-calibrated ESPRESSO data.

We model the absorption line profiles as a single component Voigt profile, which consists of three parameters: a column density, a redshift, and a line broadening. We assume that all lines of comparable ionisation level have the same redshift, and any absorption lines that are produced by the same ion all have the same column density. The total broadening of the lines includes a contribution from both turbulent and thermal broadening. The

[5]ALIS is available from:
`https://github.com/rcooke-ast/ALIS`.

turbulent broadening is assumed to be the same for all absorption features, while the thermal broadening depends inversely on the square root of the ion mass; thus, heavy elements (e.g. Fe) will exhibit absorption profiles that are intrinsically narrower than the profiles of lighter elements, (e.g. C). There is an additional contribution to the line broadening due to the instrument.

The nominal ESPRESSO instrument resolution in 4UT mode is $v_{\rm FWHM} = 4.28$ km s^{-1}, and we have explicitly checked this by measuring the widths of ThAr emission lines from the calibration data to infer the instrument full width at half maximum (FWHM) at wavelengths close to the DLA's absorption features. We find that across the wavelength range (4450 – 7830) Å the wavelength specific FWHM varies from 4.14 to 4.53 km s^{-1}. Multiple realisations of this fitting procedure produce results consistent within 1%. We adopt these wavelength specific resolutions as our fiducial choice when fitting the data. However, we also checked that our results did not change when using the nominal instrument FWHM. For the HIRES and UVES data, the respective nominal instrument resolutions are $v_{\rm FWHM} = 8.1$ km s^{-1} and $v_{\rm FWHM} = 7.75$ km s^{-1}. When fitting to the data we allow these to vary as free parameters, since the DLA absorption features are unresolved in the UVES and HIRES data. We found that the choice of instrument resolution does not have a significant impact on the resulting column densities. We have performed additional checks to ensure that the system is best modelled by a single absorption component with a stable redshift; for example, we included fictitious isotope transitions in the fit to the line profiles of other elements (like Si II), and these tests demonstrated that the absorption profiles preferred a single, symmetric absorption line. We have also tested that our result cannot be replicated using a 'mirrored' ^{13}C feature that has an offset from ^{12}C of +2.99km s^{-1} (instead of the true value, −2.99km s^{-1}).

Finally, we note that we simultaneously fit the absorption, quasar continuum, and in the case of the ESPRESSO data, the zero-level of the data. We model the continuum around every absorption line as a low order Legendre polynomial (of order 3). We assume that the zero-levels of the sky-subtracted UVES and HIRES data do not depart from zero (this is confirmed by measuring the troughs of saturated absorption lines). Upon inspection of the

Table 4.1. Ion column densities of the DLA at $z_{\rm abs}$ = 2.340064 towards the quasar J0035−0918. The quoted column densities are based on the combined fit of the available ESPRESSO, UVES and HIRES data. The quoted column density errors are the 1σ confidence limits. We also report the carbon isotope ratio as a 2σ limit.

Ion	**$\log_{10} N$(X)/cm^{-2}**
H I[a]	20.43 ± 0.04
^{12}C II + ^{13}C II	14.29 ± 0.13
N I	13.37 ± 0.04
O I	14.67 ± 0.05
Mg II	12.89 ± 0.13
Al II	11.74 ± 0.04
Si II	13.35 ± 0.04
Fe II	13.01 ± 0.03
Isotope ratio	
$\log_{10} N(^{12}\mathrm{C})/N(^{13}\mathrm{C}) > +0.37$ (2σ)	

[a] The H I column density was reported by Cooke et al. (2015).

sky-subtracted ESPRESSO data, we identified a few emission lines that appear to be due to contamination by a nearby galaxy in the field. These emission lines are not present in the UVES or HIRES data. The redshift of this galaxy was determined through observations using the William Herschel Telescope (WHT) that revealed strong O II λ3727 Å emission at an observed wavelength $\lambda \simeq 4297$ Å, corresponding to $z \simeq 0.15$. This galaxy is just 6.8 arcsec from the line-of-sight to the background quasar (corresponding to an impact parameter of 21 kpc at the redshift of the intervening galaxy). We confirmed that there are no sky or galaxy emission lines that contaminate the DLA absorption lines. Therefore to account for the sky continuum and potential low-level contamination by the continuum of this low redshift galaxy, we include a single parameter to model the zero-level of the ESPRESSO data (assumed constant for all lines).

4.3.1 Ion column densities

The ESPRESSO data, along with the best-fitting model are presented in Figure 4.1, while the corresponding column densities are listed in Table 4.1. The simultaneous analysis of the ESPRESSO+HIRES+UVES data have allowed us to accurately determine the metal column densities, gas kinetic temperature and total Doppler parameter of the DLA.

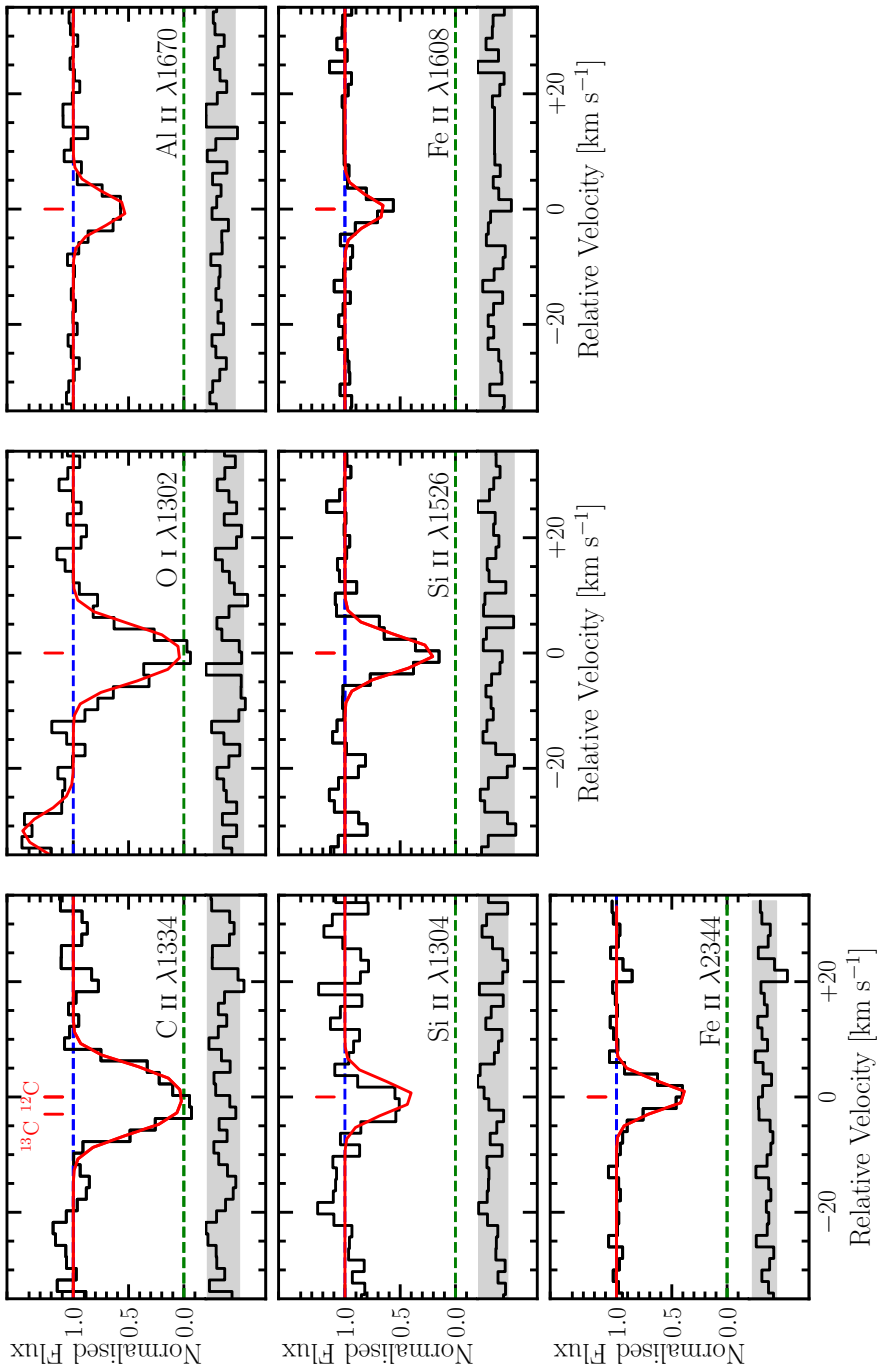

Figure 4.1. Continuum normalised ESPRESSO data (black histograms) of the absorption features produced by metal ions associated with the DLA at $z_{\rm abs}$ = 2.340064 towards the quasar J0035−0918. Overplotted in red is our best-fitting model. The blue dashed line indicates the position of the continuum while the green dashed line indicates the zero-level. The red ticks above the absorption features indicate the centre of the Voigt line profiles. In the panel that shows C II λ1334 absorption, the tick marks at a relative velocity of 0.0 km s^{-1} and −2.99 km s^{-1} represent the centroid of the ^{12}C and ^{13}C absorption line profiles, respectively. Below the zero-level, we show the residuals of this fit (black histogram) where the grey shaded band encompasses the 2σ deviates between the model and the data. Note, in the panel corresponding to O I λ1302, there is an unrelated emission line (due to an unrelated, intervening galaxy at redshift $z \simeq 0.15$; see text) that we have modelled as a Gaussian during the line-fitting procedure.

We find an absorption redshift of $z_{\rm abs} = 2.340064 \pm 0.000001$ and a gas temperature of $T = (9.1 \pm 0.5) \times 10^3$ K. We have found that the line broadening of this system is entirely dominated by its thermal motions; the minor contribution due to the turbulent motions cannot be determined given the current data and, intriguingly, is consistent with no turbulence. The extreme quiescence of this system raises an interesting possibility about the existence of other thermally dominated DLAs yet to be found, or whether known systems that contain multiple absorption components, may still have components that are dominated by thermal broadening.

For the C II absorption, we found that the best-determined parameter combination was the isotope ratio ^{12}C/^{13}C and the total column density of C II, $N(^{12}\text{C II})$+$N(^{13}\text{C II})$. The carbon isotope ratio of this model is $\log_{10}\ ^{12}\text{C}/^{13}\text{C} = +1.15 \pm 0.65$, where the quoted error is simply the diagonal term of the covariance matrix. However, given the large range allowed by this uncertainty, we have performed a suite of detailed Monte Carlo simulations to uncover the posterior distribution of the ^{12}C/^{13}C ratio, given our data. Using the parameters of our best-fitting line model, we generate mock ESPRESSO data varying the relative amount of ^{13}C in the system. These mock data provide perfect (error free) line profiles of C II λ1334 for different values of the ^{12}C/^{13}C isotope ratio (while the total C II column density remains constant). By perturbing these line profiles using the error spectrum of our data, we can emulate how these ESPRESSO data would look as a function of the underlying isotope ratio. We have performed 500 realisations of these perturbations for a variety of underlying isotope ratios. The results of these simulations are presented in Figure 4.2. Given that our line fitting procedure, applied to the real data, suggests a central value $\log_{10}\ ^{12}\text{C}/^{13}\text{C} = +1.15$, we infer $\log_{10}\ ^{12}\text{C}/^{13}\text{C} > +0.37$ (2σ). This lower bound is visualised in Figure 4.3, which shows the model line profiles for various ^{12}C/^{13}C abundance ratios. The line corresponding to $\log_{10}\ ^{12}\text{C}/^{13}\text{C} = +0.37$ falls at the edge of the asymmetric line profile where the ^{13}C absorption is most noticeable; the corresponding residuals are also at the 2σ boundary of the model fit. As the amount of ^{12}C relative to ^{13}C in a system increases, the asymmetry due to the presence of ^{13}C becomes increasingly subtle in the C line profiles. This is, in part, why we expect to recover a broad range of

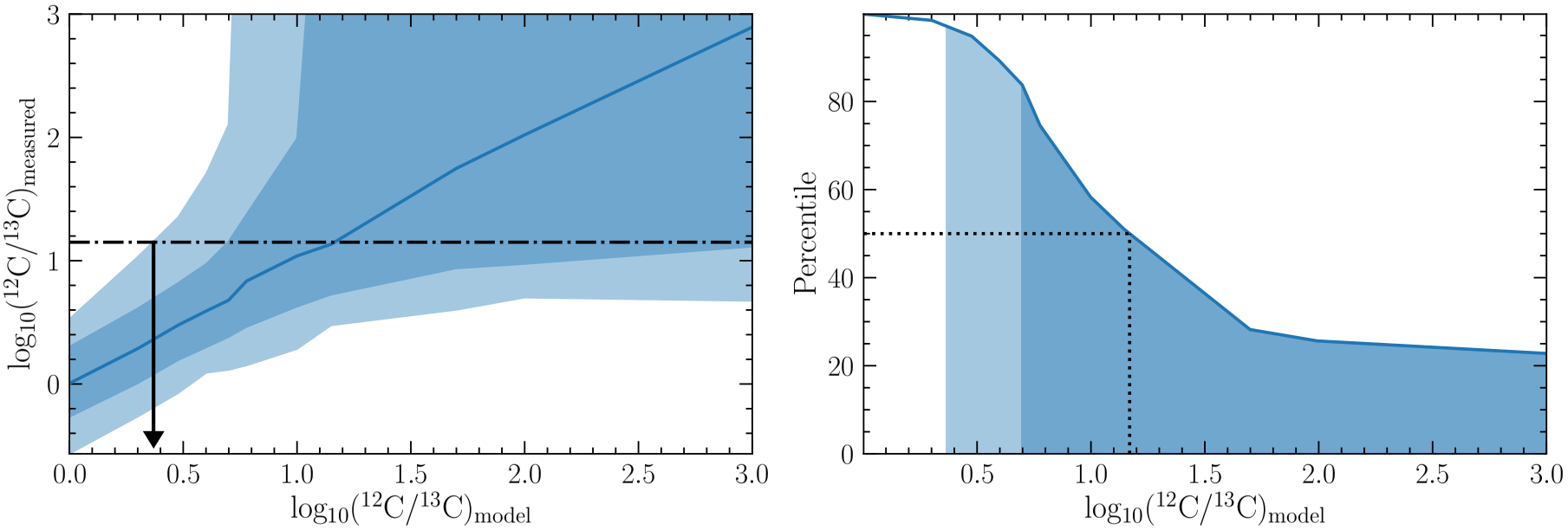

Figure 4.2. Monte Carlo simulations of our data used to infer a confidence bound on the amount of ^{13}C in the DLA towards J0035−0918 (left panel). The blue line indicates the median recovered value of the $^{12}C/^{13}C$ ratio given 500 realisations of the absorption feature generated using the model $^{12}C/^{13}C$ ratio indicated by the x-axis. The dark and light blue shaded bands encompass the 1σ and 2σ limits of the distribution, respectively. The horizontal dot-dashed line marks the $^{12}C/^{13}C$ measured in our analysis. The black arrow indicates where this value intersects the 97.5 percentile of the distribution. This corresponds to a 2σ lower limit of $^{12}C/^{13}C > +0.37$. The right panel shows the percentile value as a function of the model (i.e. true) $^{12}C/^{13}C$ isotope ratio given our measured value. The shaded bands have the same meaning as in the left panel. The dotted lines mark the 50^{th} percentile and the corresponding model value.

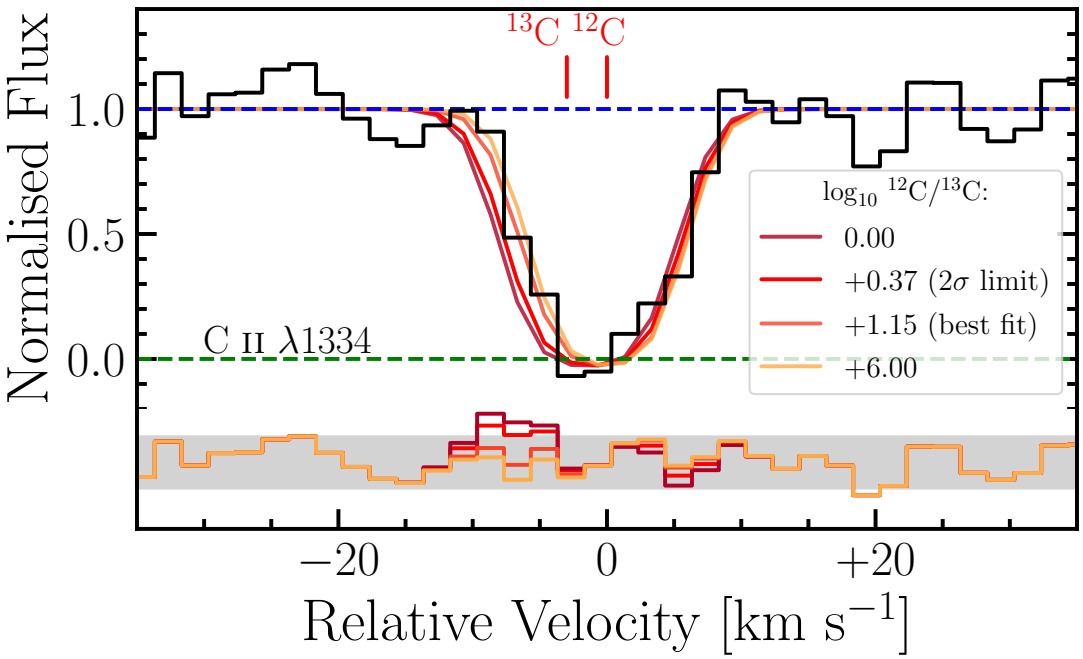

Figure 4.3. ESPRESSO data centred on the C II λ1334 absorption feature shown alongside different model line profiles. Each model curve represents a different ^{12}C/^{13}C abundance ratio (as indicated by the legend) while retaining a constant total carbon abundance of $\log_{10} N(\mathrm{C_{tot}})/\mathrm{cm}^{-2} = 14.29$. Below the zero-level of these data (green dashed line), we show the residuals of the model fit to the data. The shaded band encompasses the 2σ deviations of these model profiles, illustrating that we can rule out $\log_{10}$ ^{12}C/^{13}C $\leq +0.37$ with 95 per cent confidence.

Table 4.2. Relative abundances of the elements detected in the DLA towards J0035−0918 alongside their solar abundances as determined by Asplund et al. (2009).

X	[X/H]	[X/Fe]	[X/O]	$X_\odot$
C	−2.57 ± 0.14	+0.32 ± 0.13	−0.12 ± 0.14	8.43
N	−2.89 ± 0.06	0.00 ± 0.05	−0.44 ± 0.06	7.83
O	−2.45 ± 0.06	+0.44 ± 0.06	...	8.69
Mg	−3.10 ± 0.14	−0.21 ± 0.13	−0.65 ± 0.14	7.56
Al	−3.13 ± 0.06	−0.24 ± 0.05	−0.68 ± 0.06	6.44
Si	−2.59 ± 0.06	+0.30 ± 0.05	−0.14 ± 0.06	7.51
Fe	−2.89 ± 0.05	...	−0.44 ± 0.06	7.47

isotope ratios once $\log_{10} {}^{12}C/{}^{13}C > +1.10$. However, we expect with higher S/N data, the threshold for a detection would extend to larger isotope ratios.

This is the first limit on the carbon isotope ratio in a near-pristine absorption system. With these data we can empirically rule out the presence of large amounts of ^{13}C relative to ^{12}C in the DLA towards J0035−0918. The implications of this abundance ratio for the chemical enrichment of this DLA will be discussed in Section 4.4. The relative abundances of the detected metals are provided for convenience in Table 4.2. We note that with the latest data, [C/Fe] = +0.32 ± 0.13. While consistent with the previous determinations by Carswell et al. (2012); Dutta et al. (2014) and Cooke et al. (2015), this indicates that the DLA towards J0035−0918 is not as abundant in carbon as previously thought, owing to the unusual quiescence of the gas cloud whose broadening is dominated by the thermal motions. However, this system still exhibits an unusually high [N/O] ratio, compared with the typical very metal-poor DLA population (Cooke et al., 2011b). The [N/O] abundance of this DLA places it just above the primary N plateau (Pettini et al., 2008; Petitjean et al., 2008; Zafar et al., 2014). Furthermore, the [Mg/Si], [Mg/O], and [Mg/Fe] ratios are remarkably subsolar, quite unlike the ratios that are seen in extremely metal-poor halo stars of the Milky Way (e.g. Andrievsky et al. 2010).

4.4 Analysis

Given our robust determination of the chemical abundance pattern of the DLA towards J0035−0918, we now investigate the enrichment history of this system. Our lower bound on the $^{12}C/^{13}C$ isotope ratio indicates that there is at least 2.3 times more ^{12}C than ^{13}C in this DLA; this does not empirically rule out enrichment from low mass Population III stars. To test whether the chemical signature of this system is better modelled by Population III or Population II enrichment, we can exploit the stochastic chemical enrichment model developed by Welsh et al. (2019), alongside the yields from simulations of stellar evolution. The resulting enrichment models can be used to infer the epoch at which this DLA formed its enriching stars as well as its total stellar mass and total gas mass. In addition to investigating the physical and chemical properties of the DLA towards J0035−0918, given the simplicity of the absorption line profiles and the reliable wavelength solution delivered by ESPRESSO, we can also use these data to test the invariance of the fine-structure constant.

4.4.1 Stochastic enrichment model

In previous work (Welsh et al., 2019), we developed a stochastic chemical enrichment model that uses the abundance patterns of near-pristine environments to infer their chemical enrichment history. This model describes the initial mass function (IMF) of an enriching stellar population as a power law, governed by the slope, α. The normalisation of this power law, k, is set by the number of stars, $N_\star$, that form within a given mass range:

$$N_\star = \int_{M_{\rm min}}^{M_{\rm max}} k M^{-\alpha} dM \ . \tag{4.4.1}$$

For reference, a Salpeter IMF corresponds to $\alpha = 2.35$ (Salpeter, 1955). For a given enrichment model, we then stochastically sample the IMF and, using the yields from simulations of stellar evolution, determine the distribution of chemical abundances we expect to see across an enriched population of objects. These distributions can then be

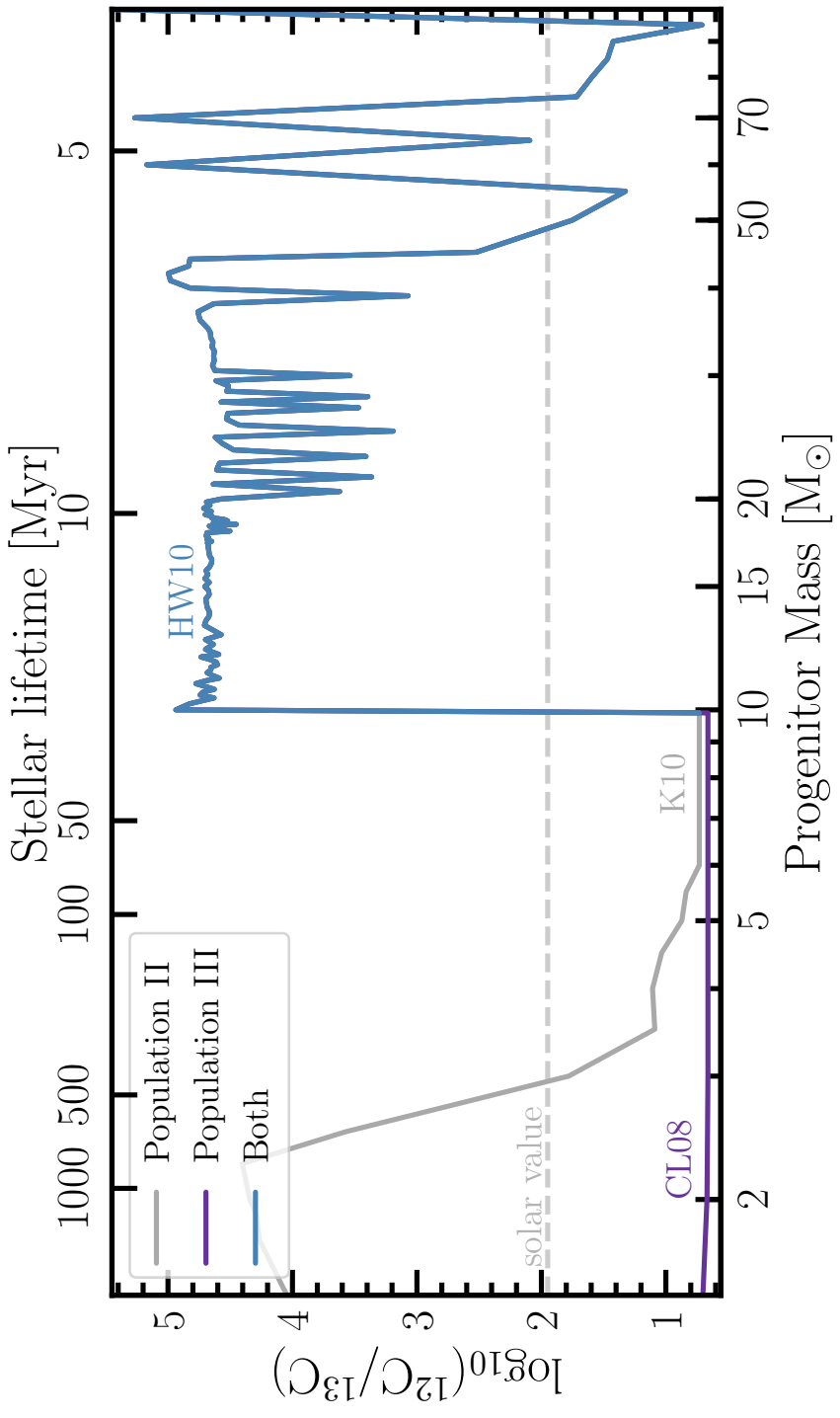

Figure 4.4. $^{12}C/^{13}C$ yield as a function of progenitor mass for both Population III and Population II stars. The yields of low mass Population III stars are from CL08 while those of Population II stars are from K10. The yields of massive Population III and Population II stars are given by HW10. We have only included the yields of stars whose lifetimes are shorter than the age of the Universe at $z = 2.34$ (i.e. those with $M > 1.46\,M_\odot$). The stellar lifetimes are indicated by the top x-axis (Woosley et al. 2002, Karakas 2014). The horizontal grey dashed line indicates the solar C isotope ratio, $^{12}C/^{13}C = 89$ (Asplund et al., 2009).

used to gauge the likelihood of measuring our observed abundances given any underlying enrichment model. This approach assumes that the gas within the DLA is well-mixed and that the system experiences no inflow or outflow of gas; for further details of this model, see Welsh et al. (2019).

The stellar yields used in this analysis are from three sources: (1) Campbell & Lattanzio (2008), hereafter CL08, who simulate the evolution of low mass metal-free stars in the mass range $(1 - 3)$ $M_{\odot}$; (2) Karakas (2010), hereafter K10, who simulate the evolution of very metal-poor AGB stars ($Z \sim 0.005 Z_{\odot}$) in the mass range $(1 - 6)$ $M_{\odot}$; and, (3) Heger & Woosley (2010), hereafter HW10, who simulate the evolution and core-collapse supernovae (CCSNe) of massive (> 10 $M_{\odot}$) metal-free stars. Throughout this work, we use the combined yields of CL08 and HW10 to define the yields of Population III stars. In lieu of simulations that calculate the $^{12}C/^{13}C$ ratio for intermediate mass Population III stars, we have chosen to extrapolate the yields of CL08 to meet the yields of HW10.

While the HW10 yields have been calculated for metal-free stars, they are also indicative of Population II CCSNe yields; this can be seen by comparison with the Woosley & Weaver (1995) yields of metal-enriched massive stars (at least for the elements under consideration in this work). We therefore define Population II yields as the combined yields of K10 and HW10. We necessarily implement another yield extrapolation to bridge the gap between the K10 and HW10 yields. Although this extrapolation is not ideal, this is the best option available to us until a more complete set of yields becomes available. K10 report stellar yields covering a range of metallicities, spanning $0.0001 < Z < 0.02$. We choose Population II yields with an initial metallicity $Z = 0.0001$. We note that the HW10 yields have been calculated as a function of the progenitor star mass, the explosion energy of their supernova, and the mixing between the different stellar layers. When considering these yields, we have adopted the recommended prescription for mixing between stellar layers, defined to be 10 per cent of the helium core size. For the explosion energy, we adopt $E_{\rm exp} = 1.8 \times 10^{51}$ erg. This is a measure of the final kinetic energy of the ejecta at infinity and is consistent with the typical value found by Welsh et al. (2019) when investigating the properties of the stars that enrich the most metal-poor DLAs. Figure 4.4 shows the resulting $^{12}C/^{13}C$ yields of

these stellar populations as a function of both their progenitor mass and stellar lifetime. From Figure 4.4 we can see that it is the low mass Population III stars, and the intermediate mass Population II stars, that are capable of producing comparable amounts of the carbon isotopes (i.e. $^{12}C/^{13}C \simeq 1$). Generally, it is surface mixing events that facilitate the production of ^{13}C. AGB (both Population II and Population III) stars produce ^{13}C through a process known as hot bottom burning (HBB). This process involves the convection induced transport of ^{12}C from the burning shell to the proton-rich envelope where ^{13}C can then be synthesised via proton-capture (Iben, 1975; Prantzos et al., 1996). HBB is dependent on both the mass and metallicity of the progenitor stars. For a star to undergo HBB, the convective envelope must reach a sufficiently high temperature. The transition seen at $\sim 10\ M_\odot$ between the yields of massive stars and those of lower mass stars originates because massive stars do not show signs of these surface mixing events (Karakas & Lattanzio, 2014); they are only capable of producing ^{13}C through secondary processes. Using our enrichment model with these yields, we can investigate the chemical enrichment of the DLA towards J0035−0918 under the assumption of either Population II or Population III enrichment. We use the relative abundances of [C/O], [Si/O], and [Fe/O] as given in Table 4.2, alongside the lower limit on $^{12}C/^{13}C$ from Table 4.1 to evaluate the likelihood of a given model. We choose to model only these abundance ratios because our stochastic chemical enrichment model is computationally expensive. We therefore focus our attention on the most abundant elements that are relatively well-modelled by stellar evolution. We use the EMCEE Markov Chain Monte Carlo (MCMC) sampler (Foreman-Mackey et al., 2013) to determine the enrichment model parameters that provide the best fit to these data. The model parameters that we consider are those defined by Equation 4.4.1 ($\alpha, N_\star, M_{\rm min}, M_{\rm max}$). We impose uniform priors on these parameters, limited by the boundary conditions:

$$
\begin{aligned}
0 \leq \quad & \log_{10} N_\star & \leq 5\ , \\
1.46 \leq \quad & M_{\rm min}/M_\odot & \leq 11\ , \\
20 \leq \quad & M_{\rm max}/M_\odot & \leq 70\ , \\
-8 \leq \quad & \alpha & \leq 8\ .
\end{aligned}
$$

Since the *number* of stars contributing to the enrichment of the DLA, $N_\star$, could be quite large in the case of a low value of $M_{\rm min}$, we choose to sample $\log_{10}$ N$_\star$; this allows us to stochastically sample the IMF at high masses (a regime we suspect may be dominated by just a few massive stars), while still allowing for a much larger number of low mass stars. The minimum mass of the enriching stars is set by considering the age of the Universe at the redshift of the DLA. Using the latest Planck Collaboration et al. (2018) cosmology, where $H_0 = 67.4 \pm 0.5$ km s^{-1}Mpc^{-1} and $\Omega_{\rm m} = 0.315 \pm 0.007$, we find that the age of the Universe is 2.792 Gyr at the redshift of this absorption system (recall $z_{\rm abs} = 2.34006$). Given that the first stars are thought to have formed between $z \sim 15 - 20$, there is a finite time in which stars can contribute to the enrichment of this system. Using the stellar lifetimes from Karakas (2014), we find that stars with masses $\lesssim 1.46$ M$_\odot$ live longer than the age of the Universe at redshift $z \simeq 2.34$. Therefore we only expect to see the chemical signature of stars with masses above this limit in the chemistry of this near-pristine DLA. The upper limit of the mass of the enriching stars marks the transition from CCSNe to pulsational pair instability SNe, as found by Woosley (2017).

During our MCMC analysis, we utilise the chains of 400 randomly initialised walkers to determine the posterior distributions of our enrichment model parameters. After adopting a burn-in that is half the original length of the chains, we find the posterior distributions shown in Figure 4.5. We found that these distributions are invariant once the walkers have each taken 2100 steps. From this figure, we see that the maximum likelihood enrichment model parameters are almost unchanged by the assumption of Population II versus Population III enrichment. Both enrichment histories suggest an IMF slope that is preferably steeper than, but still consistent with, a Salpeter distribution, $\alpha = 3.6^{+3.7}_{-2.0}$ (Population II) $\alpha = 3.8^{+3.6}_{-2.0}$ (Population III), where the quoted errors encompass 95 per cent of the parameter distributions. We have repeated our analysis under the assumption of a Salpeter-like IMF slope and found that introducing this prior has a negligible impact on the resulting distributions.

Our analysis suggests that this DLA has been enriched by at least 10 stars, with maximum likelihood values of $\log_{10} N_\star = 2.3^{+2.5}_{-1.4}$ (Population II) and $\log_{10} N_\star = 2.5^{+2.3}_{-1.7}$ (Population

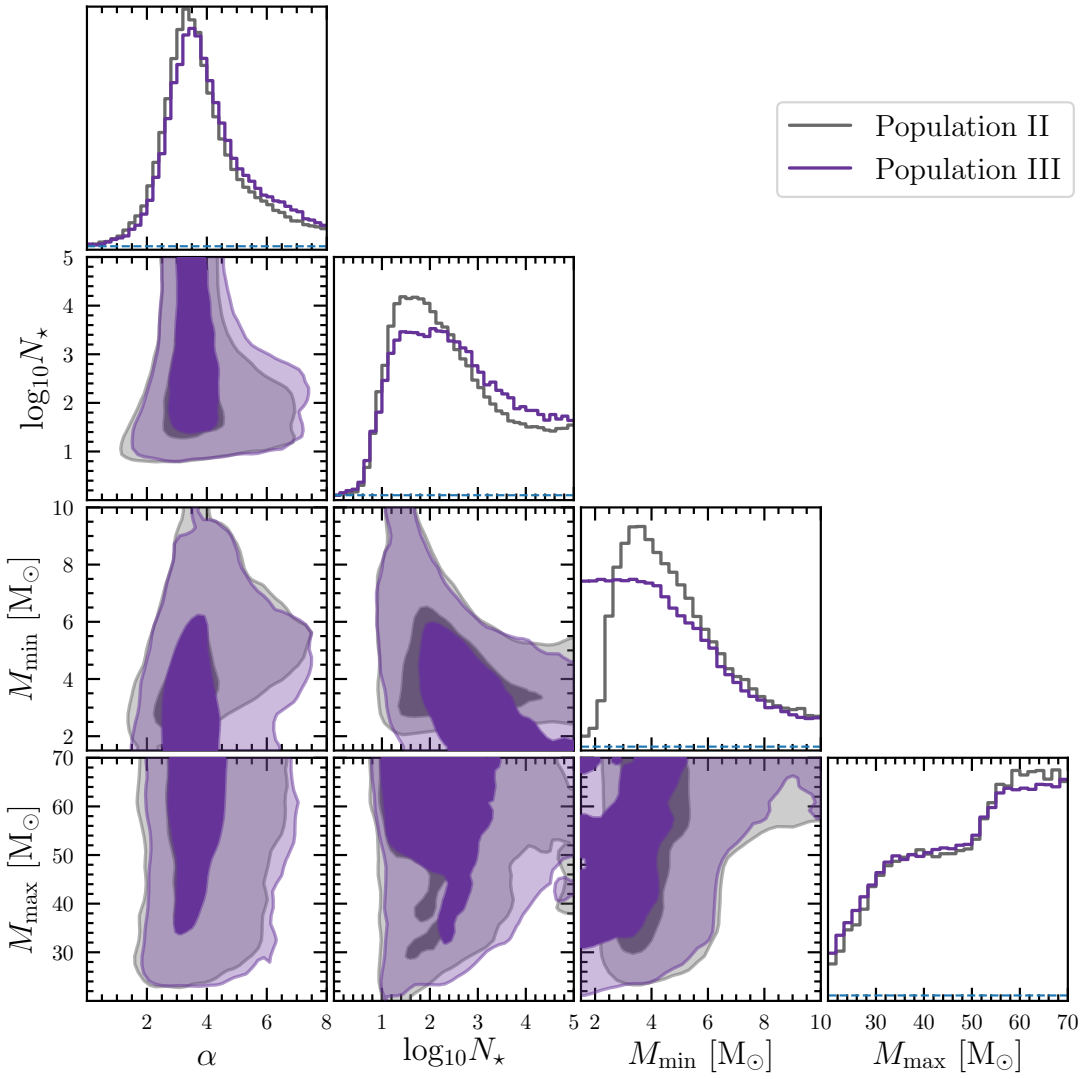

Figure 4.5. Results of our MCMC analysis of the chemical enrichment of the DLA towards J0035−0918. The diagonal panels indicate the maximum likelihood posterior distributions of our enrichment model parameters while the 2D contours indicate the correlation between these parameters. Our Population II model is shown in grey. Overplotted in purple is the result of considering Population III stars as the dominant source of enrichment. In the diagonal panels, the horizontal blue dashed line indicates the zero-level of each distribution.

III). In each enrichment scenario, $M_{\rm max}$ is unconstrained, with both distributions showing a slight preference towards a larger maximum enriching mass. We find the only parameter estimate that varies significantly between these enrichment histories is that of the minimum enriching mass, $M_{\rm min}$. Under the assumption of Population II enrichment, the data disfavour enrichment from low mass (< 2.4 M$_\odot$) stars. While, if this is a Population III enriched system, enrichment from low mass stars is preferable. This is likely being driven by the divergent yields of [C/O] across the stellar populations. From the simulations of stellar evolution, we see that the lowest mass Population II stars produce supersolar [C/O] relative to our measured value ([C/O] $= -0.12 \pm 0.14$), while the lowest mass Population III stars produce subsolar yields of [C/O]. Given that our maximum likelihood enrichment model is consistent with a well-sampled IMF, to investigate this divergence further, we can calculate the IMF weighted abundance of [C/O] for both Population II and Population III enrichment. These calculations show that, given our maximum likelihood estimate of α, when $M_{\rm min} < 2.4$ M$_\odot$ the C-rich yields of the lowest mass Population II stars result in supersolar [C/O]. These yields are hard to reconcile with our measured value.

Given current data, we are only able to utilise the ^{12}C/^{13}C lower bound to constrain our enrichment model. This lower bound does little to drive the results of our current analysis. However, as can be seen from Figure 4.4, the C isotope ratio is also divergent at low masses for the different stellar populations. Therefore, a precise measurement of the ^{12}C/^{13}C ratio, in combination with the [C/O] abundance, would enable us to distinguish more clearly whether the DLA towards J0035−0918 shows the signature of Population III versus Population II enrichment. We also note that there are some extremely metal-poor, rapidly-rotating stars, with masses > 7 M$_\odot$, that are capable of producing $4 <^{12}$C/^{13}C< 77 (Meynet et al., 2010). These stars, that have metallicities between $Z = 5 \times 10^{-7}$ Z$_\odot$ and $Z = 5 \times 10^{-4}$ Z$_\odot$, are capable of producing an enhancement of alpha elements, akin to that observed in the most iron-poor stars of the Milky Way halo. At present, our limit on ^{12}C/^{13}C is not able to rule out rapidly-rotating extremely metal-poor stars as a potential source of the enrichment of this near-pristine DLA. However, future higher S/N observations of J0035−0918 will be able to test this possibility.

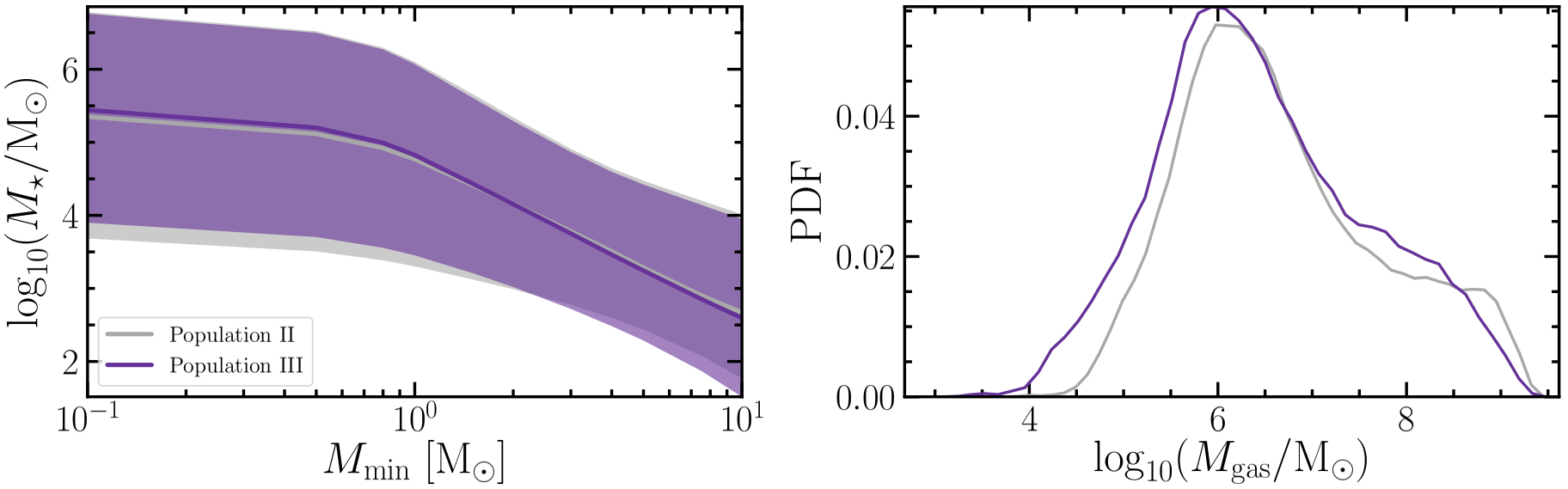

Figure 4.6. Left: The total inferred stellar mass of the DLA towards J0035−0918 as a function of the minimum mass with which stars can form. The purple solid curve indicates the median value given our Population III enrichment model and the shaded region encompasses the 16$^{\mathrm{th}}$ and 84$^{\mathrm{th}}$ percentiles. The grey curves have the same meaning, but are based on our Population II enrichment model. Right: The total gas mass of the DLA towards J0035−0918 inferred from our enrichment models combined with the measured [O/H] abundance ([O/H]= −2.45), assuming 100 per cent metal retention (see text for further details).

4.4.2 Physical and chemical properties

Using the results of our enrichment model analysis, we can infer some of the physical and chemical properties of the DLA towards J0035−0918, such as the total stellar mass and the total gas mass of the system. To calculate the total stellar mass, we use the inferred model parameter distributions and integrate over the IMF, weighted by mass (cf. Equation 4.4.1). For stars above 1 $M_\odot$, we adopt a power law IMF, while for stars $<$ 1 $M_\odot$, we adopt the IMF as described by Chabrier (2003). This results in the stellar mass distribution as shown in the left panel of Figure 4.6. We find that the total stellar mass ($\geq$ 1 $M_\odot$) of this DLA is $\log_{10}(M_\star/M_\odot) = 4.8 \pm 1.3$. We can also infer the total gas mass of the DLA using our enrichment model, as follows. Assuming that the DLA towards J0035−0918 has retained 100 per cent of the metals produced *in-situ*, we can calculate the total gas mass required to produce the observed metal abundance. For this calculation we use the observed [O/H] abundance as a proxy of the metal abundance. The resulting distribution is shown in the right panel of Figure 4.6. If this is a Population III enriched system, to achieve the measured abundance [O/H] = -2.45 ± 0.06, we would require a total gas mass $\log_{10}(M_{\rm gas}/M_\odot) = 6.3^{+1.4}_{-0.9}$. If, in fact, some metals were not retained by the DLA, the observed [O/H] abundance could be achieved through metals mixing with a smaller reservoir of hydrogen. In this case, our inference would correspond to an upper limit of the total gas mass. We find that our inferences of the stellar and gas mass of this DLA are consistent (i.e. within 1σ) of the corresponding values quoted by Welsh et al. (2019) for typical very metal-poor DLAs.

4.4.3 Enrichment timescale: Evidence of reionization quenching?

Our constraints on the minimum mass of the enriching stars can be used to estimate the epoch when the DLA experienced most of its star formation. Using the stellar lifetimes from Woosley et al. (2002) and Karakas (2014) as well as the posterior distribution of $M_{\rm min}$ (see the histogram on the third row of Figure 4.5), we can convert the $M_{\rm min}$ distribution to a distribution of enrichment timescales. The results of this transformation for both

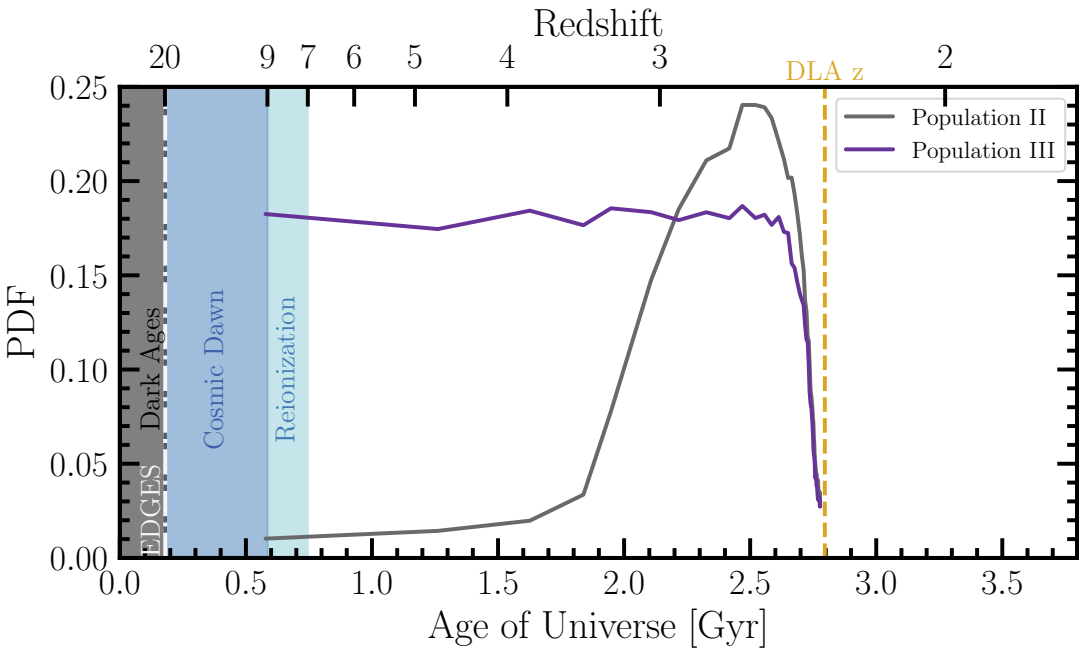

Figure 4.7. The most likely epoch of star formation experienced by the DLA towards J0035−0918 given our maximum likelihood enrichment model. The purple (Population III) and grey (Population II) curves indicates the probability that the stars which chemically enriched this system were born at a given redshift. A high value of the PDF indicates the most likely redshift that the DLA experienced a burst of star formation (or, equivalently, the epoch when most of the enriching stars were formed). We highlight the epoch of reionization as determined by the Planck Collaboration et al. (2018) with a light-blue shaded band. Similarly, the period known as the Cosmic Dawn is shown in dark blue. Between this epoch and the Dark Ages (black shaded band) is the recent EDGES detection (vertical white dot-dashed line) from Bowman et al. (2018).

Population II and Population III stars are shown in Figure 4.7. Since our analysis disfavours a large ($\sim$ 8 $M_{\odot}$) minimum enriching mass, the sharp fall of these distributions as we approach the redshift of the DLA suggests that the majority of star formation must have ended prior to this epoch. We can see from this figure that if Population II stars are the predominant enrichers, then the DLA must have had a burst of star formation just a few hundred Myr before we observe the DLA today. Such a timescale is relatively short given that the DLA would need to have recovered quickly from the putative supernova feedback in order to be observed at $z = 2.34$ with a significant quantity of neutral gas and apparently no turbulence. Hydrodynamic models of the enrichment of ultra-faint dwarf (UFD) galaxies (Webster et al., 2015a) indicate that the chemistry of these systems requires periods of extended star formation, which may also be required to explain the enrichment of this DLA (see also, Webster et al. 2015b).

In this DLA, however, we find no evidence of enrichment by low mass Population II stars. As shown in Figure 4.7 by the grey curve, the most likely explanation in this scenario is that the DLA experienced no significant star formation post-reionization, for at least $\gtrsim$ 1 Gyr. There are several mechanisms that can temporarily quench a low mass galaxy. One such possibility is reionization quenching (e.g. Bullock et al. 2000) due to the cosmic reionization of hydrogen at $z \simeq 8$ (Planck Collaboration et al. 2018; light blue band in Figure 4.7). Reionization played two critical roles that affected star formation in low mass galaxies. First, reionization heated up the intergalactic medium, thereby limiting the accretion of gas onto low mass galaxies. This starved low mass galaxies of the gas supply needed to form stars. Moreover, reionization heated up the interstellar medium of low mass galaxies, bringing a halt to any ongoing star formation.

The main thrust of current observational efforts to study the reionization quenching of low mass galaxies utilise deep observations of the lowest mass UFD galaxies orbiting the Milky Way (Weisz et al., 2012; Brown et al., 2014; Weisz et al., 2014). These studies use color magnitude diagrams to reconstruct the star formation histories of the UFD galaxies. This technique allows us to study the present properties of UFD galaxies in detail, but currently suffers from poor time resolution at $z \gtrsim 2$. Therefore it is difficult to study the

finer details of the reionization quenching process, such as the duration of the quenching and the properties of the gas that survives reionization. Simulations of low mass galaxy formation (e.g. Wheeler et al. 2015; Oñorbe et al. 2015) indicate that reionization can bring a halt to star formation for $\sim$ 1 Gyr; furthermore, these simulations indicate that some low mass galaxies are able to retain a small reservoir of gas for future star formation. Some of these quenched dwarf galaxies may re-ignite their star formation through interactions with gaseous streams in the intergalactic medium (Wright et al., 2019).

Studying the chemical enrichment of the most metal-poor DLAs may therefore offer a novel and exciting opportunity to study reionization quenching in detail by using certain chemical tracers as a 'chemical clock'. Taken at face value, our observations combined with our stochastic chemical enrichment model tentatively suggest that star formation in the DLA towards J0035−0918 may have experienced a $\sim$ 1 Gyr hiatus. In principle, one might be able to tease out the signature of reionization quenching by studying a sample of metal-poor DLAs; reionization is a cosmic event that comparably affects all galaxies at a given mass scale. This signature may be encoded in the star formation histories (and therefore chemistry) of the most metal-poor DLAs. One prediction of this scenario is that the most metal-poor DLAs should exhibit a general increase of their [C/O] at redshift $z \sim 3$; oxygen is primarily produced by massive stars on short timescales, while carbon is produced by massive stars as well as low and intermediate mass stars on longer timescales (Akerman et al., 2004; Cescutti et al., 2009; Romano et al., 2010). Thus, an increase of [C/O] at low redshift would mark the yields of the first low and intermediate mass Population II stars to have formed post-reionization. We may be witnessing the first tentative evidence of this effect in Figure 4.8 where we plot the [C/O] abundances of the *most* metal-poor DLAs currently known as a function of their redshift. These data are based on the list compiled by Cooke et al. (2017) who investigated the chemical evolution of DLAs with [O/H]< -1.75. We consider only those with $\log_{10} N(\mathrm{H\,I})/\mathrm{cm}^{-2} > 20.3$ that have also been observed with a high resolution (R $> 30,000$) spectrograph. Figure 4.8 shows tentative evidence that some near-pristine DLAs display slightly elevated [C/O] at lower redshift. We note that the size of the errors associated with each system is due to the

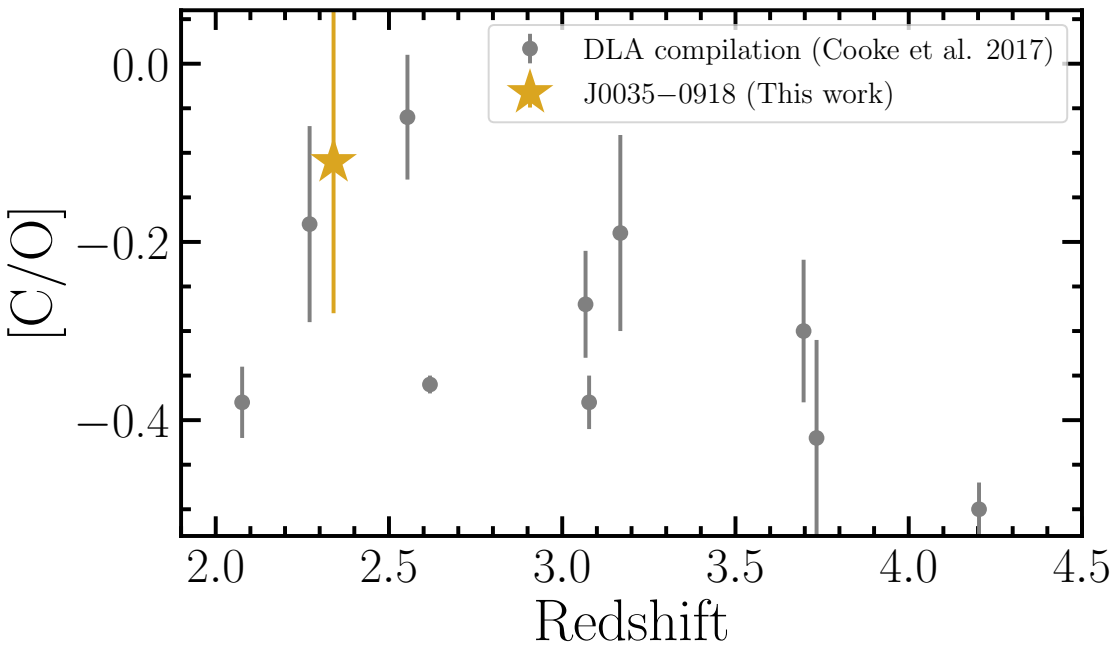

Figure 4.8. The redshift evolution of the measured [C/O] ratio of near-pristine DLAs. These systems are all bona fide DLAs (i.e. $\log_{10} N(\mathrm{H\,I})/\mathrm{cm}^{-2} > 20.3$) with metallicity [O/H]$< -1.75$ that have been observed with a high resolution ($R > 30,000$) echelle spectrograph. The potential upward trend in [C/O] at lower redshift is supported by the [C/O] determination of J0035−0918.

relative saturation of the lines used to determine the abundance ratio.

4.4.4 Fine-structure constant

Given the quiescence and intrinsically simple cloud structure of the DLA towards J0035−0918, in combination with the wavelength stability of ESPRESSO, we have an ideal dataset for placing a bound on the invariance of the fine-structure constant α at high redshift. Given that this DLA is a near-pristine environment which is presumably living in a relatively underdense part of the Universe compared to other absorption line systems, it also offers an alternative environment to test the invariance of the fundamental couplings. Astrophysical determinations of the variability of the fine-structure constant,

$$\alpha \equiv e^2/4\pi\epsilon_0\hbar c \approx 1/137\,, \tag{4.4.2}$$

which characterises the strength of the electromagnetic force, has been the subject of many investigations since the advent of the 10 m class telescopes. The general principle is to measure the change of the fine-structure constant measured today (α_0) relative to a measurement at high redshift (α_z), leading to a bound of the form:

$$\Delta\alpha/\alpha \equiv (\alpha_z - \alpha_0)/\alpha_0 \tag{4.4.3}$$

To obtain a measure of α_z, the observed wavelengths of several spectral lines need to be measured very accurately, as each absorption line exhibits a different sensitivity to α. This sensitivity can be parameterised by a change to the wavenumber of a given transition at high redshift, ω_z, relative to the same value measured in the laboratory today, ω_0:

$$\omega_z = \omega_0 + q\,x \tag{4.4.4}$$

where q is the sensitivity coefficient which determines how sensitive a given transition is to changes in α, and $x = (1 + \Delta\alpha/\alpha)^2 - 1$. In this work, we use the q-coefficients compiled by Berengut et al. (2011) and Murphy & Berengut (2014).

For this test, we use only the ESPRESSO data and include the absorption lines of O I λ1302, Al II λ1670, Si II λ1536, Fe II λ1608, and Fe II λ2344, which exhibit sensitivity coefficients in the range $-1165 \leq q/\mathrm{cm}^{-1} \leq 1375$. The ALIS line-fitting code that we use in our analysis includes $\Delta\alpha/\alpha$ as an optional extra parameter in the line fitting process. Specifically, ALIS reads in the atomic data (q and ω_0) of each transition, and calculates the observed wavelengths given the two model parameters (redshift and $\Delta\alpha/\alpha$). We can therefore constrain both $\Delta\alpha/\alpha$ and z simultaneously when optimising the model profiles of the ESPRESSO data. Based on just the one absorption line system that we report here, we infer a bound on the invariance of the fine-structure constant, $\Delta\alpha/\alpha = (-1.2 \pm 1.1) \times 10^{-5}$. Given the relatively low S/N of our data owing to the faint background quasar and short integration time, this bound is impressively tight, falling just a factor of ~ 8 short of the precision achieved by Kotuš et al. (2017), who reported the most precise measurement from any single absorber to date. In addition, the simplicity and quiescence of the cloud structure provides us with confidence that the modelling of the line profile has not

introduced unaccounted for systematic uncertainties. We refer the reader to Murphy & Cooksey (2017) for a discussion of possible sources of uncertainty and a compilation of the most reliable results to date. This is the first result that we are aware of that demonstrates the superior wavelength accuracy delivered by the ESPRESSO instrument in 4UT mode.

4.5 Conclusions

We report the first bound on the $^{12}C/^{13}C$ abundance ratio of a near-pristine environment using science verification data acquired with ESPRESSO in 4UT mode. Our main conclusions are as follows:

(i) We have demonstrated that the wavelength accuracy afforded by ESPRESSO permits a limit on the $^{12}C/^{13}C$ isotope ratio in the quiescent DLA towards J0035−0918 using the C II λ1334 absorption line. A significant quantity of ^{13}C, if found, could be a signature of low mass metal-free star formation.

(ii) We find that the gas cloud is well-modelled by a single absorption component whose broadening is entirely dominated by the thermal motions of the gas. On the basis of this model, we report a conservative 2σ lower limit $\log_{10} {}^{12}C/^{13}C > +0.37$. We therefore conclude that this DLA predominantly contains ^{12}C. Given this 2σ limit, we are unable to confidently rule out the presence of low mass Population III stars at this stage.

(iii) We developed a stochastic chemical enrichment model to test whether the chemistry of this system is better modelled by Population III or Population II enrichment. We have found, given current data, that both scenarios are plausible and are equally capable of producing the observed abundances of $^{12}C/^{13}C$, [C/O], [Si/O], and [Fe/O].

(iv) Based on our best-fitting enrichment model, we estimate the DLA contains a stellar mass of $\log_{10}(M_\star/M_\odot) = 4.8 \pm 1.3$ and a gas mass of $\log_{10}(M_{\rm gas}/M_\odot) = 6.3^{+1.4}_{-0.9}$.

(v) We report tentative evidence that the *most* metal-poor DLA population exhibits somewhat higher [C/O] values at redshift $z \lesssim 3$. The elevated [C/O] ratios at $z \lesssim 3$ might be a signature of enrichment from the first metal-enriched low and intermediate mass stars.

(vi) Our enrichment model also suggests that — if this gas cloud is predominantly enriched by Population II stars — the bulk of the metals were produced just a few hundred Myr before the time that we observe the DLA. Prior to that, star formation in this DLA appears to have experienced a period of quiescence. We propose that this quiescence may have been caused by the cosmic reionization of hydrogen, but this can only be confirmed with future observations of near-pristine DLAs covering the redshift interval $z \simeq 2 - 4$.

(vii) We use the simplicity of the absorption profile of this system to investigate whether there is a detectable spatial or temporal variation of the fine-structure constant. When including $\Delta\alpha/\alpha$ as a free parameter in our line-fitting procedure, we find $\Delta\alpha/\alpha = (-1.2 \pm 1.1) \times 10^{-5}$.

Our work demonstrates the wealth of information made available through studying the chemistry of near-pristine absorption systems. The detailed abundance patterns of the most metal-poor DLAs provide insight into the earliest episodes of chemical enrichment. Indeed, this first bound on the C isotope ratio in a near-pristine environment has ruled out the presence of strong ^{13}C in this DLA; with data of S/N=20, we could observationally rule out significant enrichment by low mass Population III stars in this near-pristine environment. A similar study across the metal-poor DLA population would determine whether these systems typically show signatures of Population II or Population III enrichment. From these reconstructed enrichment histories, we may find observational evidence of reionization quenching at $2 < z < 4$ (within the redshift interval where these absorption systems are most easily studied), and be able to study the physical properties (e.g. density, temperature) of the gas affected by reionization quenching. Thanks to ESPRESSO, studies of this nature are now within the realm of possibility.

CHAPTER 5

Oxygen and iron in extremely metal-poor DLAs

The following chapter is from a paper in preparation entitled "Oxygen and iron in extremely metal-poor DLAs". Similar to the previous chapter, we present high resolution echelle data for two near-pristine DLAs. The new data were collected with either VLT/UVES (PI: L. Welsh) or Keck I/HIRES (PI: M. Pettini). These data were reduced by the respective investigators of the programmes, while the subsequent analysis was led by the thesis author. We use these data to precisely pin down the [O/Fe] abundances of these DLAs. We go on to assess the relationship between [O/Fe] and [Fe/H] across the metal-poor DLA population. For VMP DLAs with $-3 <$ [Fe/H] < -2, the [O/Fe] is consistent with a plateau at $[\langle \mathrm{O/Fe} \rangle] = +0.40 \pm 0.08$. Below [Fe/H] < -3, DLAs show an elevated [O/Fe] ratio. The DLAs presented in this work are consistent with this trend. The plateau suggests that the VMP DLAs are enriched by a similar population of stars, drawn from the same IMF. If confirmed, this change in chemistry below [Fe/H] < -3 would be an empirical indication that the *most* metal-poor DLAs show a diverging chemical enrichment history. Indeed, the elevated [O/Fe] abundance may be a sign of enrichment from Population III stars.

Abstract: We present precise abundance determinations of two near-pristine damped Lyman-α systems (DLAs) to assess the nature of the [O/Fe] ratio at [Fe/H] < -3.0 (i.e. $< 1/1000$ of the solar metallicity). Prior observations indicate that the [O/Fe] ratio is consistent with a constant value, [O/Fe] $\simeq +0.4$, when $-3 <$ [Fe/H] < -2, but this ratio may increase when [Fe/H] $\lesssim -3$. In this paper, we test this picture by reporting two precise [O/Fe] abundances in some of the most metal-poor DLAs currently known. We derive values of [O/Fe] $= +0.50 \pm 0.10$ and [O/Fe] $= +0.62 \pm 0.05$ for these two $z \simeq 3$ near-pristine gas clouds. These results strengthen the idea that the [O/Fe] abundances of the most metal-poor DLAs are elevated compared to DLAs with [Fe/H] $\gtrsim -3$. We suggest this distinct abundance pattern may be a signpost of enrichment by the first generation of stars. We compare the observed abundance pattern of this DLA to the nucleosynthetic yields of Population III supernovae (SNe). The chemistry of this DLA can be well described by a $(17 - 27)$ $M_\odot$ Population III SN that underwent a $(1.6 - 2.4) \times 10^{51}$ erg explosion. Precise abundance determinations of additional EMP DLAs are necessary to confirm the behaviour of [O/Fe] at the lowest metallicities.

5.1 Introduction

The first stars in the Universe are responsible for producing the first chemical elements heavier than lithium. These elements — known as metals — irrevocably changed the process of all subsequent star formation and mark the onset of complex chemical evolution within our Universe. Since no metal-free stars have been detected, we know very little about their properties (e.g. their mass distribution) and the relative quantities of the metals that they produced. When the first stars ended their lives, some as supernovae (SNe), they released the first metals into their surrounding environment. The stars that formed in the wake of these (Population III) SNe were thus born with the chemical fingerprint of the first stars. By studying the chemistry of these relic objects, we can investigate the metals produced by the first stars and, ultimately, trace the evolution of metals across cosmic time. Historically, the fingerprints of the first stars have been studied in the atmospheres of low

mass, Population II stars that are still alive today (e.g. Cayrel et al. 2004; Frebel et al. 2005; Aoki et al. 2006; Frebel et al. 2015; Ishigaki et al. 2018; Ezzeddine et al. 2019); the composition of the stellar atmosphere is studied in absorption against the light of the star. This process of stellar archaeology, along with simulations of stellar evolution, allows us to infer the elements produced by the first SNe and, subsequently, infer their properties (such as mass, rotation rate, and explosion energy) (Woosley & Weaver, 1995; Chieffi & Limongi, 2004; Meynet et al., 2006; Ekström et al., 2008; Heger & Woosley, 2010; Limongi & Chieffi, 2012).

Extragalactic gas, often seen as absorption along the line-of-sight towards unrelated background quasars, offer a complementary opportunity to study chemical evolution and the first stars (Pettini et al., 2008; Penprase et al., 2010; Becker et al., 2011). The extragalactic gas clouds that have been studied in absorption to date cover a broad range of metallicity, which appears to increase over time (Rafelski et al., 2012, 2014; Jorgenson et al., 2013; Lehner et al., 2016; Quiret et al., 2016; Lehner et al., 2019). Those whose relative iron abundance is $1/1000^{\text{th}}$ of the solar value (i.e. [Fe/H] < -3.0)[1] are classified as extremely metal-poor (EMP). These environments have necessarily experienced minimal processing through stars and are therefore an ideal environment to search for the chemical signature of the first stars.

Among the least polluted environments currently known, there are three absorption line systems at $z \sim 3-4$ that appear to be entirely untouched by the process of star formation, with metallicity limits of [M/H] $\lesssim -4.0$ (Fumagalli et al., 2011; Robert et al., 2019); all three are Lyman limit systems (LLSs) whose neutral hydrogen column density is $16.2 < \log_{10} N(\text{H I})/\text{cm}^{-2} < 19.0$. These pristine LLSs are a rarity. It is more common to detect absorption line systems that are, at least, minimally enriched with metals. For example, there is a LLS at $z = 3.5$ with a metal abundance $Z/Z_\odot = 10^{-3.4\pm0.26}$ whose [C/Si] abundance is consistent with enrichment by either a Population III or Population II star (Crighton et al., 2016). In order to distinguish between these scenarios, additional

[1]Here, and throughout this paper, [X/Y] denotes the logarithmic number abundance ratio of elements X and Y relative to their solar values $\text{X}_\odot$ and $\text{Y}_\odot$, i.e. $[\text{X/Y}] = \log_{10}(N_\text{X}/N_\text{Y}) - \log_{10}(N_\text{X}/N_\text{Y})_\odot$.

metal abundance determinations are required. Distinguishing between the gaseous systems enriched by Population III stars and later stellar populations would allow us to trace the metals produced by the first stars and determine the typical Population III properties. Furthermore, such an investigation will reveal the timescale over which these gas clouds are enriched by subsequent stellar populations.

A prime environment to disentangle these chemical signatures are damped Lyman-α systems (DLAs; $\log_{10} N(\mathrm{H\,I})/\mathrm{cm}^{-2} > 20.3$; see Wolfe et al. 2005 for a review). Indeed, the most metal-poor DLAs may have been exclusively enriched by the first generation of metal-free stars (Erni et al., 2006; Pettini et al., 2008; Penprase et al., 2010; Cooke et al., 2017; Welsh et al., 2019). These high H I column density gas clouds are self-shielded from external radiation. Thus, the constituent metals reside in a single, dominant, ionization state. This negates the need for ionization corrections and leads to reliable gas-phase abundance determinations. These systems are most easily studied in the redshift interval $2 < z < 3$ when the strongest UV metal absorption features are redshifted into the optical wavelength range. Only the most abundant elements are typically observed in EMP DLAs, including the light α-capture elements (C, O, Mg, Si, S), some odd atomic number elements (N, Al), and some iron-peak elements (usually, only Fe). Given that these elements trace various nucleosynthetic sources, these abundant elements are sufficient to understand the properties of the stars that are responsible for the enrichment of EMP DLAs, and tease out the potential fingerprints of the first stars.

Based on the chemical abundances of EMP stars, we have uncovered some signatures of the first stars, including the enhancement of the lighter atomic number elements relative to the heavier atomic number elements. For example, the observed enhancement of carbon relative to iron in EMP stars with a normal abundance of neutron capture elements (i.e. a 'CEMP-no' star) may indicate that these stars contain the metals produced by Population III stars (see Beers & Christlieb 2005 for a review). Reminiscent of this signature in stars, there is tentative evidence of an enhanced [O/Fe] abundance in the most metal-poor DLAs. Specifically, all DLAs with an iron abundance between $-3.0 < [\mathrm{Fe/H}] < -2.0$ are scattered around an [O/Fe] plateau of [O/Fe]$\simeq +0.4$, while those with [Fe/H] < -3.0 exhibit

a modestly elevated [O/Fe] abundance. The plateau in [O/Fe] observed in DLAs with [Fe/H] > -3.0 suggests that the relatively higher metallicity DLAs were all enriched by a similar population of stars, drawn from the same initial mass function (IMF). Since oxygen is predominantly sourced from the supernovae of massive stars, the apparent 'inflection' observed in the EMP regime can be explained by three equally exciting possibilities. Relative to the stars that enriched the DLAs with [Fe/H] > -3.0, the stars that enriched the most metal-poor DLAs were either: (1) Drawn from an IMF that was more bottom-light; (2) ejected less Fe-peak elements; or (3) released less energy during the explosion that ended their life. All three of these alternatives are signatures of enrichment by a generation of metal-free stars (e.g. Heger & Woosley 2010). However, the errors associated with the currently available data are too large to confirm this trend.

In this paper, we present the detailed chemical abundances of two chemically near-pristine DLAs to study the behaviour of [O/Fe] at the lowest metallicities. These DLAs are found along the line-of-sight to the quasars SDSS J095542.12+411655.3 (hereafter J0955+4116) and SDSS J100151.38+034333.9 (hereafter J1001+0343). Previous observations of these quasars have shown that these two gas clouds are among the most metal-poor DLAs currently known. These gas clouds are therefore ideally placed to assess the [O/Fe] inflection in near-pristine environments. This paper is organised as follows. Section 5.2 describes our observations and data reduction. In Section 5.3, we present our data and determine the chemical composition of the two DLAs. We discuss the chemical enrichment histories of these systems in Section 5.4, before drawing overall conclusions and suggesting future work in Section 5.5.

5.2 Observations

The presented data either represent the first high resolution observations of the DLA (as is the case for J0955+4116), or, we have obtained additional high resolution observations that target previously unobserved metal lines (as is the case for J1001+0343).

The DLA identified along the line of sight to the $m_r = 19.38$ quasar, J0955+4116, was

Table 5.1. Journal of observations.

QS0	r (mag)	z_{em}	z_{abs}	Telescope/ instrument	Wavelength range[a] (Å)	Resolution (km s^{-1})	Integration time (s)	S/N[b]	Programme ID
J0955+4116	19.38	3.420	3.280	KECK/HIRES	3839 – 6718	6.3	32 400	20	N162Hb, C320Hb
				KECK/HIRES	3242 – 7805	8.7	14 400	18	A152Hb
J1001+0343	17.72	3.198	3.078	VLT/UVES	3282 – 6652	7.3	33 700	28	083.A-0042(A)
				VLT/UVES	3756 – 10429	7.3	28 800	11	105.20L3.001

[a] With some wavelength gaps.

[b] Near the accessible O I line — either λ1302 or λ1039

identified by Penprase et al. (2010) as an EMP DLA, based on observations with the Keck Echellete Spectrograph and Imager. This quasar was then observed using the High Resolution Echelle Spectrometer (HIRES; Vogt et al. 1994) on the Keck I telescope. The C1 (7.0×0.861 arcsec slit) and C5 (7.0×1.148 arcsec slit) deckers were utilised, resulting in a spectral resolution of 49 000 and 37 000, respectively. These observations consist of 9×3600 s exposures using the C1 set up and 4×3600 s exposures using the C5 set up.

Prior observations of the $m_r = 17.7$ quasar, J1001+0343, using the Ultraviolet and Visual Echelle Spectrograph (UVES; Dekker et al. 2000) at the European Southern Observatory (ESO) Very Large Telescope (VLT) revealed that the intervening DLA at $z_{\rm abs} = 3.078$ is one of the least polluted gas reservoirs currently known. The 9.3 hours of VLT/UVES data presented in Cooke et al. (2011b) indicate that [Fe/H] $= -3.18 \pm 0.15$ and [O/Fe] $= +0.53 \pm 0.16$. Given that the typical [O/Fe] abundance observed amongst very metal-poor (VMP; [Fe/H] < -2) DLAs is $\sim +0.4$, the EMP DLA towards J1001+0343 is ideally placed to investigate if the [O/Fe] abundance is elevated at the lowest metallicities. The observations carried out by Cooke et al. (2011b) covered the wavelength range 3740 – 6650 Å. Thus, the iron abundance was determined from observations of the Fe II λ1608 line. We have secured further observations that focus on red wavelengths and target the stronger Fe II λ2344 and λ2382 features of this DLA. The new data on J1001+0343 were collected with UVES ($R \simeq 40\,000$) throughout P106 and P108 spanning the wavelength range 3756 – 4985 Å and 6705 – 10429 Å using a 0.8 arcsec slit width. We acquired 8×3600 s exposures on target using 2×2 binning in slow readout mode. A summary of our observations can be found in Table 5.1. These data are part of our ongoing programme to measure the chemical composition of the least polluted gas clouds in the Universe.

5.2.1 Data reduction

The HIRES data were reduced with the MAKEE reduction pipeline while the ESO data were reduced with the EsoRex reduction pipeline. Both pipelines include the standard reduction steps of subtracting the detector bias, locating and tracing the echelle orders,

flat-fielding, sky subtraction, optimally extracting the 1D spectrum, and performing a wavelength calibration. The data were converted to a vacuum and heliocentric reference frame.

Finally, the individual exposures of each DLA were combined using UVES_POPLER[2]. This corrects for the blaze profile, and allowed us to manually mask cosmic rays and minor defects from the combined spectrum. When combining these data we adopt a pixel sampling of 2.5 km s^{-1}. Due to the different resolutions of the C1 and C5 HIRES deckers, we separately combine and analyse the data collected using each setup. For the regions of the J1001+0343 spectrum $\sim$ 9000 Å, that are imprinted with absorption features due to atmospheric H_2O, we also perform a telluric correction with reference to a telluric standard star. We test the robustness of this correction by also analysing the extracted spectra of the individual exposures (as discussed further in Section 5.3.2).

5.3 Analysis

Using the Absorption LIne Software (ALIS) package[3]— which uses a χ-squared minimisation procedure to find the model parameters that best describe the input data — we simultaneously analyse the full complement of high S/N and high spectral resolution data currently available for each DLA. We model the absorption lines with a Voigt profile, which consists of three free parameters: a column density, a redshift, and a line broadening. We assume that all lines of comparable ionization level have the same redshift, and any absorption lines that are produced by the same ion all have the same column density and total broadening. The total broadening of the lines includes a contribution from both turbulent and thermal broadening. The turbulent broadening is assumed to be the same for all absorption features, while the thermal broadening depends inversely on the square root of the ion mass; thus, heavy elements (e.g. Fe) will exhibit absorption profiles that are intrinsically narrower than the profiles of lighter elements, (e.g. C). There is an

[2]UVES_POPLER is available from: https://github.com/MTMurphy77/UVES_popler

[3]ALIS is available from:
`https://github.com/rcooke-ast/ALIS`.

Table 5.2. Ion column densities of the DLA at $z_{\rm abs}$ = 3.279912 towards the quasar J0955+4116. The quoted column density errors are the 1σ confidence limits.

Ion	Transitions used	$\log_{10} N$(X)/cm^{-2}	[X/H]	[X/Fe]
H I	1215	20.24 ± 0.05	—	—
C II	1036, 1334	13.74 ± 0.10	−2.90 ± 0.11	+0.06 ± 0.13
O I	988.6, 988.7, 988.8, 1302	14.44 ± 0.04	−2.46 ± 0.06	+0.50 ± 0.10
Al II	1670	11.21 ± 0.35	−3.45 ± 0.35	−0.49 ± 0.36
Si II	1260, 1304, 1526	12.89 ± 0.06	−2.83 ± 0.07	+0.13 ± 0.11
Fe II	1144, 1608	12.72 ± 0.09	−2.96 ± 0.10	—

additional contribution to the line broadening due to the instrument. For the HIRES and UVES data, the nominal instrument resolutions are $v_{\rm FWHM}$ = 6.28 km s^{-1} (HIRES C1), $v_{\rm FWHM}$ = 8.33 km s^{-1} (HIRES C5), and $v_{\rm FWHM}$ = 7.3 km s^{-1} (UVES). Finally, we note that we simultaneously fit the absorption and quasar continuum of the data. We model the continuum around every absorption line as a low order Legendre polynomial (typically of order 3). We assume that the zero-levels of the sky-subtracted UVES and HIRES data do not depart from zero[4]. In the following sections we discuss the profile fitting for each DLA in turn.

5.3.1 J0955+4116

J0955+4116 is best modelled with two gaseous components at $z_{\rm abs} = 3.279912 \pm 0.000001$ and $z_{\rm abs}$ = 3.27997 ± 0.00001 for all singly ionized species (except Fe II), and just the former component for neutral species (i.e. O I). We assume the temperature is 1×10^4 K (a value that is typical for a metal-poor DLA; see Cooke et al. 2015, Welsh et al. 2020, Noterdaeme et al. 2021) and find that the turbulent components are 3.3 ± 0.2 km s^{-1} and 13.4 ± 1.4 km s^{-1} respectively. The data, along with the best-fitting model are presented in Figure 5.1, while the corresponding column densities are listed in Table 5.2. These results are unchanged when the assumed temperature varies between $\sim (0.5 - 1.2) \times 10^4$ K — the typical range expected for metal-poor DLAs (Cooke et al., 2015).

Note, we only use the neutral component (identified in the O I absorption) to infer the relative chemical abundances of this gas cloud; the component at $z_{\rm abs}$ = 3.27997 likely

[4]We visually inspected the troughs of saturated absorption features to confirm this is the case.

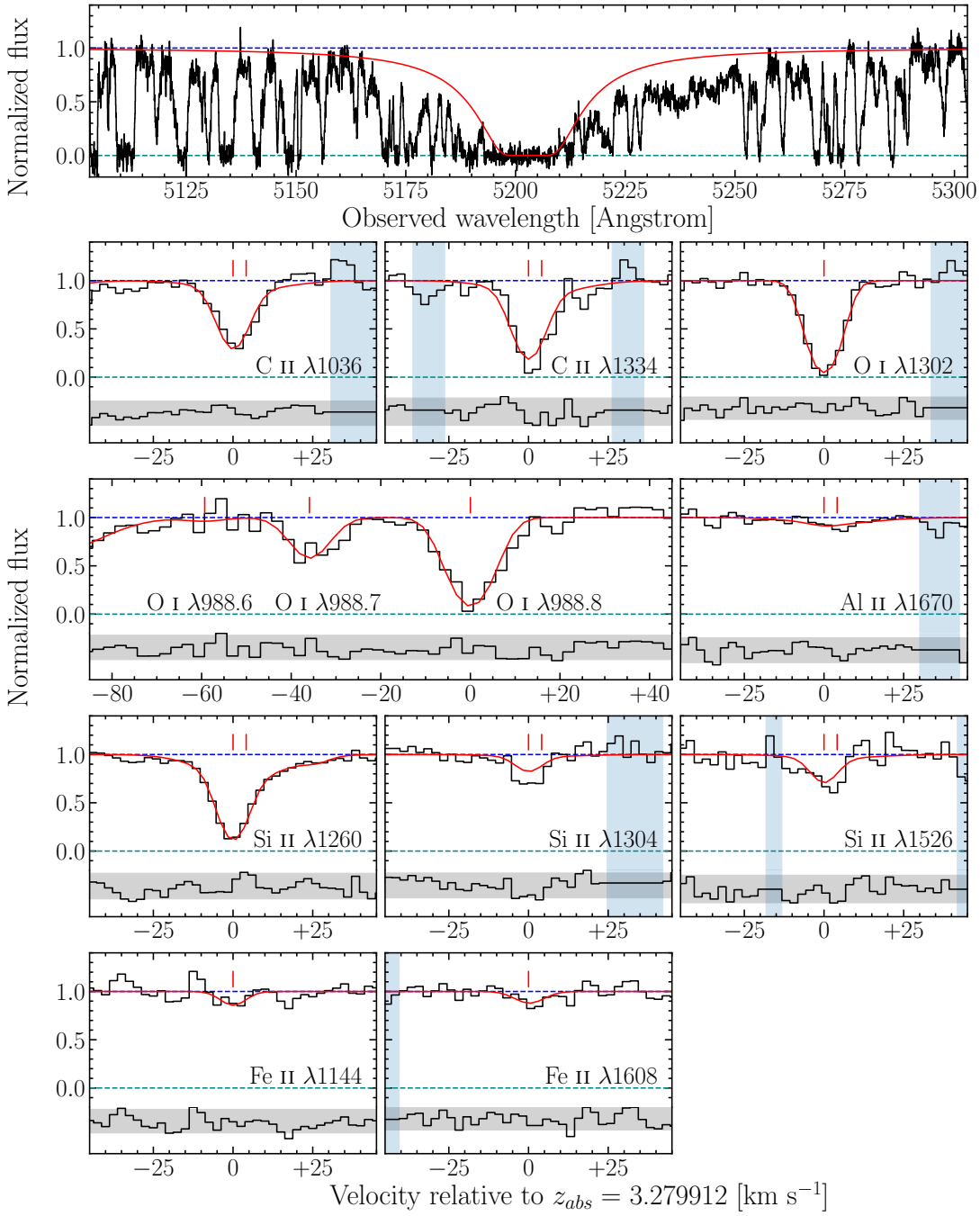

Figure 5.1. Continuum normalised HIRES data (black histograms) of the absorption features produced by metal ions associated with the DLA at $z_{\rm abs}$ = 3.279912 towards the quasar J0955+4116. The best-fitting model is shown with the red curves. The blue dashed line indicates the position of the continuum while the green dashed line indicates the zero-level. The red ticks above the absorption features indicate the centre of the Voigt line profiles. Below the zero-level, we show the residuals of this fit (black histogram) where the grey shaded band encompasses the 2σ deviates between the model and the data. The vertical blue shaded bands indicate the regions of the spectrum not included in the fit.

Table 5.3. Ion column densities of the DLA at $z_{\rm abs} = 3.078408$ towards the quasar J1001+0343. The quoted column density errors are the 1σ confidence limits.

Ion	Transitions used	$\log_{10} N$(X)/cm^{-2}	[X/H]	[X/Fe]
H I	1215	20.20 ± 0.05	—	—
C II	1036, 1334	13.57 ± 0.01	-3.06 ± 0.01	$+0.19 \pm 0.05$
N I	1200	≤ 12.50[a]	≤ -3.53	≤ -0.28
O I	1039, 1302	14.26 ± 0.01	-2.63 ± 0.01	$+0.62 \pm 0.05$
Si II	1190, 1260, 1304, 1526	12.86 ± 0.01	-2.85 ± 0.01	$+0.40 \pm 0.05$
S II	1253	≤ 12.91[a]	≤ -2.41	$\leq +0.84$
Fe II	1608, 2382	12.42 ± 0.05	-3.25 ± 0.05	—

[a] 3σ upper limit on column density.

arises from ionized gas. The neutral component at $z_{\rm abs} = 3.279912$ constitutes 76% to the total absorption in Si II. We find that [Fe/H] $= -2.96 \pm 0.10$ while [O/Fe] $= +0.50 \pm 0.10$. This places the DLA towards J0955+4116 at the cusp of the EMP regime where the plateau in [O/Fe] may change.

5.3.2 J1001+0343

J1001+0343 is best modelled with one component at $z_{\rm abs} = 3.078408 \pm 0.000006$ with a turbulence $b = 6.3 \pm 0.4$ km s^{-1} and temperature $T = (1.0 \pm 0.6) \times 10^4$ K. The data, along with the best-fitting model are presented in Figure 5.2, while the corresponding column densities are listed in Table 5.3. We find that [Fe/H] $= -3.25 \pm 0.05$ and [O/Fe] $= +0.62 \pm 0.05$. All reported column densities are consistent with the previous determinations by Cooke et al. (2011b), but with a reduced error; in particular, the new data reported here have allowed the precision on the [O/Fe] measurement to be improved by a factor of three, from 0.15 to 0.05.

When analysing the DLA towards J1001+0343, we adopt two approaches for modelling the Fe II absorption features. The Fe II λ2344 and λ2382 features fall in regions of the spectrum that are impacted by telluric absorption; the DLA absorption features are therefore partially blended with telluric features to varying degrees of severity. Prior to combining the individual DLA exposures, we remove these features using the spectrum of a telluric standard star. The resulting data near the Fe II λ2382 line, after performing this correction, are shown in the right panel of the third row of Figure 5.2. To ensure that we have not

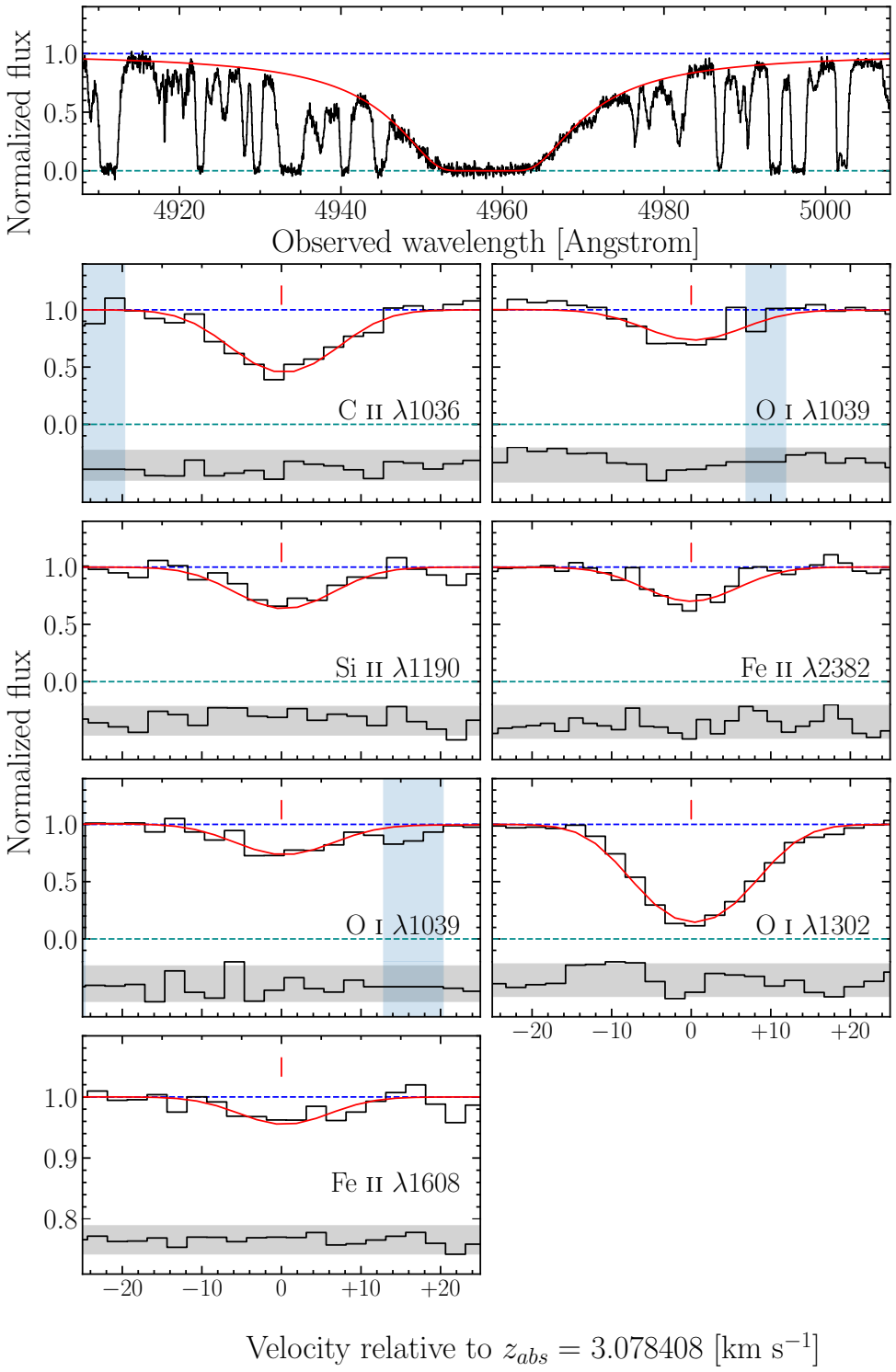

Figure 5.2. Continuum normalised UVES data (black histograms) of the absorption features produced by metal ions associated with the DLA towards J1001+0343. The top row shows H I. The second and third rows show our new programme data (programme ID: 105.20L3.001) while the bottom two rows show the archival data (programme ID: 083.A-0042(A)). The best-fitting model profiles are shown as red curves. The blue dashed line indicates the position of the continuum while the green dashed line indicates the zero-level. The red ticks above the absorption features indicate the centre of the Voigt line profiles. Below the zero-level, we show the residuals of this fit (black histogram) where the grey shaded band encompasses the 2σ deviates between the model and the data. The vertical blue shaded bands indicate the regions of the spectrum not included in the fit.

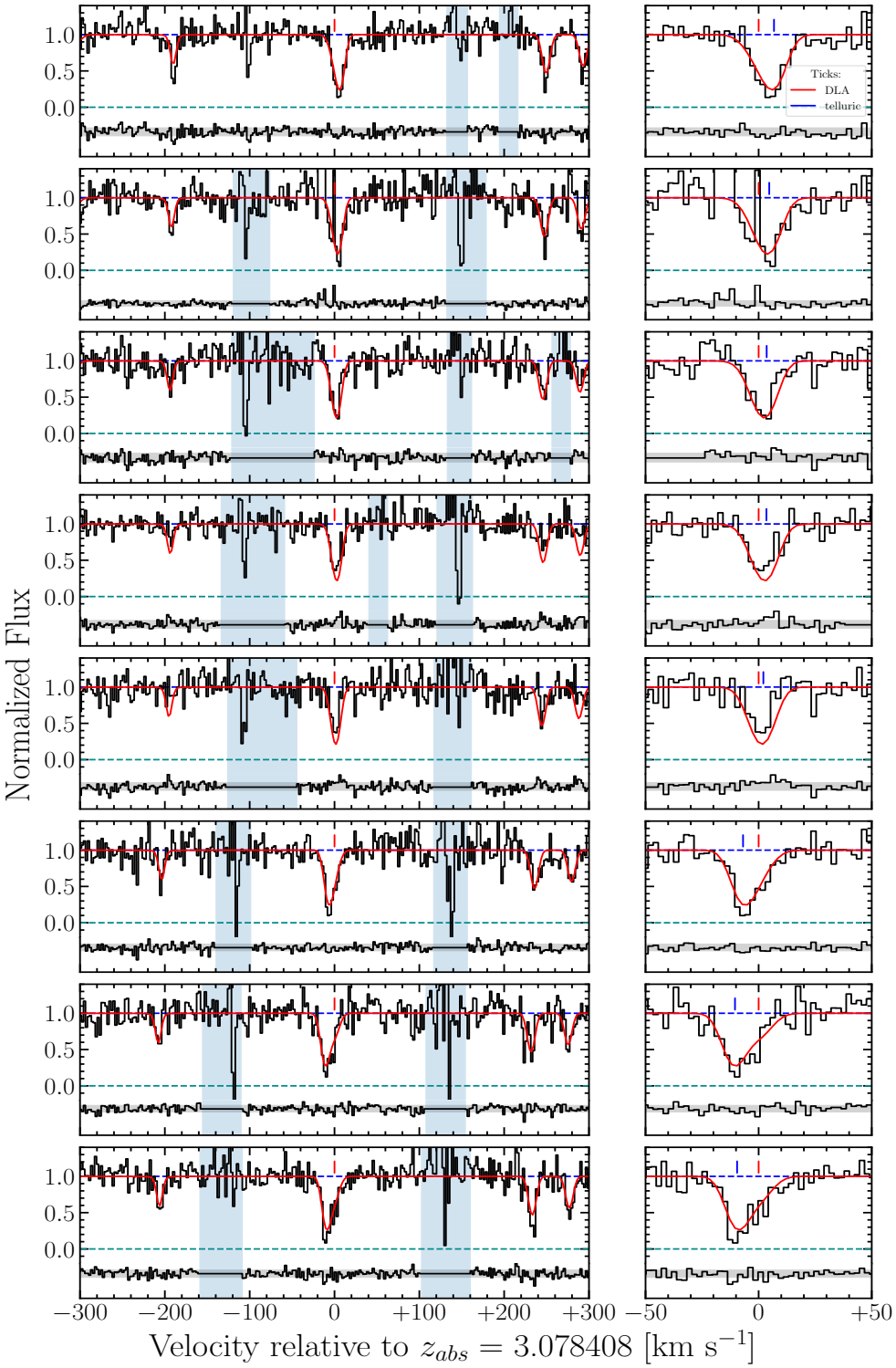

Figure 5.3. Continuum normalised UVES data (black histograms) of the absorption features produced by Fe II λ2382 associated with the DLA towards J1001+0343 along with the surrounding telluric absorption features for each exposure. The right panels show a zoom in of the left panels. Overplotted in red is our best-fitting model of the Fe II λ2382 feature and the telluric absorption. The blue dashed line indicates the position of the continuum while the green dashed line indicates the zero-level. The red ticks above the absorption features indicate the centre of the Voigt line profiles of the DLA, while the blue tick marks indicate the line centre of the telluric features. Below the zero-level, we show the residuals of this fit (black histogram) where the grey shaded band encompasses the 2σ deviates between the model and the data. The vertical blue shaded bands indicate the regions of the spectrum not included in the fit.

introduced any artefacts in the data, we simultaneously fit the standard star spectrum and all of the individual quasar exposures (uncorrected for telluric absorption). The results of this fitting procedure are shown in Figure 5.3. From this figure it is clear that, while the Fe II λ2382 feature is partially blended with a telluric absorption line, the range of dates used to observe this target results in a sequential shift in the position of the telluric feature relative to the Fe line of interest. In the top right panel of Figure 5.3, the telluric absorption is $\sim +5$ km s^{-1} from the Fe II λ2382 line center (as indicated by the blue tick mark). In the bottom right panel, the telluric absorption is ~ -10 km s^{-1} from the Fe II λ2382 line center. When jointly analysing these data, this shift allows us to capture an accurate profile of both the telluric and Fe II features. Note, the centroid of the Fe II λ2382 line is tied to the other DLA absorption features, while the centroid of the telluric feature is fixed from other telluric lines in the standard star spectrum. Using this approach we find a total Fe II column density consistent with our analysis of the corrected combined spectrum.

These new data confirm that the DLA towards J1001+0343 is one of the most metal-poor DLAs currently known. The new found precision afforded for the iron column density allow us to conclude that [O/Fe] is significantly elevated in this DLA compared to the plateau observed at higher metallicity. Before discussing the origin of this elevation, we perform some simulations to support our analysis.

5.3.3 Mock models

To further test if the DLA towards J1001+0343 exhibits an elevated [O/Fe] ratio, we have simulated the O I and Fe II absorption line profiles that would be expected given different underlying [O/Fe] abundance ratios. To achieve this, we take the best fit cloud model from our modelling procedure and generate synthetic model profiles varying the column density of either O I or Fe II. The results of this test are shown in Figure 5.4. The top row shows the observed UVES data centered on the O I λ1039 (left) and O I λ1302 (right) absorption features. Overplotted on these data are the model profiles that would be expected if the underlying [O/Fe] ratio were +0.4, +0.6, and +0.8. To generate these profiles, we assume

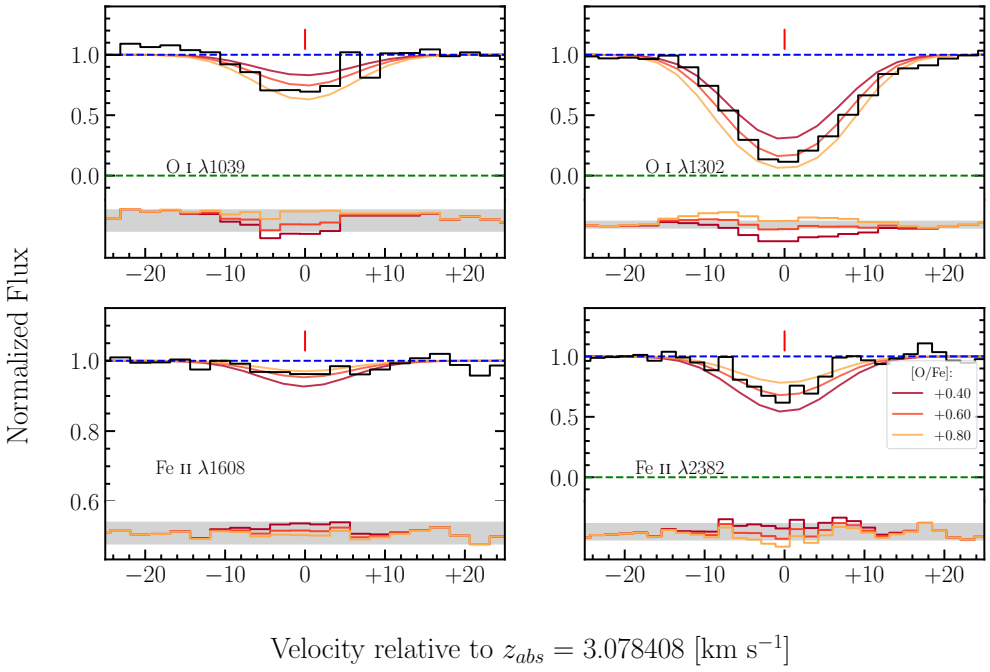

Figure 5.4. Models of O I and Fe II absorption components overplotted on the UVES data of J1001+0343. The colour indicates the underlying abundance ratio [O/Fe] as highlighted in the legend. The top panels shows the O I data and the corresponding O I model profiles assuming a fixed Fe II column density. The bottom panels show the corresponding Fe II model profiles assuming a fixed O I column density. These fixed values represent the best fit column densities of the data. Note the different y-axis range of the Fe II λ1608 panel.

that the Fe II column density is fixed (at the value given by our best fit model) and then vary the column density of O I accordingly. In the bottom row we show the UVES data centered on the Fe II λ1608 (left) and Fe II λ2382 (right) lines. The overplotted models show the same underlying [O/Fe] abundance ratios as the top row, however, in this case we vary the column density of Fe II (while the column density of O I is fixed at the value given by our best fit model). Below these data we show the residual fits between the model and the data. The grey shaded band represents the two sigma limits provided by our best fit model ([O/Fe] = +0.62 ± 0.05) and the data. In each panel (except Fe II λ1608), the residual showcasing the fit of the [O/Fe] = +0.4 model (dark red; see legend) is outside of this 2σ range. From this analysis, we find it improbable that these data show an [O/Fe] abundance ratio that is consistent with the plateau seen at [Fe/H] > −3.

5.4 Discussion

The primary goal of this paper is to assess if EMP DLAs (those with [Fe/H] < −3.0) exhibit an enhanced [O/Fe] abundance relative to VMP DLAs (those with −3.0 < [Fe/H] < −2.0). Figure 5.5 shows the [O/Fe] abundance ratio as a function of the [Fe/H] metallicity for the DLAs analysed in this work (red symbols), together with literature measurements of VMP and EMP DLAs (blue symbols) and stars (gray symbols). The DLA abundances used to produce this figure are given in Appendix C. The new data reported here confirm that the DLA towards J1001+0343 is a bonafide EMP DLA, while the DLA towards J0955+4116 is on the cusp of the EMP regime. Qualitatively, the [O/Fe] values of these DLAs are consistent with the trend of an increased [O/Fe] ratio below [Fe/H] < −3. Given the metallicity of J0955+4116, it is reasonable to expect that the [O/Fe] abundance ratio of this DLA is consistent with the plateau seen at higher metallicity. The high precision [O/Fe] determination of J1001+0343 has strengthened the evidence that this system exhibits an elevated [O/Fe] ratio. With this new measurement, we determine the mean of this relative abundance ratio for the EMP DLAs shown in Figure 5.5: $[\langle O/Fe \rangle] = +0.67 \pm 0.04$. For VMP DLAs, $[\langle O/Fe \rangle] = +0.40 \pm 0.08$; this marks a 3σ distinction between the mean

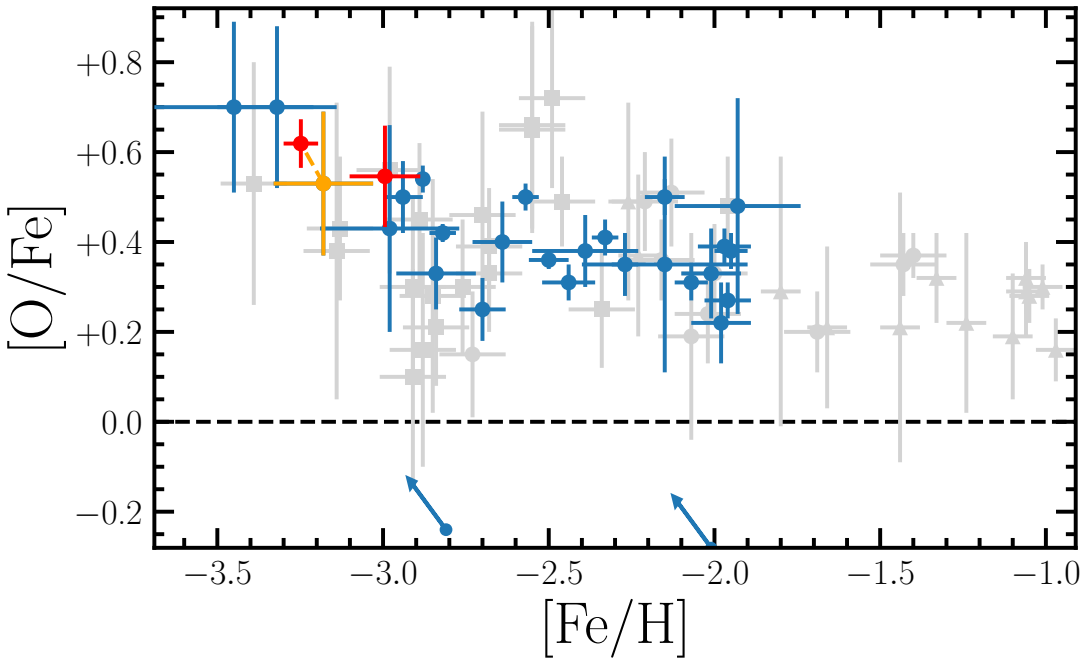

Figure 5.5. [O/Fe] vs [Fe/H] for all metal-poor DLAs and sub-DLAs (blue circles) plotted alongside [O/Fe] of metal-poor stars (light gray) — the shape of the marker indicates the source of the stellar data: circles - García Pérez et al. (2006), squares - Cayrel et al. (2004), triangles - Nissen et al. (2002) (all values are those presented in the Cooke et al. 2011b reanalysis). The two [O/Fe] abundances reported here are shown in red. The previous measurement of J1001+0343 is marked in orange and is connected to the latest measurement by a dashed line. The black dashed line indicates the solar relative abundance.

values reported in these regimes.

There are no obvious selection biases that may have caused this apparent inflection of [O/Fe] at the lowest metallicities probed. If this trend is confirmed with future [O/Fe] measurements of EMP DLAs, it will highlight that EMP DLAs exhibit a distinct chemical enrichment relative to VMP DLAs; the source of the elevated [O/Fe] in these metal-poor DLAs may be attributed to enrichment by a generation of metal-free stars (Heger & Woosley, 2010). However, before we consider the abundance pattern of this DLA in relation to the yields of Population III SNe, we first consider the origin of this elevation.

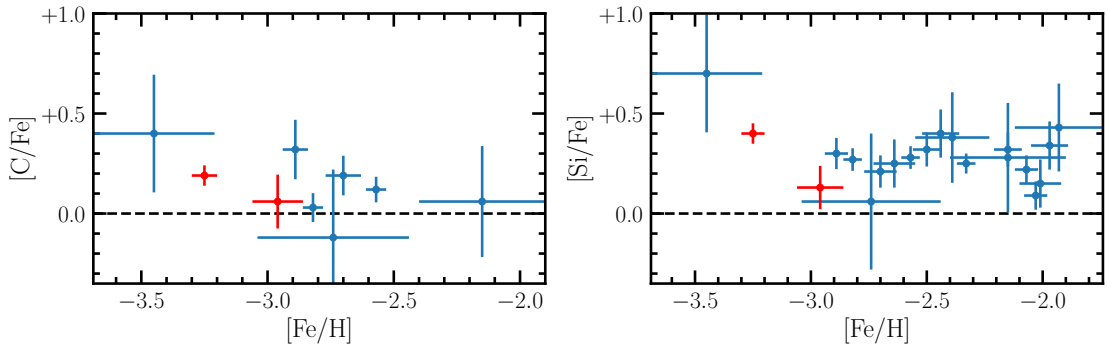

Figure 5.6. [C/Fe] (left) and [Si/Fe] (right) vs [Fe/H] for all metal-poor DLAs and sub-DLAs (blue circles). The abundances of the DLAs reported here are shown in red. The black dashed line indicates the solar relative abundance.

5.4.1 Origin of elevation

Dust depletion is expected to be minimal for VMP DLAs (Pettini et al., 1997; Akerman et al., 2005; Vladilo et al., 2011; Rafelski et al., 2014). However, if the depletion of metals onto dust grains is unaccounted for, it will lead to artificially low metal abundance determinations for refractory elements. It is therefore useful to rule out its impact in the DLAs presented here. Depletion studies compare the relative abundances of elements in DLAs to the expected nucleosynthetic ratio which can be inferred from the abundances of stars of similar metallicity. O is minimally depleted onto dust grains (Spitzer & Jenkins, 1975). Both Si and Fe are refractory elements, and are partially depleted onto dust grains but at different rates. As shown in Figure 5.5, both metal-poor halo stars and VMP DLAs exhibit an identical evolution of the [O/Fe] ratio (see also Figure 12 of Cooke et al., 2011b). Given this agreement, we therefore expect dust depletion to be minimal in DLAs that have a metallicity [Fe/H] < -2.

We can also use the [Si/Fe] abundance ratio to explore the possibility of dust depletion. The most metal-poor stars and the most metal-poor DLAs appear to have a metallicity independent evolution of [Si/Fe] when [Fe/H] < -2. For stars, the plateau occurs at [Si/Fe] = +0.37 ± 0.15 (Cayrel et al., 2004). While for DLAs, the plateau occurs at [Si/Fe] = +0.32 ± 0.09 (Wolfe et al., 2005; Cooke et al., 2011b). The [Si/Fe] of both J0955+4116 and J1001+0343 are consistent with the plateau seen in metal-poor DLAs

(see Figure 5.6). We therefore do not expect dust depletion to be the source of the elevated [O/Fe] abundance ratio. Volatile elements, like S and Zn, are less readily depleted onto dust grains than Si and Fe (Savage & Sembach, 1996). These elements are not currently accessible for the EMP DLAs studied here. However, the advent of the next generation of 30+ m telescopes will make these abundance determinations possible for EMP DLAs.

We therefore conclude that the elevated oxygen to iron abundance ratio observed for the EMP DLA towards J1001+0343 is intrinsic to the DLA. We note that the O I column densities of both DLAs are derived from at least one weak absorption line; the derived column densities are therefore unlikely to depend on the cloud model. Furthermore, we note that ionization effects cannot explain this behaviour at low metallicity. If some of the gas associated with the DLA is ionized, this will increase the Fe II column density, and the O I column density will be unaffected; the net result would be a *reduction* of the [O/Fe] ratio, while we are reporting an [O/Fe] enhancement.

5.4.2 Stochastic enrichment

In the previous section, we concluded that the observed [O/Fe] ratio is intrinsic to the DLA towards J1001+0343. We now explore the possibility that this DLA has been enriched by the first generation of stars. Specifically, we compare the observed abundance pattern of this DLA to those predicted by a stochastic chemical enrichment model developed in previous work (Welsh et al., 2019). This model describes the underlying mass distribution of the enriching stellar population using a power-law: $\xi(M) = kM^{-\alpha}$, where k is a multiplicative constant that is set by the number of enriching star that form between a given mass range:

$$N_\star = \int_{M_{\rm min}}^{M_{\rm max}} kM^{-\alpha} \mathrm{d}M \tag{5.4.1}$$

Since the first stars are thought to form in small multiples, this underlying mass distribution is necessarily stochastically sampled. We utilise the yields from simulations of stellar evolution to construct the expected distribution of chemical abundances given a underlying IMF model. These distributions can then be used to assess the likelihood of the observed

DLA abundances given any underlying enrichment model.

In our analysis, we use the relative abundances of [C/O], [Si/O], and [Fe/O] when investigating the enrichment of the DLA towards J1001+0343. We compare these abundances to those predicted using the nucleosynthetic yields of massive (> 10 $M_\odot$) metal-free stars from Heger & Woosley (2010). These yields have been calculated as a function of the progenitor star mass (M), the explosion energy of their supernova ($E_{\rm exp}$), and the mixing between the different stellar layers ($f_{\rm He}$). The explosion energy is a measure of the final kinetic energy of the ejecta at infinity while the mixing between stellar layers is parameterised as a fraction of the helium core size. For further details, see both Heger & Woosley (2010) and Welsh et al. (2019).

While the Heger & Woosley (2010) yields have been calculated for metal-free stars, they are also representative of EMP Population II CCSNe yields (at least for the elements under consideration in this work); this can be seen by comparison with the Woosley & Weaver (1995) yields of metal-enriched massive stars. As a result, in previous studies of near-pristine absorption line systems, it has been difficult to distinguish between enrichment by Population II and Population III stars. Fortunately, in our analysis, we can take advantage of this degeneracy.

The default enrichment model, described above, contains five free parameters ($N_\star$, $M_{\rm min}$, $M_{\rm max}$, α, $E_{\rm exp}$, and $f_{\rm He}$). We are using three relative abundances to assess the enrichment of the DLA towards J1001+0343. Thus, we cannot simultaneously investigate these five parameters. We can, however, make some simplifications under the assumption of enrichment by Population II SNe. The underlying IMF of the first stars remains an open question. This is not the case for massive Population II stars. The Population II IMF for stars with a mass $M \gtrsim 10\,M_\odot$ should be well-described by a Salpeter IMF (i.e. α = 2.35 in Equation 5.4.1)[5]. Under this assumption, if the number of enriching stars we derive is large, then this may imply that Pop II stars are the dominant enrichment source. Alternatively, if $N_\star$ is low, then it is possible that a pure or washed out Pop III signature

[5]This was the first local measurement of the stellar IMF (Salpeter, 1955) — see Bastian et al. (2010) for a review.

may still be present in this DLA.

We test this idea by using a Markov Chain Monte Carlo (MCMC) likelihood analysis to investigate the number of stars that have enriched this DLA. We explore the entire enrichment model parameter space to find the parameters that best fit our data. The Heger & Woosley (2010) parameters span $(10 - 100)$ $M_\odot$ (with a mass resolution of $\Delta M \gtrsim 0.1$ $M_\odot$), $(0.3 - 10) \times 10^{51}$ erg (sampled by 10 values), and $(0 - 0.25)$ $f_{\rm He}$ (sampled by 14 values) where $f_{\rm He}$ is the fraction of the He core size; in total, there are 16 800 models in this yield suite. During our analysis, we linearly interpolate between this grid of yields while applying uniform priors on each parameter. The results of this analysis are shown in Figure 5.7. We find that this DLA is preferentially enriched by a low number of massive SNe. The most favoured result of this model is that the DLA towards J1001+0343 was enriched by a low number of massive stars and, thus, we cannot rule out the possibility that this DLA contains a Pop III fingerprint.

Motivated by these findings, we now assess the possible properties of a putative metal-free star that may be responsible for the enrichment of the DLA towards J1001+0343. In this case we assume that the DLA has been enriched by one Population III SN, again utilising the Heger & Woosley (2010) yields. The results of this analysis are shown in Figure 5.8. We find that the abundances of this DLA are best modelled by a Population III star with a mass between $17 - 27$ $M_\odot$ (2σ) and an explosion energy between $(1 - 3) \times 10^{51}$ erg (2σ). The degree of mixing between the stellar layers remains unconstrained, but generally favours lower values of the mixing parameter. To test how well this model describes our data, we compare the [X/O] ratios supported by this model to those presented in Table 5.3. This comparison is shown in Figure 5.9. The [C/O], [Si/O], and [Fe/O] of this DLA are simultaneously well described by the inferred likelihood model. The Population III star that best models the abundances of the DLA towards J1001+0343 has an explosion energy that is consistent with the value found for a typical metal-poor DLA (Welsh et al., 2019). The results of this analysis are also similar to the inferred enrichment of the most metal-poor DLA currently known; Cooke et al. (2017) find that the abundance pattern of the most metal-poor DLA can be well-modelled by a Population III SN with a progenitor

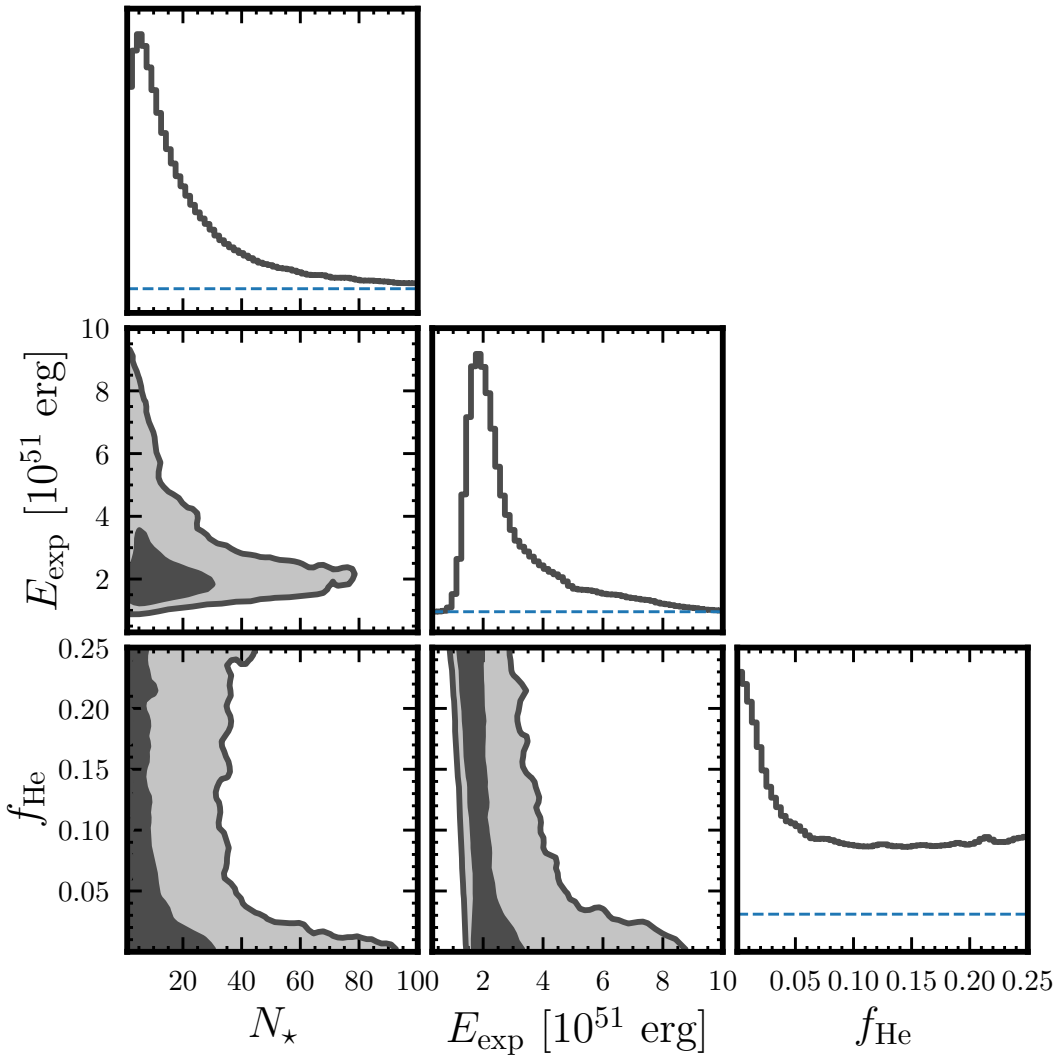

Figure 5.7. Results of our MCMC analysis of the chemical enrichment of the DLA towards J1001+0343 given our stochastic model. From left to right, we show the number of enriching stars, the explosion energy, and the degree of mixing. The diagonal panels indicate the maximum likelihood posterior distributions of the model parameters while the 2D contours indicate the correlation between these parameters. In the diagonal panels, the horizontal blue dashed line indicates the zero-level of each distribution.

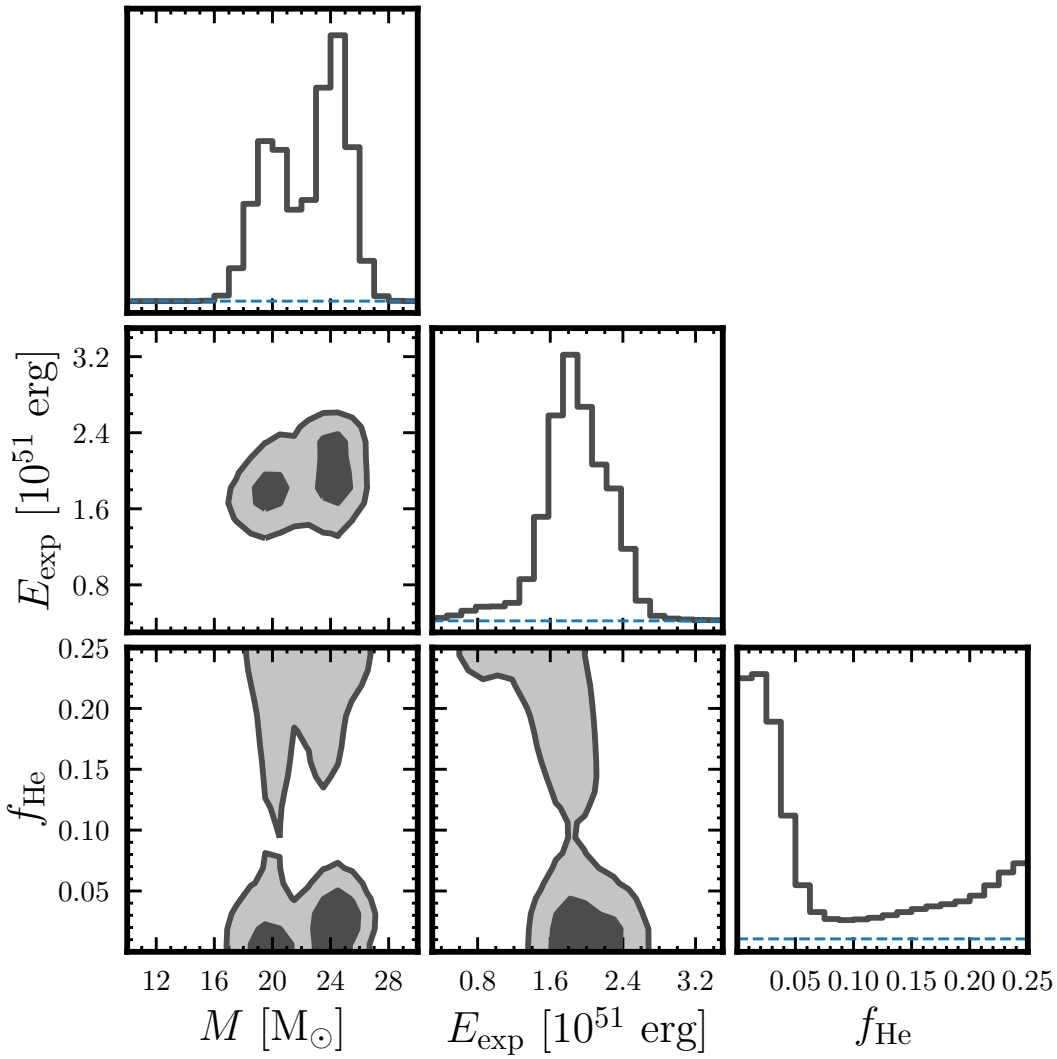

Figure 5.8. Results of our MCMC analysis of the chemical enrichment of the DLA towards J1001+0343 assuming the number of enriching stars $N_\star = 1$. From left to right, we show the progenitor star mass, the explosion energy, and the degree of mixing. The diagonal panels indicate the maximum likelihood posterior distributions of the model parameters while the 2D contours indicate the correlation between these parameters. In the diagonal panels, the horizontal blue dashed line indicates the zero-level of each distribution.

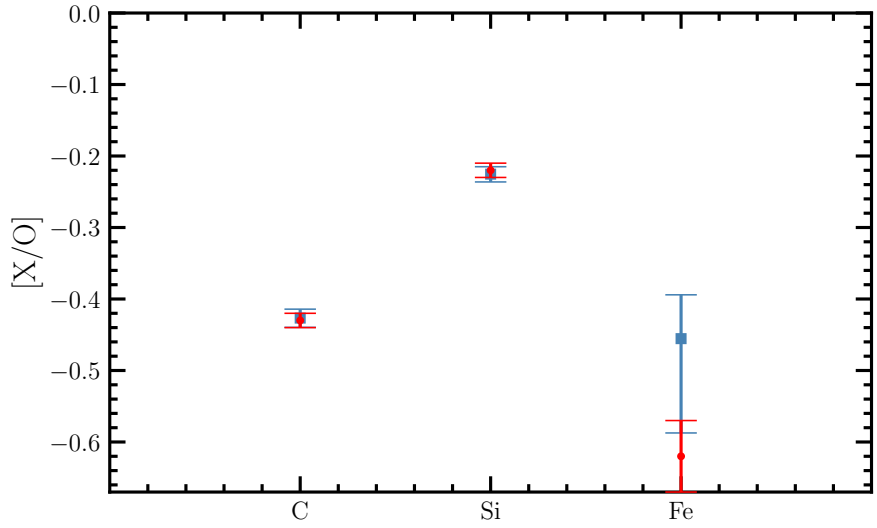

Figure 5.9. The observed abundances of the DLA towards J1001+0343 (red circles) compared to the best fit abundance ratios inferred by our best fit enrichment model (blue squares). The blue error bars encompass the interquartile range of the model values.

mass $M = 20.5\,\mathrm{M}_{\odot}$. The DLA analysed in Cooke et al. (2017) was preferentially modelled with a somewhat higher explosion energy than that reported here, but still consistent within 2σ. This preference towards higher energy explosions (i.e. hypernovae) is also inferred from the analysis of some EMP stars (e.g. Grimmett et al. 2018; Ishigaki et al. 2018). Though, the Heger & Woosley (2010) analysis of the Cayrel et al. (2004) sample of EMP stars favoured models with an explosion energy between $(0.6 - 1.2) \times 10^{51}$ erg. At present, the models are driven by the relatively low errors on the [C/O] and [Si/O] abundances. Future higher S/N observations would allow us to detect additional odd atomic number elements (e.g. N, Al), and iron-peak elements (e.g. Ni, Cr, Zn). These elements may allow us to pin down the properties of the enriching stars more thoroughly. For example, recent work by Ezzeddine et al. (2019) suggests that aspherical SNe yields may be necessary to describe the yields of some of the most metal-poor stars known. An informative probe of the explosion physics is the relative abundance of zinc and iron — we do not detect zinc absorption in this DLA, but this may be possible with the next generation of 30+ m telescopes.

5.4.3 Ruling out Population II

In the previous section we investigated the chemical enrichment of the DLA towards J1001+0343. Under the assumption of a Sapleter IMF, we found that this DLA was best modelled by a low number of enriching stars (consistent with one). We also found that the observed abundances of [C/O], [Si/O], and [Fe/O] can be simultaneously well modelled by the yields of an individual Population III SN. However, given the age of the Universe at redshift $z = 3$ ($\sim$ 2 Gyr), there is sufficient time ($\sim$ 1.5 Gyr between $z = 10$ to $z = 3$) for this DLA to be enriched by Population III stars and subsequent Population II stars. Any putative Population III signature is thought to be washed out soon after the birth of Population II stars (Ji et al., 2015); just a few massive Population II stars are required to wash out a peculiar Population III chemical signature. Though, there could be a delay between Population III and Population II star formation. For example, reionization quenching can temporarily suspend star formation in low mass galaxies (Oñorbe et al., 2015; Wheeler et al., 2015), and this may prolong the time that a Population III signature can be preserved in near-pristine gas. After a period of dormancy, interactions with gaseous streams in the intergalactic medium can help re-ignite star formation in these low mass objects (Wright et al., 2019). Interestingly, the chemistry of the most metal-poor DLAs shows an increase in [C/O] with decreasing redshift (see Figure 8 of Welsh et al., 2020). One interpretation of this trend is that EMP DLAs universally experienced some degree of reionization quenching; the increase in [C/O] with decreasing redshift is interpreted as the onset of enrichment from the carbon yield of the first (i.e. Population II) intermediate mass stars.

To reduce the possibility of Population II contamination, one might consider measurements of the [O/Fe] ratio close to the epoch of reionization. For example, Bañados et al. (2019) recently reported the detection of a near-pristine DLA at $z = 6.4$. While the current determinations of the metallicity and [O/Fe] abundance of this system ([Fe/H] = -2.94 ± 0.26; [O/Fe] = $+0.02 \pm 0.21$) are quite uncertain, future higher spectral resolution and higher signal-to-noise ratio observations would allow the chemistry of this gas cloud to be inferred

from weak absorption lines, potentially improving the precision of this measurement by an order of magnitude. With the current data, they find no evidence of a Population III chemical fingerprint. The best-fit value of the [O/Fe] value of the Bañados et al. (2019) DLA places this system below the typical [O/Fe] abundance of VMP DLAs (at $\sim 1.7\sigma$ confidence). Considering the high [O/Fe] ratio reported in this paper, if the [O/Fe] value of the Bañados et al. (2019) DLA remains unchanged with future observations, this would be a signpost of stochastic chemical enrichment at the lowest metallicity — this may also be a signature of Population III star formation.

While it may be difficult to distinguish the absolute chemical yields of Pop II versus Pop III stars, it may be possible to identify a transition of Pop III to Pop II enrichment by empirically looking for a change in the behaviour of chemical abundance ratios at the lowest metallicity. Given the tight [O/Fe] plateau seen in VMP DLAs combined with the evidence of an increased [O/Fe] ratio in some EMP DLAs, we thus propose that the [O/Fe] abundance may offer the cleanest probe of the Pop III to Pop II transition in the most metal-poor DLAs.

5.4.4 Unravelling the Population III fingerprint

We have mentioned both EMP stars and EMP DLAs as potential environments to uncover the Population III fingerprint. Both stars and DLAs have their respective advantages. The large sample size afforded when studying stellar relics cannot be matched in similar studies of gaseous relics. The potential evolution of [O/Fe] across EMP stars has also been the subject of much discussion (see the review by McWilliam, 1997). However, determining this ratio for EMP stars is particularly challenging. There are four approaches to determine the oxygen abundance in stellar atmospheres. The typical method utilises the O I λ7771 – 5, triplet; a transition that requires large non-LTE corrections (Fabbian et al., 2009). The weak O I λ6300 line is known to form in LTE and, as such, may be more reliable (Asplund, 2005). However, the strength of this feature means that it is challenging to detect at low metallicities. Given the difficulty of accurately determining this abundance in the lowest metallicity stars, we suggest that DLAs are the ideal environment to study the evolution of

this particular metal despite the smaller sample size.

The comparative analysis of the chemistry of both gaseous and stellar relics offer the opportunity to study early chemical enrichment further. It is well established that some of the most metal-poor Milky Way halo stars show an enhanced [C/Fe] ratio (Beers & Christlieb, 2005). It is curious that Figure 5.6 suggests that EMP DLAs do not exhibit any concurrent enhancement of the [C/Fe] or [Si/Fe] abundance ratios along with [O/Fe]. The enhancement of [O/Fe] in the EMP regime may not extend to other α elements across DLAs. The lack of concurrent [C/Fe] enhancement may suggest that the CEMP-no stars and the [O/Fe] enhanced DLAs have experienced divergent enrichment histories.

Another environment that may offer unique insight to the metals produced by the first stars are the ultra-faint dwarf galaxies (UFDs) that orbit the Milky Way. These UFDs contain some of the most metal-poor stars to date. Recent work by Skúladóttir et al. (2021) have shown that an EMP star within Sculptor can be modelled with the yields of a Population III hypernovae. The stars in these UFDs may have experienced a different enrichment history to the Milky Way halo stars. If metal-poor DLAs are indeed the antecedents of the UFDs, we might be able to search for this chemical signature in the most metal-poor stars of the UFDs.

5.5 Conclusions

Previous observations of metal-poor DLAs tentatively suggest that the *most* metal-poor DLAs display an elevated [O/Fe] ratio compared to their higher metallicity counterparts. The higher metallicity ([Fe/H] > -3) DLAs are well described by a plateau around a typical value of $[\langle \mathrm{O/Fe} \rangle] = +0.40 \pm 0.08$. The primary goal of this paper is to assess whether [O/Fe] is indeed elevated amongst the most metal-poor DLAs by presenting a detailed chemical abundance analysis of two near-pristine DLAs — J0955+4116 and J1001+0343, observed with Keck/HIRES and VLT/UVES respectively. Our main conclusions are:

(i) We find that the DLA towards J0955+4116 has a neutral hydrogen column density $\log_{10} N(\mathrm{H\,I})/\mathrm{cm}^{-2} = 20.24 \pm 0.05$ and a relative iron abundance [Fe/H] $= -2.96 \pm$

0.10. This places the gas cloud towards this quasar on the cusp of the EMP regime. The data collected using Keck/HIRES have revealed [O/Fe] = +0.50 ± 0.10. The [O/Fe] abundance of this DLA is therefore consistent with the plateau observed across DLAs whose [Fe/H] > −3.

(ii) We present new VLT/UVES data of the DLA toward J1001+0343 that cover previously unobserved Fe II features. These data provide a more precise determination of its chemical composition. We find [Fe/H] = -3.25 ± 0.05 and [O/Fe] = $+0.62 \pm 0.05$, reducing the error associated with these abundance determinations by a factor of three.

(iii) This [O/Fe] ratio of the DLA towards J1001+0343 is significantly (2.3σ) above the typical value of a VMP DLA. We have considered the abundances of other ions and this analysis suggests that neither dust depletion nor ionization corrections are the source of this elevation. Rather, the elevated value is intrinsic of the DLA.

(iv) The origin of this elevation can be explained if the higher metallicity DLAs with [O/Fe] $\sim$ +0.4 are all enriched by a similar population of stars, drawn from the same IMF. The divergence at the lowest metallicities likely represents enrichment from a distinct population of stars. The chemical composition of this DLA can be well modelled by the yields of a $(17 - 27)$ $M_{\odot}$ (2σ) Population III SN with a $(1 - 3) \times 10^{51}$ erg (2σ) explosion.

We suggest that EMP DLAs display an elevated [O/Fe] ratio compared to their higher metallicity counterparts and this is due to their distinct enrichment histories. The elevated [O/Fe] abundance ratio could be an indicator of enrichment from a generation of metal free stars (Heger & Woosley, 2010). Further data are necessary to determine if the elevated [O/Fe] ratio of J1001+0343 is typical for an EMP DLA. Forthcoming data on other near-pristine DLAs, as part of this programme, will directly answer this question. Furthermore, upcoming surveys (e.g. WEAVE and 4MOST) will provide new EMP DLA candidates to investigate and improve the statistical significance of this behaviour. If this elevated [O/Fe] abundance ratio can be attributed to enrichment from metal-free stars, the DLAs

analysed in this work provide an ideal site to search for light from Population III SNe using the forthcoming *James Webb Space Telescope*.

CHAPTER 6

Summary

This thesis has focused on studying the chemistry of relic environments with an ultimate goal of uncovering the properties of the first stars using their surviving chemistry. Our main conclusions are as follows:

(i) In Chapter 2, we present a novel stochastic chemical enrichment model tailored to studying environments enriched by the first generation of stars. The model estimates the mass distribution of the enriching stellar population and the number of stars that have enriched a relic environment. Depending on the Population III nucleosynthetic yields adopted, we can estimate additional properties such as the typical explosion energy of their SNe and the degree of mixing between the stellar layers.

(ii) We employ this model to investigate the enrichment of the 11 most metal-poor DLAs above $z > 2.6$. We find that the chemistry of these gas clouds can be well modelled by enrichment from $N_\star < 72$ stars in the mass range $(10-40)$ $M_\odot$, with an underlying IMF that is consistent with a Salpeter distribution. Due to the similarity between the Population II and Population III yields used in this analysis, we cannot discern which population is the predominant enricher. However, given the relatively large number of enriching stars, it is likely that some DLAs in this sample have been enriched by Population II stars.

(iii) We use our stochastic chemical enrichment model to estimate the total stellar and total gas mass of a typical metal-poor DLA. We find the total stellar mass is $\log_{10}(M_\star/\mathrm{M}_\odot) = 3.5^{+0.3}_{-0.4}$ and note that this is comparable to the stellar mass content of faint Milky Way satellites (Martin et al., 2008; McConnachie, 2012). In the future, this inference might allow us to test if some of the most metal-poor DLAs are the antecedents of the UFD galaxy population.

(iv) We go on to investigate the enrichment of a sample of metal-poor Milky Way halo stars in Chapter 3. We find that the number of massive stars that have typically enriched a metal-poor halo star is $\hat{N}_\star = 5^{+13}_{-3}$. This estimate of $N_\star$ is lower than that estimated for the most metal-poor DLAs and the maximum likelihood value is more well-defined. By simultaneously considering stellar and gaseous relics, we can distinguish between their chemical enrichment histories. The investigation of stellar relics may reveal the Population III multiplicity. Using this, and the analysis of metal-poor DLAs, we can determine the typical number of minihalos that enrich early structures at $z \sim 3$ — found to be < 13 (2σ).

(v) In Chapter 4, we present the first bound on the carbon isotope ratio of a near-pristine DLA using VLT/ESPRESSO data. This bound is used to investigate possible enrichment from low mass (~ 1 $\mathrm{M}_\odot$) Population III stars. With the current bound, it is not possible to rule out enrichment from low mass Population III stars. Our analysis of the enrichment timescale of the DLA towards J0035−0918 suggests it may have experienced a hiatus in star formation following the epoch of reionisation. This result is driven by the lack of a chemical signature of low mass (< 2.4 $\mathrm{M}_\odot$) Population II stars in the chemistry of this DLA. It is also supported by the tentative relationship between [C/O] and redshift amongst the most metal-poor DLAs. The increase in [C/O] around $z \sim 3$ may be expected if we are witnessing the onset of enrichment from the first intermediate and low mass Population II stars.

(vi) In Chapter 5, we turn our attention to the empirical relationship between [O/Fe] and [Fe/H] amongst metal poor DLAs. Those with $-3 <$ [Fe/H] < -2 show a plateau in

their [O/Fe] abundance described by $[\langle O/Fe \rangle] = +0.40 \pm 0.08$. Lower metallicity DLAs show an elevated [O/Fe] abundance compared to this plateau. We present the detailed chemical abundances of two near-pristine DLAs that appear to follow this trend. If confirmed with further EMP DLAs, this would be an empirical signpost that these most metal-poor DLAs are showing a divergent chemistry at the lowest metallicities. Furthermore, this elevated [O/Fe] abundance can be explained by enrichment from a metal-free stellar population (Heger & Woosley, 2010).

Overall, the work presented in this thesis aims to highlight the wealth of information that is contained within the DLAs at the lowest metallicities. With the use of this stochastic chemical enrichment model, we can not only investigate the mass distribution of the enriching stellar population, but, also the physical properties of these DLAs that are otherwise challenging to determine. This provides an avenue to connect these high redshift relic environments to their local descendants. The combined study of gaseous and stellar relics can help distinguish between their enrichment histories and investigate the dispersion of metals in the early Universe. Furthermore, it may help to reveal the elements most useful for investigating Population III properties. The recent work by Haze Nuñez et al. (2021) highlights that a comparison of the chemistry of these VMP relics can showcase which metals in stellar atmospheres are most impacted by the stellar modelling process (i.e. RGB evolution for N and non-LTE effects for Al). Given the metal-poor stellar population in UFDs, and their possible connection to the first galaxies, a natural next step is to investigate the chemical enrichment of the stars associated with an individual UFD, for example Reticulum II (Ji et al., 2016a,b).

The enrichment model presented in this thesis can be a powerful tool to understand the enrichment of relic environments. Though, it is reliant on mapping the observed chemistry to that predicted by simulations of stellar evolution. Therefore, to reliably pin down the properties of the enriching population, we require nucleosynthetic yields with well understood uncertainties. The processes that introduce uncertainty are well studied, however, their impact on the resulting yields is less well-defined. In the future we hope to employ our enrichment model using a grid of nucleosynthetic yields with associated

uncertainties. An alternative to the nucleosynthetic yield calculations is the detection of empirical trends with metallicity and/or redshift. To investigate these relationships, we require a larger sample of EMP DLAs. Indeed, we must also aim to detect increasingly metal-poor DLAs. For example, there is yet to be a detection of a [Fe/H] < -4 DLA.

Thus far, the discovery of these low metallicity DLAs has been a relatively slow process: first requiring SDSS data, then intermediate resolution data, and finally high resolution data. This process will soon be streamlined with the advent of DESI, 4MOST and WEAVE (Dalton et al., 2012; de Jong et al., 2012; DESI Collaboration et al., 2016; Pieri et al., 2016). These surveys will scan the sky with a resolution sufficient to negate the second step of the discovery process. In fact, DESI is already collecting data. The impact of large QSO catalogues with increased spectral resolution on the detection rate of EMP DLAs is yet to be seen. It will be interesting to see how many promising candidates have been hiding in plain sight due to unfavourable low resolution data. A resolution of $\sim 60\,\mathrm{km\,s^{-1}}$ is sufficient to estimate the carbon abundance of candidate metal-poor DLAs down to [C/H] ~ -3. Thus, these catalogues will provide data of sufficient quality to efficiently identify metal-poor DLAs without the time consuming, and restrictive, step of finding targets from SDSS catalogues. The most promising candidates will then be available for follow up observations using a high resolution echelle spectrograph. Furthermore, 4MOST will survey the southern sky which, due to the lack of SDSS coverage, has been largely unexplored for metal-poor DLAs. 4MOST will observe $\sim 4 \times 10^5$ QSOs in the redshift interval $2.2 < z < 3.5$ with $r_{\mathrm{AB}} < 22.5$ (Richard et al., 2019). This is $\sim 1.3\times$ more than the number of quasars contained in the SDSS BOSS DR12 quasar catalogue (Alam et al., 2015). With these data, we would therefore expect to *at least* double the number of known EMP DLAs. Once these surveys start collecting data, there will be an influx of unexplored metal-poor DLA candidates. As such, it is almost serendipitous that the first 30+ m telescopes, like the ELT, are expected to collect light in 2027. Given the increased power of these telescopes, we will be able to detect EMP DLAs in the foreground of fainter quasars. This will allow us to study a currently inaccessible sample of EMP DLA candidates. Furthermore, we will also be able to detect absorption features from elements

that are too weak to detect in the most metal-poor DLAs with current instruments. In the future, we expect to detect Ni and Zn (in addition to Ar and Ti and Cr). These elements are invaluable when it comes to diagnosing the explosion mechanism of Population III SNe. With these data we will therefore be able to conduct a more thorough investigation into the end stages of the lives of the first stars.

In addition to this, we are awaiting the imminent launch of the James Webb Space Telescope (JWST) at the end of this calendar year. JWST will revolutionise our ability to investigate the first galaxies and their stellar populations at $z > 10$. The luminosity and number abundance of these detected galaxies will depend sensitively on the metallicity, age, and IMF of their constituent stars (Bromm & Yoshida, 2011). Thus, studying these galaxies will help reveal the properties of the earliest stellar populations. With these new instruments at our disposal, it is the optimum time to be researching the 'last frontier of observational cosmology'.

APPENDIX A

DLA enrichment model

A.1 Further models

In this Appendix, we explore the sensitivity of our model parameter inferences to the adopted nucleosynthesis yield calculation (see also, Section 2.5). We first consider the yields of massive Population II ($Z = 10^{-4}$ $Z_{\odot}$) stars reported by WW95. These yields have been calculated for a typical explosion energy of 1.2×10^{51} erg. We therefore only consider three model parameters: α, $N_{\star}$, and $M_{\rm max}$. The maximum mass considered by the WW95 yields is $M_{\rm max} = 40$ $M_{\odot}$. We repeat the analysis described in Section 2.4 to find the enrichment model that best describes the abundance ratios observed in the most metal-poor DLAs. We also repeat our analysis considering the model yield calculations of massive metal-free stars reported by LC12. These yields have been calculated for a typical explosion energy of $\sim 10^{51}$ erg. In Figure A.1, we show the maximum likelihood enrichment models (blue PDF) based on each of the above yield sets, and compare these to the observed data. From this we can see that the enrichment model indicated by the HW10 yields produces the best overall fit to the observed data. This, alongside the fine mass resolution and the detailed consideration of the explosion energy afforded by the HW10 yields, reaffirms our choice to use this yield set in our fiducial analysis.

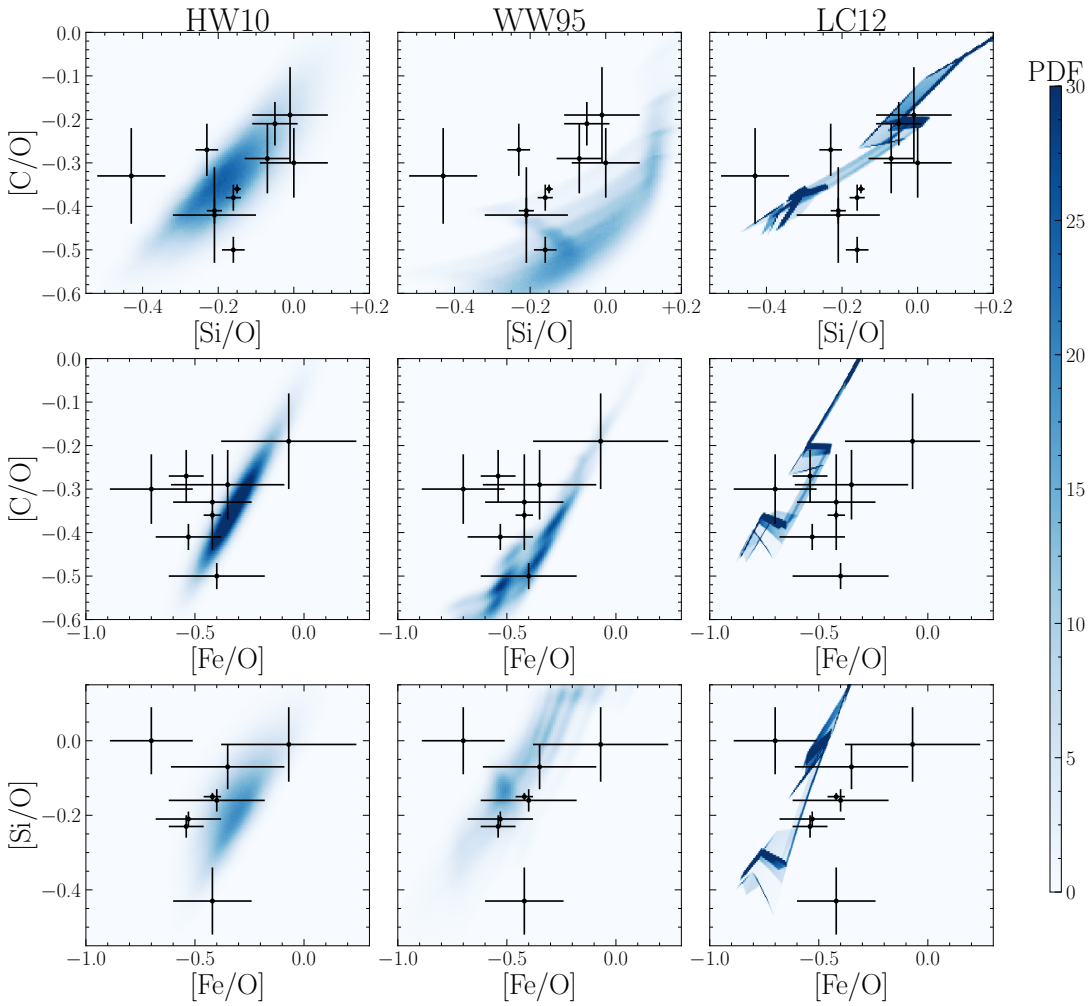

Figure A.1. The observed abundance ratios of the most metal-poor DLAs (black symbols with errors) are overplotted on the maximum likelihood parameter distribution ($p(R_i|R_m)$; blue background PDF) based on three yield sets. Each column corresponds to a different yield set. From left to right, the underlying yields correspond to: HW10 (fiducial yield choice), WW95, and LC12. Each panel showcases the joint probability density of two expected abundance ratios, given the maximum likelihood enrichment model parameters for a given yield set. The combined inspection of each column gives an indication of $p(R_i|R_m)$, and the ability of a given yield set to simultaneously reproduce the [C/O], [Si/O], and [Fe/O] abundance ratios observed within the metal-poor DLA population.

APPENDIX B

Stellar enrichment model

B.1 Intrinsic scatter calculation

In this appendix, we describe our approach to estimate the intrinsic scatter of the stellar samples. This scatter is defined by Eq. 3.3.1. As described in Section 3.3, we consider two model parameters ($[X/Fe]_{cent}$ and σ_{int}) that we determine independently for each abundance ratio and each sample. We use an MCMC procedure to simultaneously estimate the central values $[Mg/Fe]_{cent}$, $[Ca/Fe]_{cent}$, and $[Ni/Fe]_{cent}$ of a sample, alongside their associated additional error components $\sigma_{int,Mg}$, $\sigma_{int,Ca}$, and $\sigma_{int,Ni}$. We adopt uniform priors for these parameters; the central values are bounded by $-5 \leq [X/Fe]_{cent} \leq 5$ and the intrinsic errors are bounded by $0 \leq \sigma_{int,X} \leq 5$. We utilised the EMCEE software package (Foreman-Mackey et al., 2013) to randomly initialise 400 walkers and explore this parameter space. The results of this analysis for the C04 data are presented in Figure B.1 which shows the converged posterior distributions of these model parameters. The confidence interval for [Mg/Fe] demonstrates there is a statistically significant deviation from 0; this result is replicated across all of the stellar samples. We consider the possibility that this intrinsic dispersion is the result of stochastic sampling of the IMF.

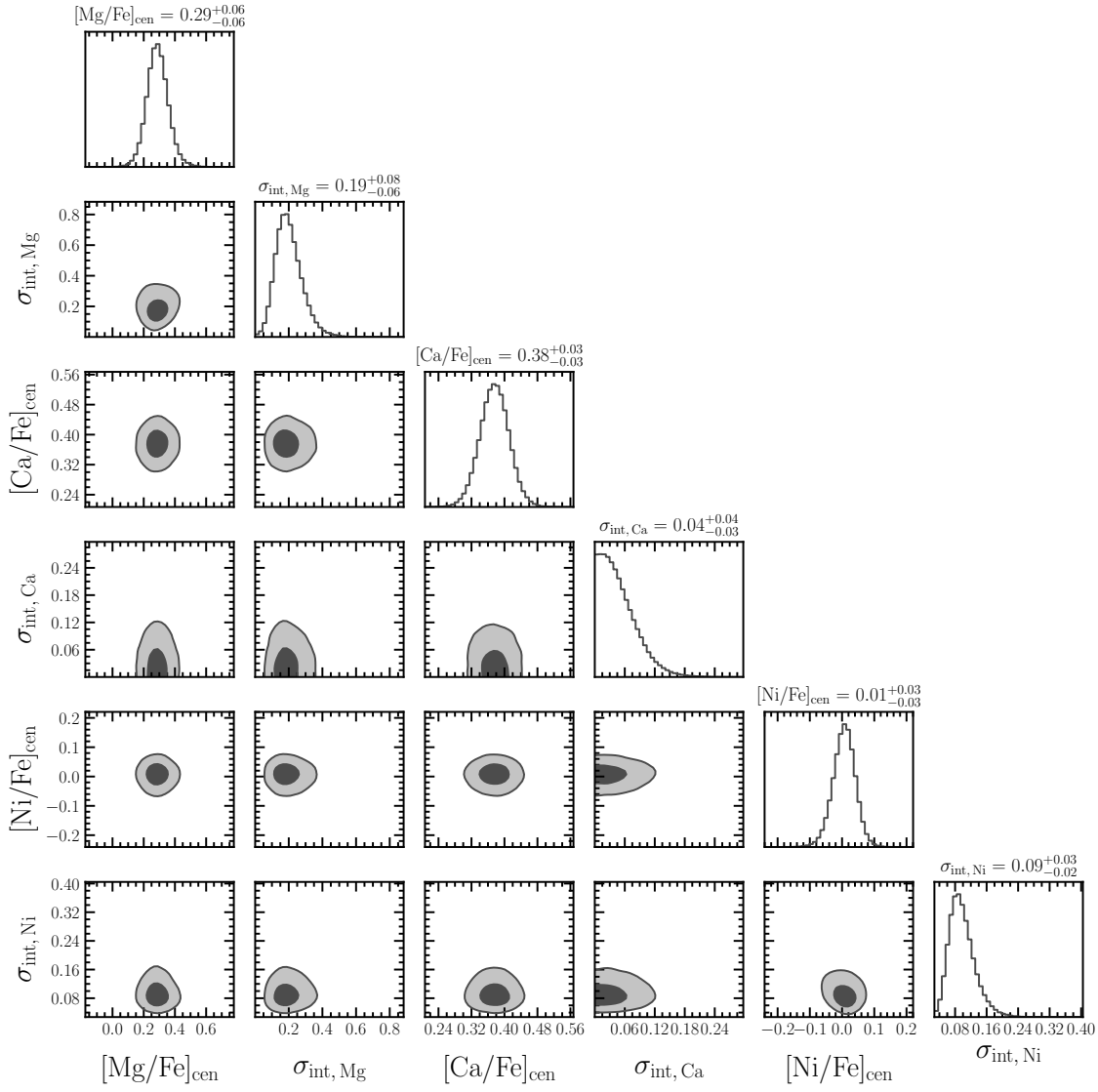

Figure B.1. Converged MCMC analysis of the intrinsic scatter of the C04 data. The main diagonal panels show the marginalised maximum likelihood distributions of the parameters describing the central values and intrinsic dispersions of the C04 data (refer to Section 3.3). The associated contours highlight their associated 2D projections. The dark and light contours show the 68% and 95% confidence regions of these projections, respectively.

B.2 Analysis of the corrected R14 sample

In this appendix, we show the results of repeating our analysis using the offset corrected R14 data in combination with the C04, B09, and Y13 data. We use the abundances of the stars that appear in multiple surveys to calculate the [Mg/Ca] and [Ni/Fe] offsets of 0.14 ± 0.07 and 0.05 ± 0.13 respectively. The confidence intervals are estimated using the median absolute deviation; for normally distributed data, $\sigma \simeq 1.4826\,\mathrm{MAD}$. When applying this correction, the errors associated with the R14 [Mg/Ca] and [Ni/Fe] abundances are given by the reported observational errors and these additional systematic components added in quadrature. Figure B.2 shows the parameter estimates that result from considering this modified sample (grey distributions). Unlike those produced using the original data (see Figure 3.6), these estimates are consistent with those found using the reduced sample (blue distributions in Figure B.2). Given that we have calibrated the R14 data using a substantial portion of the stars within the reduced sample, this agreement is reassuring. We note that the original discrepancies between the sample distributions are invaluable for testing the sensitivity of our model to the input data.

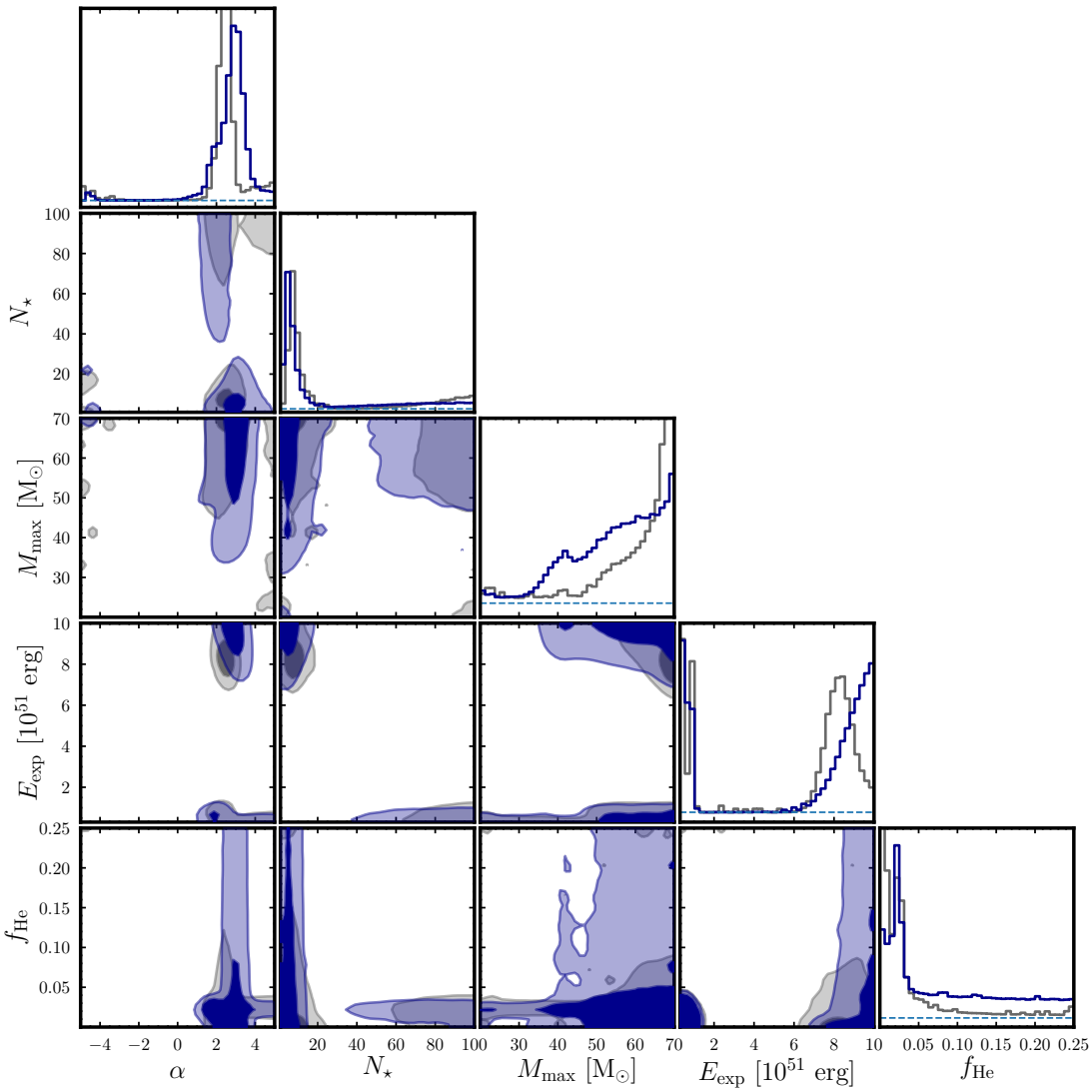

Figure B.2. Same as Figure 3.6 using the offset corrected R14 [Mg/Ca] and [Ni/Fe] data in place of the original values.

APPENDIX C

DLA [O/Fe] data

C.1 DLA [O/Fe] abundances

In this appendix, we present the DLA data used to produce Figure 5.5. In Table C.1 we list the column density of neutral hydrogen, the redshift, and the relative abundances of O and Fe.

Table C.1. DLA data used in Figure 5.5

QSO	$z_{\rm abs}$	$\log_{10} N({\rm H\,I})$	[Fe/H]	[O/Fe]	References
Q0000−2620	3.390	21.41 ± 0.08	−2.01 ± 0.09	+0.33 ± 0.10	1
J0034+1639	4.251	20.60 ± 0.10	−2.84 ± 0.12	+0.33 ± 0.08	2
J0035−0819	2.340	20.43 ± 0.04	−2.89 ± 0.05	+0.44 ± 0.06	3, 4, 5
HS0105+1619	2.537	19.42 ± 0.01	−1.98 ± 0.09	+0.22 ± 0.09	6
Q0112−306	2.418	20.50 ± 0.08	−2.64 ± 0.09	+0.40 ± 0.09	7
J0140−0839	3.697	20.75 ± 0.15	−3.45 ± 0.24	+0.70 ± 0.19	3, 8
J0307−4945	4.467	20.67 ± 0.09	−1.93 ± 0.19	+0.48 ± 0.24	9
J0311−1722	3.734	20.30 ± 0.06	< -2.01	> -0.28	3
J0831+3358	2.304	20.25 ± 0.15	−2.39 ± 0.16	+0.38 ± 0.08	3, 10
J0903+2628	3.078	20.32 ± 0.05	≤ -2.81	> -0.24	11
Q0913+072	2.618	20.34 ± 0.04	−2.82 ± 0.04	+0.42 ± 0.01	12
J0953−0504	4.203	20.55 ± 0.10	−2.95 ± 0.21	+0.40 ± 0.19	13
J0955+4116	3.280	20.24 ± 0.05	−2.99 ± 0.10	+0.50 ± 0.10	10, 14
J1001+0343	3.078	20.20 ± 0.05	−3.25 ± 0.07	+0.62 ± 0.05	3, 14
J1037+0139	2.705	20.50 ± 0.08	−2.44 ± 0.08	+0.31 ± 0.04	3
Q1108−077	3.608	20.37 ± 0.07	−1.96 ± 0.07	+0.27 ± 0.04	7
J1111+1332	2.271	20.39 ± 0.04	−2.27 ± 0.04	+0.35 ± 0.07	15
Q1202+3235	4.977	19.83 ± 0.10	−2.44 ± 0.16	+0.42 ± 0.14	16
J1340+1106	2.508	20.09 ± 0.05	−2.07 ± 0.05	+0.31 ± 0.04	3
J1340+1106	2.796	21.00 ± 0.06	−2.15 ± 0.06	+0.50 ± 0.04	3
J1358+0349	2.853	20.16 ± 0.02	−3.32 ± 0.18	+0.70 ± 0.18	17
J1358+6522	3.067	20.50 ± 0.08	−2.88 ± 0.08	+0.54 ± 0.03	17
J1419+0829	3.050	20.40 ± 0.03	−2.33 ± 0.04	+0.41 ± 0.04	3
J1558−0031	2.703	20.67 ± 0.05	−1.95 ± 0.05	+0.38 ± 0.04	18
J1558+4053	2.553	20.30 ± 0.04	−2.70 ± 0.07	+0.25 ± 0.07	12
Q1946+7658	2.844	20.27 ± 0.06	−2.50 ± 0.06	+0.36 ± 0.01	19
Q2059−360	3.083	20.98 ± 0.08	−1.97 ± 0.08	+0.39 ± 0.04	7
J2155+1358	4.212	19.61 ± 0.10	−2.15 ± 0.25	+0.35 ± 0.24	20
Q2206−199	2.076	20.43 ± 0.04	−2.57 ± 0.04	+0.50 ± 0.03	12

1) Molaro et al. (2000); 2) Berg et al. (2016); 3) Cooke et al. (2011b); 4) Cooke et al. (2011a); 5) Welsh et al. (2020); 6) O'Meara et al. (2001); 7) Petitjean et al. (2008), 8) Ellison et al. (2010); 9) Dessauges-Zavadsky et al. (2001); 10) Penprase et al. (2010); 11) Cooke et al. (2017); 12) Pettini et al. (2008); 13) Dutta et al. (2014); 14) This work; 15) Cooke et al. (2015); 16) Morrison et al. (2016); 17) Cooke et al. (2016); 18) O'Meara et al. (2006); 19) Prochaska et al. (2002); 20) Dessauges-Zavadsky et al. (2003).

Bibliography

Abel T., Anninos P., Norman M. L., Zhang Y., 1998, ApJ, 508, 518

Abel T., Bryan G. L., Norman M. L., 2000, ApJ, 540, 39

Abel T., Bryan G. L., Norman M. L., 2002, Science, 295, 93

Abohalima A., Frebel A., 2018, ApJs, 238, 36

Adams S. M., Kochanek C. S., Gerke J. R., Stanek K. Z., Dai X., 2017, Mon. Not. Roy. Astron. Soc., 468, 4968

Aguado D. S., Allende Prieto C., González Hernández J. I., Carrera R., Rebolo R., Shetrone M., Lambert D. L., Fernández-Alvar E., 2016, A&A, 593, A10

Akerman C. J., Carigi L., Nissen P. E., Pettini M., Asplund M., 2004, A&A, 414, 931

Akerman C. J., Ellison S. L., Pettini M., Steidel C. C., 2005, A&A, 440, 499

Alam S., et al., 2015, ApJ Sup., 219, 12

Allende Prieto C., et al., 2015, A&A, 579, A98

Alvarez M. A., Wise J. H., Abel T., 2009, ApJl, 701, L133

An Z.-D., Ma Y.-G., Fan G.-T., Li Y.-J., Chen Z.-P., Sun Y.-Y., 2016, ApJl, 817, L5

Andrievsky S. M., Spite M., Korotin S. A., Spite F., Bonifacio P., Cayrel R., François P., Hill V., 2010, A&A, 509, A88

Aoki W., et al., 2006, ApJ, 639, 897

Aoki W., et al., 2013, AJ, 145, 13

Aoki W., Tominaga N., Beers T. C., Honda S., Lee Y. S., 2014, Science, 345, 912

Asplund M., 2005, ARA&A, 43, 481

Asplund M., Grevesse N., Sauval A. J., Scott P., 2009, ARA&A, 47, 481

Bañados E., et al., 2019, ApJ, 885, 59

Barkana R., Loeb A., 2001, Physics Reports, 349, 125

Bastian N., Covey K. R., Meyer M. R., 2010, ARA&A, 48, 339

Becker G. D., Sargent W. L. W., Rauch M., Calverley A. P., 2011, ApJ, 735, 93

Beers T. C., Carollo D., 2008, in O'Shea B. W., Heger A., eds, American Institute of Physics Conference Series Vol. 990, First Stars III. pp 104–108 (arXiv:0804.1993), doi:10.1063/1.2905513

Beers T. C., Christlieb N., 2005, ARA&A, 43, 531

Beers T. C., Preston G. W., Shectman S. A., 1985, AJ, 90, 2089

Beers T. C., Preston G. W., Shectman S. A., 1992, AJ, 103, 1987

Berengut J. C., Dzuba V. A., Flambaum V. V., King J. A., Kozlov M. G., Murphy M. T., Webb J. K., 2011, Astrophysics and Space Science Proceedings, 22, 9

Berg T. A. M., Ellison S. L., Prochaska J. X., Venn K. A., Dessauges-Zavadsky M., 2015, MNRAS, 452, 4326

Berg T. A. M., et al., 2016, MNRAS, 463, 3021

Béthermin M., et al., 2018, A&A, 620, A115

Bond H. E., 1980, The Astrophysical Journal Supplement Series, 44, 517

Bonifacio P., et al., 2009, A&A, 501, 519

Bowman J. D., Rogers A. E. E., Monsalve R. A., Mozdzen T. J., Mahesh N., 2018, Nature, 555, 67

Brauer K., Ji A. P., Drout M. R., Frebel A., 2021, ApJ, 915, 81

Bromm V., Yoshida N., 2011, ARA&A, 49, 373

Bromm V., Coppi P. S., Larson R. B., 1999, ApJl, 527, L5

Bromm V., Coppi P. S., Larson R. B., 2002, ApJ, 564, 23

Bromm V., Yoshida N., Hernquist L., 2003, ApJl, 596, L135

Bromm V., Yoshida N., Hernquist L., McKee C. F., 2009, Nature, 459, 49

Brown T. M., et al., 2014, ApJ, 796, 91

Bullock J. S., Kravtsov A. V., Weinberg D. H., 2000, ApJ, 539, 517

Burrows A., Radice D., Vartanyan D., 2019, arXiv e-prints, p. arXiv:1902.00547

Caffau E., et al., 2013, A&A, 560, A71

Campbell S. W., Lattanzio J. C., 2008, A&A, 490, 769

Carswell R. F., Becker G. D., Jorgenson R. A., Murphy M. T., Wolfe A. M., 2012, MNRAS, 422, 1700

Cayrel R., et al., 2004, A&A, 416, 1117

Cescutti G., Matteucci F., McWilliam A., Chiappini C., 2009, A&A, 505, 605

Chabrier G., 2003, PASP, 115, 763

Chieffi A., Limongi M., 2004, ApJ, 608, 405

Christensen L., Møller P., Fynbo J. P. U., Zafar T., 2014, MNRAS, 445, 225

Christlieb N., et al., 2002, Nature, 419, 904

Christlieb N., Gustafsson B., Korn A. J., Barklem P. S., Beers T. C., Bessell M. S., Karlsson T., Mizuno-Wiedner M., 2004, ApJ, 603, 708

Christlieb N., Schörck T., Frebel A., Beers T. C., Wisotzki L., Reimers D., 2008, A&A, 484, 721

Clark P. C., Glover S. C. O., Klessen R. S., 2008, ApJ, 672, 757

Clark P. C., Glover S. C. O., Klessen R. S., Bromm V., 2011, ApJ, 727, 110

Cooke R., Pettini M., Steidel C. C., Rudie G. C., Jorgenson R. A., 2011a, MNRAS, 412, 1047

Cooke R., Pettini M., Steidel C. C., Rudie G. C., Nissen P. E., 2011b, MNRAS, 417, 1534

Cooke R., Pettini M., Murphy M. T., 2012, MNRAS, 425, 347

Cooke R. J., Pettini M., Jorgenson R. A., Murphy M. T., Steidel C. C., 2014, ApJ, 781, 31

Cooke R. J., Pettini M., Jorgenson R. A., 2015, ApJ, 800, 12

Cooke R. J., Pettini M., Nollett K. M., Jorgenson R., 2016, ApJ, 830, 148

Cooke R. J., Pettini M., Steidel C. C., 2017, MNRAS, 467, 802

Cooke R. J., Pettini M., Steidel C. C., 2018, The Astrophysical Journal, 855, 102

Crighton N. H. M., O'Meara J. M., Murphy M. T., 2016, MNRAS, 457, L44

DESI Collaboration et al., 2016, arXiv e-prints, p. arXiv:1611.00036

Da Costa G. S., et al., 2019, MNRAS, 489, 5900

Dalton G., et al., 2012, in McLean I. S., Ramsay S. K., Takami H., eds, Society of Photo-Optical Instrumentation Engineers (SPIE) Conference Series Vol. 8446, Ground-based and Airborne Instrumentation for Astronomy IV. p. 84460P, doi:10.1117/12.925950

Dekker H., D'Odorico S., Kaufer A., Delabre B., Kotzlowski H., 2000, in Iye M., Moorwood A. F., eds, Vol. 4008, Optical and IR Telescope Instrumentation and Detectors. pp 534–545, doi:10.1117/12.395512

Dessauges-Zavadsky M., D'Odorico S., McMahon R. G., Molaro P., Ledoux C., Péroux C., Storrie-Lombardi L. J., 2001, A&A, 370, 426

Dessauges-Zavadsky M., Péroux C., Kim T.-S., D'Odorico S., McMahon R. G., 2003, MNRAS, 345, 447

Di Matteo P., Spite M., Haywood M., Bonifacio P., Gómez A., Spite F., Caffau E., 2020, A&A, 636, A115

Dutta R., Srianand R., Rahmani H., Petitjean P., Noterdaeme P., Ledoux C., 2014, MNRAS, 440, 307

Ekström S., Meynet G., Chiappini C., Hirschi R., Maeder A., 2008, A&A, 489, 685

Ellison S. L., Prochaska J. X., Hennawi J., Lopez S., Usher C., Wolfe A. M., Russell D. M., Benn C. R., 2010, MNRAS, 406, 1435

Erni P., Richter P., Ledoux C., Petitjean P., 2006, A&A, 451, 19

Ezzeddine R., Sitnova T., Frebel A., Mashonkina L., Plez B., 2018, in Chiappini C., Minchev I., Starkenburg E., Valentini M., eds, IAU Symposium Vol. 334, Rediscovering Our Galaxy. pp 259–262, doi:10.1017/S1743921317007177

Ezzeddine R., et al., 2019, ApJ, 876, 97

Fabbian D., Asplund M., Barklem P. S., Carlsson M., Kiselman D., 2009, A&A, 500, 1221

Field G. B., Steigman G., 1971, ApJ, 166, 59

Foreman-Mackey D., 2016, The Journal of Open Source Software, 1, 24

Foreman-Mackey D., Hogg D. W., Lang D., Goodman J., 2013, PASP, 125, 306

Fraser M., Casey A. R., Gilmore G., Heger A., Chan C., 2017, MNRAS, 468, 418

Frebel A., 2010, Astronomische Nachrichten, 331, 474

Frebel A., Norris J. E., 2015, ARA&A, 53, 631

Frebel A., et al., 2005, Nature, 434, 871

Frebel A., Chiti A., Ji A. P., Jacobson H. R., Placco V. M., 2015, ApJl, 810, L27

Fumagalli M., O'Meara J. M., Prochaska J. X., 2011, Science, 334, 1245

Fumagalli M., O'Meara J. M., Prochaska J. X., Rafelski M., Kanekar N., 2015, MNRAS, 446, 3178

Fumagalli M., et al., 2017, MNRAS, 471, 3686

Fynbo J. P. U., et al., 2010, MNRAS, 408, 2128

García Pérez A. E., Asplund M., Primas F., Nissen P. E., Gustafsson B., 2006, A&A, 451, 621

Gerke J. R., Kochanek C. S., Stanek K. Z., 2015, MNRAS, 450, 3289

Glover S., 2013, in Wiklind T., Mobasher B., Bromm V., eds, Astrophysics and Space Science Library Vol. 396, The First Galaxies. p. 103 (arXiv:1209.2509), doi:10.1007/978-3-642-32362-1_3

Greif T. H., Johnson J. L., Bromm V., Klessen R. S., 2007, ApJ, 670, 1

Greif T. H., Glover S. C. O., Bromm V., Klessen R. S., 2010, ApJ, 716, 510

Greif T. H., White S. D. M., Klessen R. S., Springel V., 2011, ApJ, 736, 147

Greif T. H., Bromm V., Clark P. C., Glover S. C. O., Smith R. J., Klessen R. S., Yoshida N., Springel V., 2012, MNRAS, 424, 399

Grimmett J. J., Heger A., Karakas A. I., Müller B., 2018, MNRAS,

Haehnelt M. G., Steinmetz M., Rauch M., 1998, ApJ, 495, 647

Hartwig T., Yoshida N., 2019, ApJl, 870, L3

Hartwig T., Ishigaki M. N., Klessen R. S., Yoshida N., 2018a, MNRAS,

Hartwig T., et al., 2018b, MNRAS, 478, 1795

Haze Nuñez E., Kirby E. N., Steidel C. C., 2021, arXiv e-prints, p. arXiv:2108.00659

Heger A., Woosley S. E., 2002, ApJ, 567, 532

Heger A., Woosley S. E., 2010, ApJ, 724, 341

Heger A., Fryer C. L., Woosley S. E., Langer N., Hartmann D. H., 2003, ApJ, 591, 288

Hendricks B., Koch A., Lanfranchi G. A., Boeche C., Walker M., Johnson C. I., Peñarrubia J., Gilmore G., 2014, ApJ, 785, 102

Henry R. B. C., Edmunds M. G., Köppen J., 2000, ApJ, 541, 660

Hill V., et al., 2018, arXiv e-prints, p. arXiv:1812.01486

Hirano S., Hosokawa T., Yoshida N., Umeda H., Omukai K., Chiaki G., Yorke H. W., 2014, ApJ, 781, 60

Höfner S., Olofsson H., 2018, A&Ar, 26, 1

Howes L. M., et al., 2016, MNRAS, 460, 884

Iben I. J., 1975, ApJ, 196, 525

Ishigaki M. N., Tominaga N., Kobayashi C., Nomoto K., 2018, ApJ, 857, 46

Jeon M., Bromm V., Pawlik A. H., Milosavljević M., 2015, MNRAS, 452, 1152

Jeon M., Besla G., Bromm V., 2019, ApJ, 878, 98

Ji A. P., Frebel A., Bromm V., 2015, MNRAS, 454, 659

Ji A. P., Frebel A., Chiti A., Simon J. D., 2016a, Nature, 531, 610

Ji A. P., Frebel A., Simon J. D., Chiti A., 2016b, ApJ, 830, 93

Joggerst C. C., Almgren A., Bell J., Heger A., Whalen D., Woosley S. E., 2010a, ApJ, 709, 11

Joggerst C. C., Almgren A., Woosley S. E., 2010b, ApJ, 723, 353

Johnson J. L., Bromm V., 2007, MNRAS, 374, 1557

Jorgenson R. A., Murphy M. T., Thompson R., 2013, MNRAS, 435, 482

Joshi R., et al., 2021, ApJ, 908, 129

Karakas A. I., 2010, MNRAS, 403, 1413

Karakas A. I., 2014, MNRAS, 445, 347

Karakas A., Lattanzio J. C., 2007, PASA, 24, 103

Karakas A. I., Lattanzio J. C., 2014, PASA, 31, e030

Karlsson T., 2005, A&A, 439, 93

Karlsson T., Gustafsson B., 2005, A&A, 436, 879

Keller S. C., et al., 2007, PASA, 24, 1

Keller S. C., et al., 2014, Nature, 506, 463

Kitayama T., Yoshida N., Susa H., Umemura M., 2004, ApJ, 613, 631

Klitsch A., Péroux C., Zwaan M. A., De Cia A., Ledoux C., Lopez S., 2021, MNRAS, 506, 514

Kochanek C. S., Beacom J. F., Kistler M. D., Prieto J. L., Stanek K. Z., Thompson T. A., Yüksel H., 2008, ApJ, 684, 1336

Kotuš S. M., Murphy M. T., Carswell R. F., 2017, MNRAS, 464, 3679

Krogager J. K., Møller P., Fynbo J. P. U., Noterdaeme P., 2017, MNRAS, 469, 2959

Kroupa P., 2001, MNRAS, 322, 231

Kulkarni V. P., Hill J. M., Schneider G., Weymann R. J., Storrie-Lombardi L. J., Rieke M. J., Thompson R. I., Jannuzi B. T., 2000, ApJ, 536, 36

Ledoux C., Petitjean P., Fynbo J. P. U., Møller P., Srianand R., 2006, A&A, 457, 71

Lehner N., O'Meara J. M., Howk J. C., Prochaska J. X., Fumagalli M., 2016, ApJ, 833, 283

Lehner N., Wotta C. B., Howk J. C., O'Meara J. M., Oppenheimer B. D., Cooksey K. L., 2019, ApJ, 887, 5

Levshakov S. A., Centurión M., Molaro P., Kostina M. V., 2006, A&A, 447, L21

Li H.-N., Zhao G., Christlieb N., Wang L., Wang W., Zhang Y., Hou Y., Yuan H., 2015, ApJ, 798, 110

Limongi M., Chieffi A., 2012, The Astrophysical Journal Supplement Series, 199, 38

Mackenzie R., et al., 2019, MNRAS, 487, 5070

Martin N. F., de Jong J. T. A., Rix H.-W., 2008, ApJ, 684, 1075

Matteucci F., 2003, A&SS, 284, 539

Matteucci F., Brocato E., 1990, ApJ, 365, 539

McConnachie A. W., 2012, AJ, 144, 4

McWilliam A., 1997, ARA&A, 35, 503

McWilliam A., Searle L., 1999, A&SS, 265, 133

McWilliam A., Preston G. W., Sneden C., Shectman S., 1995, AJ, 109, 2736

Melson T., Janka H.-T., Marek A., 2015, ApJl, 801, L24

Meynet G., Ekström S., Maeder A., 2006, A&A, 447, 623

Meynet G., Hirschi R., Ekstrom S., Maeder A., Georgy C., Eggenberger P., Chiappini C., 2010, A&A, 521, A30

Mihalas D., 1978, Stellar atmospheres

Molaro P., Bonifacio P., Centurión M., D'Odorico S., Vladilo G., Santin P., Di Marcantonio P., 2000, ApJ, 541, 54

Møller P., et al., 2018, MNRAS, 474, 4039

Morrison S., Kulkarni V. P., Som D., DeMarcy B., Quiret S., Péroux C., 2016, ApJ, 830, 158

Morton D. C., 2003, ApJs, 149, 205

Müller B., 2019, Annual Review of Nuclear and Particle Science, 69, annurev

Müller B., 2020, Living Reviews in Computational Astrophysics, 6, 3

Müller B., Heger A., Liptai D., Cameron J. B., 2016, MNRAS, 460, 742

Müller B., et al., 2019, MNRAS, 484, 3307

Murphy M. T., Berengut J. C., 2014, MNRAS, 438, 388

Murphy M. T., Cooksey K. L., 2017, MNRAS, 471, 4930

Murphy M. T., Curran S. J., Webb J. K., Ménager H., Zych B. J., 2007, MNRAS, 376, 673

Naoz S., Yoshida N., Gnedin N. Y., 2012, ApJ, 747, 128

Neeleman M., Wolfe A. M., Prochaska J. X., Rafelski M., 2013, ApJ, 769, 54

Neeleman M., Kanekar N., Prochaska J. X., Christensen L., Dessauges-Zavadsky M., Fynbo J. P. U., Møller P., Zwaan M. A., 2018, ApJl, 856, L12

Nissen P. E., Primas F., Asplund M., Lambert D. L., 2002, A&A, 390, 235

Nomoto K., Kobayashi C., Tominaga N., 2013, ARA&A, 51, 457

Nordlander T., et al., 2019, MNRAS, 488, L109

Noterdaeme P., et al., 2021, arXiv e-prints, p. arXiv:2105.00697

Oñorbe J., Boylan-Kolchin M., Bullock J. S., Hopkins P. F., Kereš D., Faucher-Giguère C.-A., Quataert E., Murray N., 2015, MNRAS, 454, 2092

O'Meara J. M., Tytler D., Kirkman D., Suzuki N., Prochaska J. X., Lubin D., Wolfe A. M., 2001, ApJ, 552, 718

O'Meara J. M., Burles S., Prochaska J. X., Prochter G. E., Bernstein R. A., Burgess K. M., 2006, ApJl, 649, L61

Penprase B. E., Prochaska J. X., Sargent W. L. W., Toro-Martinez I., Beeler D. J., 2010, ApJ, 721, 1

Pepe F. A., et al., 2010, in Ground-based and Airborne Instrumentation for Astronomy III. p. 77350F, doi:10.1117/12.857122

Péroux C., McMahon R. G., Storrie-Lombardi L. J., Irwin M. J., 2003, MNRAS, 346, 1103

Péroux C., Bouché N., Kulkarni V. P., York D. G., Vladilo G., 2011, MNRAS, 410, 2251

Péroux C., Bouché N., Kulkarni V. P., York D. G., Vladilo G., 2012, MNRAS, 419, 3060

Petitjean P., Ledoux C., Srianand R., 2008, A&A, 480, 349

Pettini M., Smith L. J., Hunstead R. W., King D. L., 1994, ApJ, 426, 79

Pettini M., King D. L., Smith L. J., Hunstead R. W., 1997, ApJ, 478, 536

Pettini M., Zych B. J., Steidel C. C., Chaffee F. H., 2008, MNRAS, 385, 2011

Pieri M. M., et al., 2016, in Reylé C., Richard J., Cambrésy L., Deleuil M., Pécontal E., Tresse L., Vauglin I., eds, SF2A-2016: Proceedings of the Annual meeting of the French Society of Astronomy and Astrophysics. pp 259–266 (arXiv:1611.09388)

Pitrou C., Coc A., Uzan J.-P., Vangioni E., 2018, Physics Reports, 754, 1

Placco V. M., et al., 2016, ApJ, 833, 21

Planck Collaboration et al., 2018, arXiv e-prints, p. arXiv:1807.06209

Planck Collaboration et al., 2020, A&A, 641, A7

Prantzos N., Aubert O., Audouze J., 1996, A&A, 309, 760

Primas F., Brugamyer E., Sneden C., King J. R., Beers T. C., Boesgaard A. M., Deliyannis C. P., 2000, in Weiss A., Abel T. G., Hill V., eds, The First Stars. p. 51, doi:10.1007/10719504_7

Prochaska J. X., Howk J. C., O'Meara J. M., Tytler D., Wolfe A. M., Kirkman D., Lubin D., Suzuki N., 2002, ApJ, 571, 693

Prochaska J. X., Gawiser E., Wolfe A. M., Castro S., Djorgovski S. G., 2003, ApJl, 595, L9

Prochaska J. X., Herbert-Fort S., Wolfe A. M., 2005, ApJ, 635, 123

Prochaska J. X., Chen H.-W., Wolfe A. M., Dessauges-Zavadsky M., Bloom J. S., 2008, ApJ, 672, 59

Quiret S., et al., 2016, MNRAS, 458, 4074

Rafelski M., Wolfe A. M., Prochaska J. X., Neeleman M., Mendez A. J., 2012, ApJ, 755, 89

Rafelski M., Neeleman M., Fumagalli M., Wolfe A. M., Prochaska J. X., 2014, ApJ, 782, L29

Ranjan A., Noterdaeme P., Krogager J. K., Petitjean P., Srianand R., Balashev S. A., Gupta N., Ledoux C., 2020, A&A, 633, A125

Reynolds T. M., Fraser M., Gilmore G., 2015, MNRAS, 453, 2885

Richard J., et al., 2019, The Messenger, 175, 50

Ritter J. S., Sluder A., Safranek-Shrader C., Milosavljević M., Bromm V., 2015, MNRAS, 451, 1190

Robert P. F., Murphy M. T., O'Meara J. M., Crighton N. H. M., Fumagalli M., 2019, MNRAS, 483, 2736

Roederer I. U., Preston G. W., Thompson I. B., Shectman S. A., Sneden C., Burley G. S., Kelson D. D., 2014, AJ, 147, 136

Romano D., Karakas A. I., Tosi M., Matteucci F., 2010, A&A, 522, A32

Ryan S. G., Norris J. E., Bessell M. S., 1991, AJ, 102, 303

Ryan S. G., Norris J. E., Beers T. C., 1996, ApJ, 471, 254

Salpeter E. E., 1955, ApJ, 121, 161

Salvadori S., Ferrara A., Schneider R., Scannapieco E., Kawata D., 2010, MNRAS, 401, L5

Sarmento R., Scannapieco E., Pan L., 2017, ApJ, 834, 23

Saslaw W. C., Zipoy D., 1967, Nature, 216, 976

Savage B. D., Sembach K. R., 1996, ApJ, 470, 893

Sitnova T. M., Mashonkina L. I., Ezzeddine R., Frebel A., 2019, MNRAS, 485, 3527

Skúladóttir Á., Salvadori S., Pettini M., Tolstoy E., Hill V., 2018, A&A, 615, A137

Skúladóttir Á., et al., 2021, arXiv e-prints, p. arXiv:2106.11592

Spitzer L. J., Jenkins E. B., 1975, Annual Review of Astronomy and Astrophysics, 13, 133

Srianand R., Gupta N., Petitjean P., Noterdaeme P., Ledoux C., 2010, MNRAS, 405, 1888

Stacy A., Bromm V., 2014, ApJ, 785, 73

Stacy A., Greif T. H., Bromm V., 2010, MNRAS, 403, 45

Stacy A., Bromm V., Lee A. T., 2016, MNRAS, 462, 1307

Starkenburg E., et al., 2013, A&A, 549, A88

Starkenburg E., et al., 2017, MNRAS, 471, 2587

Suda T., et al., 2008, PASJ, 60, 1159

Suda T., Yamada S., Katsuta Y., Komiya Y., Ishizuka C., Aoki W., Fujimoto M. Y., 2011, MNRAS, 412, 843

Suda T., et al., 2017, PASJ, 69, 76

Sukhbold T., Adams S., 2019, arXiv e-prints,

Sukhbold T., Ertl T., Woosley S. E., Brown J. M., Janka H.-T., 2016, ApJ, 821, 38

Sukhbold T., Woosley S. E., Heger A., 2018, ApJ, 860, 93

Susa H., Hasegawa K., Tominaga N., 2014, ApJ, 792, 32

Tarumi Y., Hartwig T., Magg M., 2020, arXiv e-prints, p. arXiv:2005.10401

Tegmark M., Silk J., Rees M. J., Blanchard A., Abel T., Palla F., 1997, ApJ, 474, 1

Thévenin F., Idiart T. P., 1999, ApJ, 521, 753

Tinsley B. M., 1979, ApJ, 229, 1046

Tolstoy E., Hill V., Tosi M., 2009, ARA&A, 47, 371

Tominaga N., Umeda H., Nomoto K., 2006, in Kubono S., Aoki W., Kajino T., Motobayashi T., Nomoto K., eds, American Institute of Physics Conference Series Vol. 847, Origin of Matter and Evolution of Galaxies. pp 488–490, doi:10.1063/1.2234468

Tominaga N., Umeda H., Nomoto K., 2007, ApJ, 660, 516

Turk M. J., Abel T., O'Shea B., 2009, Science, 325, 601

Umeda H., Nomoto K., 2002, ApJ, 565, 385

Umeda H., Nomoto K., 2003, Nature, 422, 871

Umeda H., Nomoto K., 2005, ApJ, 619, 427

Vartanyan D., Burrows A., Radice D., Skinner M. A., Dolence J., 2018, MNRAS, p. 2479

Viegas S. M., 1995, MNRAS, 276, 268

Vladilo G., Centurión M., Bonifacio P., Howk J. C., 2001, ApJ, 557, 1007

Vladilo G., Abate C., Yin J., Cescutti G., Matteucci F., 2011, A&A, 530, A33

Vogt S. S., et al., 1994, in Crawford D. L., Craine E. R., eds, Society of Photo-Optical Instrumentation Engineers (SPIE) Conference Series Vol. 2198, Instrumentation in Astronomy VIII. p. 362, doi:10.1117/12.176725

Weaver T. A., Woosley S. E., 1993, Physics Reports, 227, 65

Webster D., Bland-Hawthorn J., Sutherland R., 2015a, ApJl, 799, L21

Webster D., Bland-Hawthorn J., Sutherland R. S., 2015b, ApJ, 804, 110

Weisz D. R., et al., 2012, ApJ, 748, 88

Weisz D. R., Dolphin A. E., Skillman E. D., Holtzman J., Gilbert K. M., Dalcanton J. J., Williams B. F., 2014, ApJ, 789, 148

Welsh L., Cooke R., Fumagalli M., 2019, MNRAS, 487, 3363

Welsh L., Cooke R., Fumagalli M., Pettini M., 2020, MNRAS, 494, 1411

Welsh L., Cooke R., Fumagalli M., 2021, MNRAS, 500, 5214

West C., Heger A., Austin S. M., 2013, ApJ, 769, 2

Wheeler J. C., Sneden C., Truran Jr. J. W., 1989, ARA&A, 27, 279

Wheeler C., Oñorbe J., Bullock J. S., Boylan-Kolchin M., Elbert O. D., Garrison-Kimmel S., Hopkins P. F., Kereš D., 2015, MNRAS, 453, 1305

Wheeler C., et al., 2018, arXiv e-prints,

Wolfe A. M., Turnshek D. A., Smith H. E., Cohen R. D., 1986, ApJs, 61, 249

Wolfe A. M., Gawiser E., Prochaska J. X., 2005, ARA&A, 43, 861

Wolfire M. G., McKee C. F., Hollenbach D., Tielens A. G. G. M., 2003, ApJ, 587, 278

Woosley S. E., 2017, ApJ, 836, 244

Woosley S. E., Weaver T. A., 1995, ApJs, 101, 181

Woosley S. E., Heger A., Weaver T. A., 2002, Reviews of Modern Physics, 74, 1015

Wright A. C., Brooks A. M., Weisz D. R., Christensen C. R., 2019, MNRAS, 482, 1176

Xu H., Wise J. H., Norman M. L., 2013, ApJ, 773, 83

Yamada S., Suda T., Komiya Y., Aoki W., Fujimoto M. Y., 2013, MNRAS, 436, 1362

Yong D., et al., 2013, ApJ, 762, 26

Yoon S.-C., Dierks A., Langer N., 2012, A&A, 542, A113

Yoshida N., Abel T., Hernquist L., Sugiyama N., 2003, ApJ, 592, 645

Yoshida N., Omukai K., Hernquist L., Abel T., 2006, ApJ, 652, 6

Yoshida N., Oh S. P., Kitayama T., Hernquist L., 2007, ApJ, 663, 687

Yuan S., Cen R., 2016, MNRAS, 457, 487

Zafar T., Centurión M., Péroux C., Molaro P., D'Odorico V., Vladilo G., Popping A., 2014, MNRAS, 444, 744

de Jong R. S., et al., 2012, in McLean I. S., Ramsay S. K., Takami H., eds, Society of Photo-Optical Instrumentation Engineers (SPIE) Conference Series Vol. 8446, Ground-based and Airborne Instrumentation for Astronomy IV. p. 84460T (arXiv:1206.6885), doi:10.1117/12.926239